MEASURING THE PHOTON ENERGY SCALE THROUGH TEST BEAM DATA

by

Karina Flavia Loureiro

A preliminary report submitted in partial fulfillment of
the requirements for the degree of

Doctor of Philosophy

(Physics)

at the

UNIVERSITY OF WISCONSIN–MADISON

2006

To my family and Stephen, my loving husband.

ACKNOWLEDGMENTS

I would like to express my thanks to the many people without whom this work would have not been accomplished. I am forever thankful to my family for their love and support throughout the years. My grandparents, Patitita and Patitito, who are always watching over me. Patitita transmitted me the strength to pursuit my dreams, while Patitito, the professor, instilled in me the curiosity for all things in nature. My mom Elena, the educator, has given me love and encouragement from miles away. Nora, my older sister, has always shared with me her strength and confidence. I thank my nieces Meli and Deni for their unconditional love and my brother-in-law, Carlitos, for being like a brother to me and for putting up with my sister and nieces. I deeply thank my loving husband, Stephen, who followed me all over the world and offered me his love and support through all times. My special thanks go also to my pets Clarita, Stinky, Mandarina and Canela for bringing joy into my life.

I am truly grateful to my friend and colleague, Stathes Paganis, from whom I learnt the tricks of the trade and whose advise has been invaluable towards the completion of this work.

I am thankful to all my dear friends who were with me until the very last moment especially Valeria Pérez-Reale, Connie Potter, Annabelle Leung Fook Cheong and Sophia Chouridou.

I would like to thank many members of the ATLAS collaboration for their assistance in recent years. In particular I would like to thank Isabelle Wingerter-Seez for her guidance and kindness and for allowing me to be a part of the cheerful liquid argon community; Tancredi Carli, for his relentless pursuit of truth; Monika Wielers and Guillaume Unal, for giving me a big helping hand in my early studies of photon/jet rejection; Alden Stradling [1], for being a

---

[1] To whom I owe a chocolate cake.

wonderful proof-reader and for saving me every time ’Agatha’, my computer, decided to bail out on me.

Finally, I would like to thank my advisor, Prof. Sau Lan Wu, for giving me her immeasurable support and for offering me the opportunity to be part of her group along with the immense advantage of being based at the heart of the experiment.

DISCARD THIS PAGE

TABLE OF CONTENTS

Page

Appendix

Page

DISCARD THIS PAGE

LIST OF TABLES

Table Page

Appendix
Table

DISCARD THIS PAGE

LIST OF FIGURES

Figure Page

Appendix
Figure Page

Figure Page

Appendix

Figure Page

Figure

DISCARD THIS PAGE

NOMENCLATURE

Axes	The beam direction defines the z-axis, and the x-y plane is the plane transverse to the beam direction. The positive x-axis is defined as pointing from the interaction point to the center of the LHC ring, and the positive y-axis is pointing upwards.
ϕ	The azimuthal angle, where $tan(\phi) \equiv \frac{p_y}{p_x}$. It is measured around the beam axis.
θ	The angle measured from the beam axis.
η	The pseudorapidity is defined as $\eta = -ln(\frac{\theta}{2})$.
σ	This variable usually refers to the standard deviation of some implicit Gaussian distribution, thus it is used in several ways. In the context of detector performance, σ refers to the resolution of a reconstructed quantity. It is also the symbol that is used for the cross-section of a given particle interaction.
ADC	Analog to Digital Converter.
LAr	Liquid Argon.
EM	Electro-magnetic.
OFC	Optimal Filtering Coefficient.
EMC	Electro-magnetic Calorimeter.
EMEC	Electro-magnetic End-Cap.

MEASURING THE PHOTON ENERGY SCALE THROUGH TEST BEAM DATA

Karina Flavia Loureiro

Under the supervision of Professor Sau Lan Wu
At the University of Wisconsin-Madison

This dissertation aims at measuring the photon energy scale combining specialized Monte Carlo simulation with data taken during the combined ATLAS test beam in 2004.

This work explains the steps taken to arrive at the photon energy scale, starting from the knowledge acquired for electrons. The chapters are structured as follows: Chapters 1 and 2 briefly introduce this work and the motivation behind it. Chapter 3 gives an overview of the LHC experiment and the ATLAS detector as a whole. Chapters 4 and 5 address in detail the ATLAS electromagnetic calorimeter and signal reconstruction at the cell level. Chapter 6 concentrates on the setup for the combined test beam with emphasis on the photon run. Chapter 7 details the event selection strategy used for the photon run analysis. Chapter 8 describes the generation and tuning of the special Monte Carlo for the photon run. Chapter 9 focuses on the highly specialized Monte Carlo studies that employed special calibration objects known as calibration hits. Chapter 10 details the methodology behind the measurement of the photon scale and evaluates it in terms of the electromagnetic calorimeter resolution. Chapters 11 and 12 present a summary of the results and the conclusions, respectively.

Sau Lan Wu

ABSTRACT

This dissertation aims at measuring the photon energy scale combining specialized Monte Carlo simulation with data taken during the combined ATLAS test beam in 2004.

This work explains the steps taken to arrive at the photon energy scale, starting from the knowledge acquired for electrons. The chapters are structured as follows: Chapters 1 and 2 briefly introduce this work and the motivation behind it. Chapter 3 gives an overview of the LHC experiment and the ATLAS detector as a whole. Chapters 4 and 5 address in detail the ATLAS electromagnetic calorimeter and signal reconstruction at the cell level. Chapter 6 concentrates on the setup for the combined test beam with emphasis on the photon run. Chapter 7 details the event selection strategy used for the photon run analysis. Chapter 8 describes the generation and tuning of the special Monte Carlo for the photon run. Chapter 9 focuses on the highly specialized Monte Carlo studies that employed special calibration objects known as calibration hits. Chapter 10 details the methodology behind the measurement of the photon scale and evaluates it in terms of the electromagnetic calorimeter resolution. Chapters 11 and 12 present a summary of the results and the conclusions, respectively.

Chapter 1

Introduction

In choosing the ATLAS experiment at the LHC, I made a compromise between the exploring of the possibilities of one of the greatest experiments ever built and the fact that I would not be able, during my graduate student career, to analyze data from the experiment until late 2007. This shifted my focus to the only available source of data that would give me hands-on experience similar to the experiment at its outset. The source came from the first ATLAS combined test beam. During 2004, all sub-detectors were assembled to mimic a slice of the real detector. It was during this time that I got a taste of the life of an experimentalist and the real problems that the experiment, as a whole, might face should pragmatism and realisticx expectations not prevail during the early stages. I was very fortunate to work with scientists that understood, recognized these issues and pointed me in the right direction.

The work presented here is divided into four basic units. The first one addresses the LHC experiment as a whole, the ATLAS detector and the electromagnetic calorimeter (in detail). The second section is dedicated to the combined test beam analysis, from setup to event selection, while the third one is focused on Monte Carlo tuning and detailed calibration hits studies. The final section focuses on the measurement of the photon energy scale via test beam data combined with the results from the calibration hits studies. This dissertation is, therefore, an attempt to obtain the photon energy scale through the exclusive use of calorimeter information.

It is the author's hope that this work be continued and extrapolated to the full ATLAS detector in the near future, for channels with final state photons will benefit highly from the right calibration.

Chapter 2

Motivation

Discovery physics, as well as high-statistics precision measurements, will require the extraction of clean signals with the ATLAS detector. This will, in turn, demand precise in-situ calibration of the different sub-detectors, which comprise 448 regions inside $|\eta| < 2.5$ [1]. In-situ calibration will be done with physics samples. For the Liquid Argon calorimeter, Z→ $e^{+}e^{-}$ events will be used [3] [16].

The requirements imposed by an early discovery of a low mass (M_H=130 GeV) Higgs boson, decaying either leptonically or into two photons, during the low luminosity period [13] [23] make the ATLAS calorimeter the first choice to begin this calibration (see Figure 2.1).

Electron-based calibration has been investigated for quite some time. The well-understood results were promising enough that a whole calibration scheme was developed and implemented in the ATLAS software framework. It is important to note that the results (i.e. calibration constants) came from Monte Carlo (MC) simulation studies of the ATLAS detector (almost final geometry), and are being verified with test beam data.

Figures 2.2(a) and 2.2(b) show the improvement on the resolution and uniformity for electrons in the liquid-argon calorimeter as a function of pseudorapidity when using the electron calibration [25]. At the same time, tests performed using the electron calibration when reconstructing the invariant masses for the Z→ $e^{+}e^{-}$ and to the H→ $4e$ processes rendered this electron calibration the preferred choice as seen in Figure 2.2(c).

---

[1] The standard region corresponds to 2 mother boards in azimuth, equivalent to 2 HV sectors in the barrel. In each end-cap, there are 4 mother boards and 7 HV sectors along pseudorapidity. This definition chooses the HV sectors, leading thus to a higher number of regions [16].

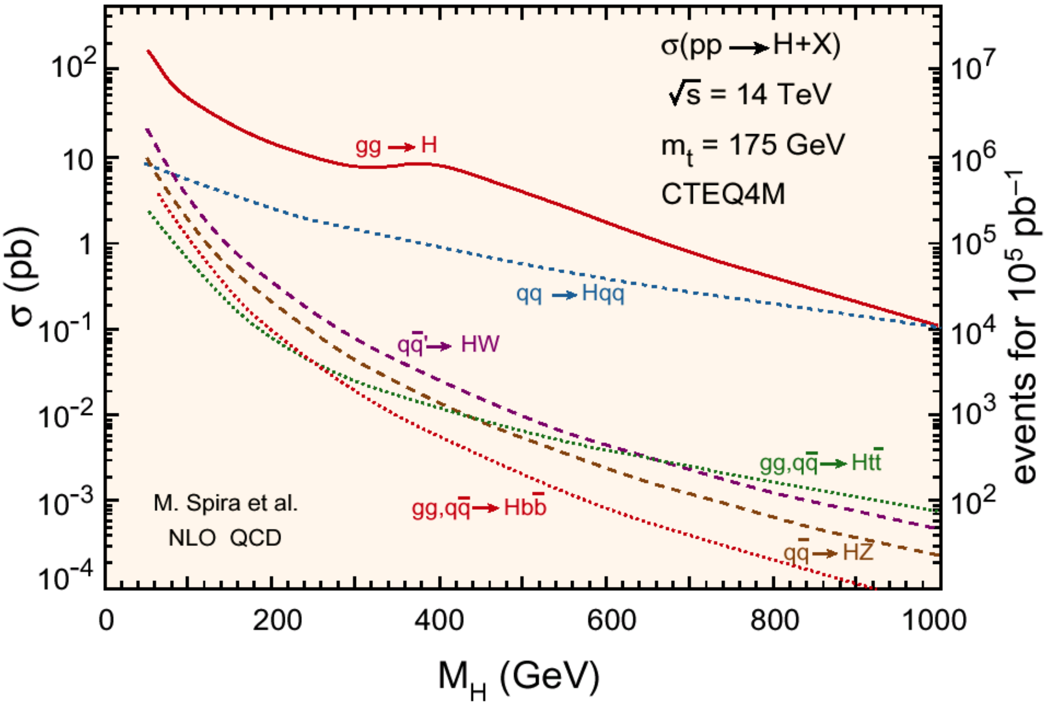

Figure 2.1 Cross-section for $pp \to H + X$ as a function of M_H from M. Spira Fortsch. *Phys. 46* (1998).

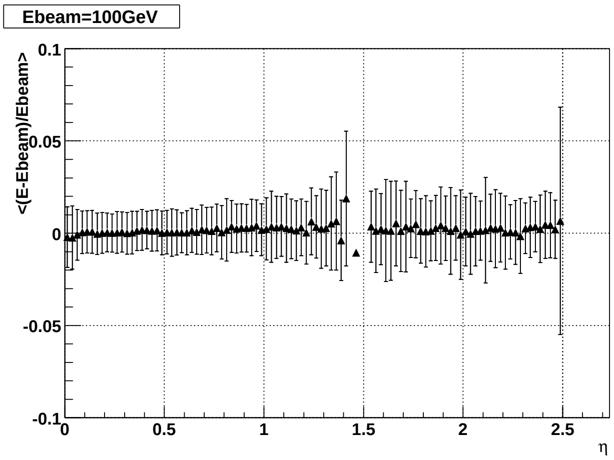

(a) Electron Resolution as a function of η for 100 GeV electrons. Simulation done with full ATLAS.

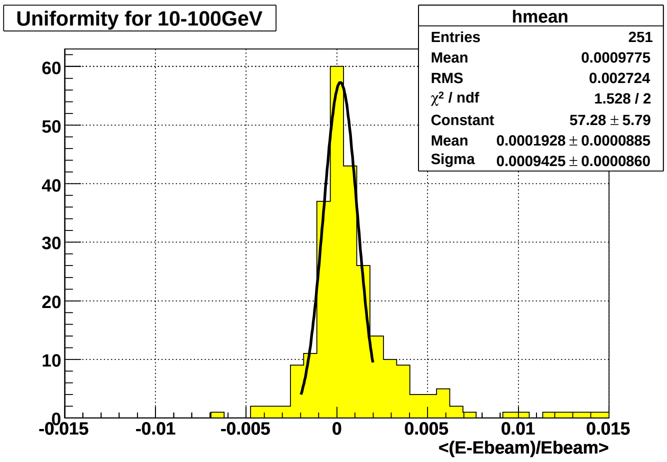

(b) Uniformity for electrons with energies in the range of 10 to 100 GeV.

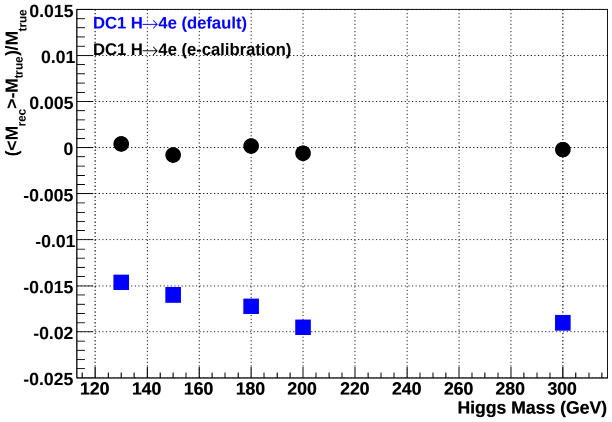

(c) Linearity of the reconstructed $H \rightarrow 4e$ invariant mass with (black) and without (blue) electron-calibration constants.

Figure 2.2 Effects on the linearity, uniformity and mass reconstruction of electrons after the application of the calibration constants [25].

With the onset of the 2004 ATLAS combined test beam effort, where a complete sector of the detector was exposed to different beams of particles, came the idea of extending this electron-based calibration to photons. Previous tests conducted on ATLAS MC simulations using photon samples with the same characteristics as those of the electrons gave a good assessment of the feasibility of the proposed idea. This concept gained momentum along with the potential for the early discovery of the Higgs through the $\gamma\gamma$ channel. Though the extension of the electron calibration to photons seemed straight forward, one serious complication arose. Photons of this high momentum (60 GeV/c) lose energy mostly by pair production, meaning that the final state of any decay channel where photons are involved will have non-interacting photons, known as *non-converted* photons and interacting or *converted* photons.

In the H$\rightarrow \gamma\gamma$ channel, contribution from both interacting and non-interacting photons will have an impact on the mass peak. If not treated properly, the peak will not be seen in the sea of the irreducible $\gamma\gamma$ background continuum. Figures 2.3(a) and 2.3(b) show the differences in the invariant mass reconstruction for this channel, taking into consideration the two types of photons and the two luminosity scenarios.

It is expected that the converted photons will behave like electrons, while the non-converted ones will have their own calibration scheme. Unfortunately, the problem is not defined solely by the categorization of the photons, but it is specified by the design requirements of the ATLAS detector (i.e. between the inner detector and the face of the calorimeter, there are approximately $1.3X_0$ of extra material in which conversions can occur). The implications of these very late conversions are treated in Appendix C.

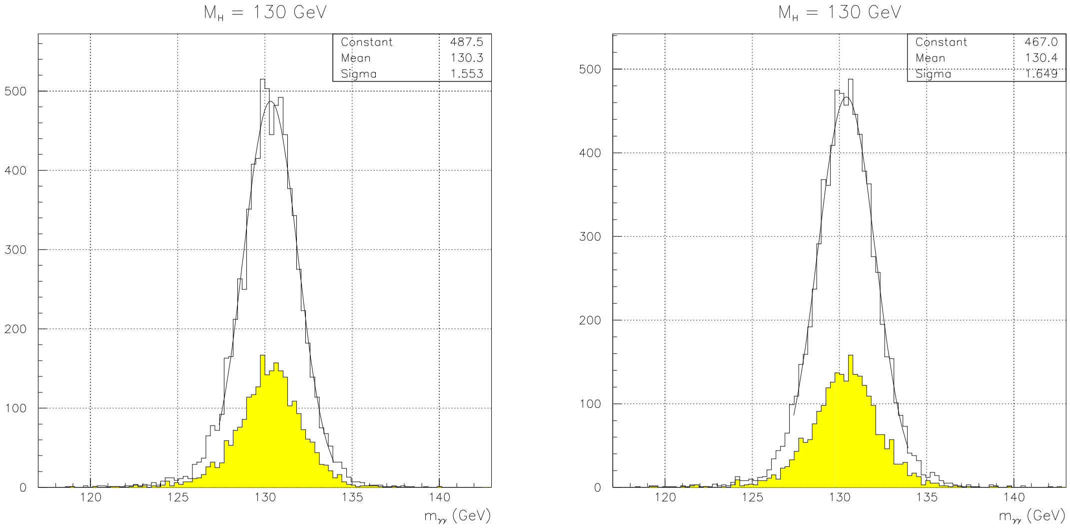

(a) Low Luminosity Scenario

(b) High Luminosity Scenario

Figure 2.3 Reconstructed two photon invariant mass for the $H \rightarrow \gamma\gamma$ decay channel using the calorimeter information only. The yellow histograms represent events containing at least one converted photon. [4]

This dissertation, though not delving into the physics of the Higgs boson mechanism, tries to test the electron calibration method on photons, relying exclusively on the liquid argon calorimeter. This exercise will acquire importance as we approach the high luminosity régime, for the inner detector tracking systems will be saturated by the number of tracks [23] and the calorimeter will be the sub-detector of choice for this channel.

Chapter 3

The LHC and ATLAS

This chapter serves as an introduction to the main features of the Large Hadron Collider (LHC). It also delves into some details pertaining to the ATLAS (A Toroidal LHC ApparatuS) experiment. The first section presents the relevant accelerator parameters and the physics program allowed by the machine. The second section describes the structure of the ATLAS detector and sub-detectors considering the requirements imposed by the physics program and the machine features.

3.1 Introduction to the LHC

3.1.1 Machine Parameters

The Large Hadron Collider [42] is a proton-proton and heavy-ion (Pb-Pb) collider with a center of mass energy of 14 TeV when operating in the pp mode. The accelerator, which is presently under construction in the existing LEP tunnel, will begin operations in 2007. The basic layout of the machine mirrors that of LEP with 8 straight sections, each approximately of 528 m, available for experimental insertions or utilities. The two high-luminosity insertions are located in diametrically opposite straight sections, Point 1 (ATLAS) and Point 5 (CMS) (see Figure 3.1). Two more experimental insertions are located at Point 2 (ALICE Pb ions) and Point 8 (B physics). The beams cross from one ring to the other only at these four locations. The 27 km circumference of the tunnel houses 1232 super-conducting dipoles that produce the magnetic field (8.33 Tesla) necessary to keep the beam in its trajectory. Bunches of protons, separated by 25 ns and with an RMS length of 75 mm, intersect at the 4 points mentioned above.

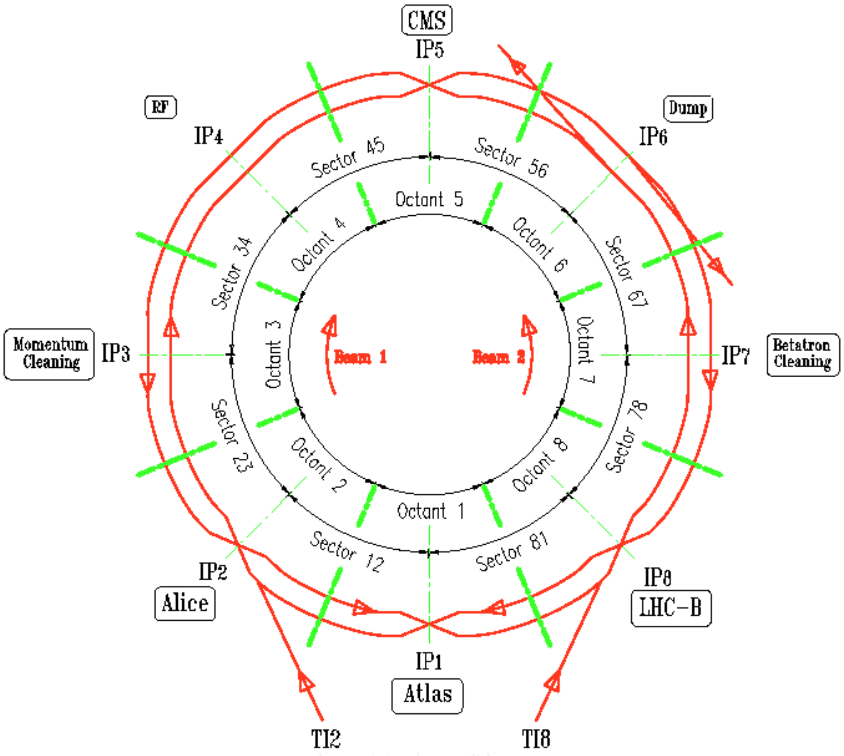

Figure 3.1 Schematic layout of the LHC

The preacceleration chain, shown in Figure 3.3, consists of the following steps: an ion source injects the protons into a radio-frequency (RF) cavity which accelerates them to $750keV$. After this, they are transmitted to a proton LINAC (linear accelerator) to reach energies of $50MeV$. The proton synchrotron BOOSTER (PSB) increases the energy up to $1.4GeV$ and sends the protons to the proton synchrotron (PS) and later to the super-proton synchrotron (SPS) which then boost the proton energy to $25GeV$ and $450GeV$, respectively. The protons at $450GeV$ are injected into each LHC ring with 2835 bunches of 10^{11} particles. The bunch spacing will be 7.48 m, corresponding to an interval between two successive bunches of 25 ns at the collision energy. The super-conducting dipole magnets, see Figure 3.2, guide the proton beams in their LHC orbits over a total magnetic length of 15 km. Super-conducting quadrupole correctors will make the orbit corrections to the spurious non-linear components of the guiding and focusing magnetic fields of the machine and allow recovery of the required beam density after interactions. Special orbit correctors will be used - sextupole, octupole and decapole magnets. The luminosity lifetime is anticipated to be about 10 hours. The luminosity L is defined as:

$$L = \frac{N_1 \cdot N_2}{(4\Pi \cdot \sigma_x \sigma_y)} \cdot n_b \cdot f_{rev} \tag{3.1}$$

L is the interaction rate of particles per unit cross-section. N_1 and N_2 are the number of particles per bunch for each beam, σ_x and σ_y are the beam sizes in the transverse directions cross-section, n_b is the number of bunches and f_{rev} is the revolution frequency. The two beam pipes of the LHC and the super-conducting coils will be housed in the same super-fluid helium cryostat at the temperature of 1.9 K.

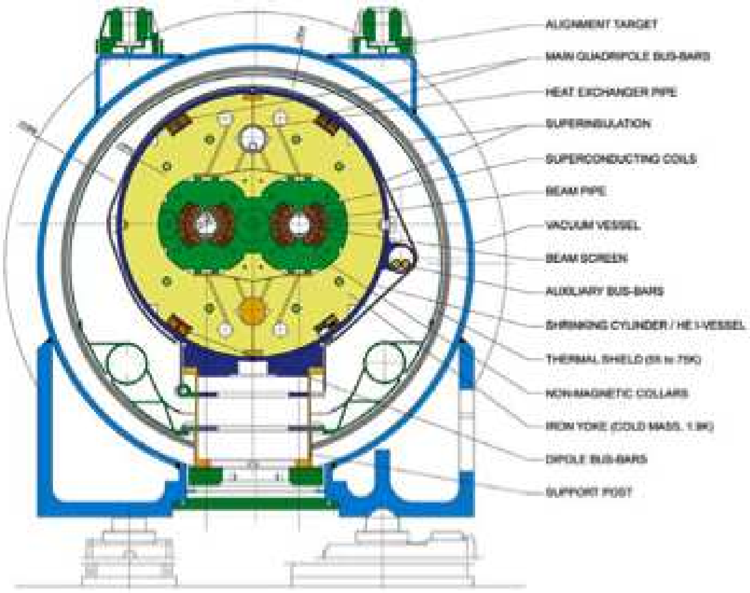

Figure 3.2 LHC dipole cross-section. The nominal magnetic field is 8.33 T inside a cold beam tube of 50 mm inner diameter, with a magnetic length of 14.3 mm.

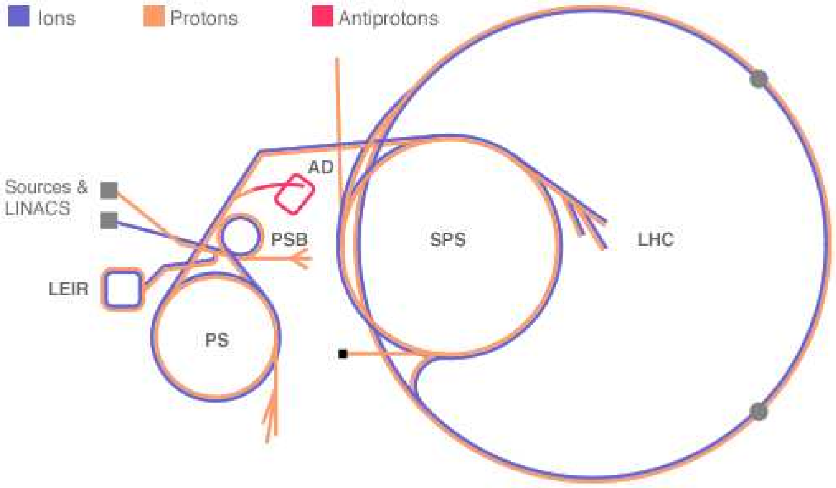

Figure 3.3 LHC proton injection chain

Two operational phases are foreseen for the LHC. During the first year (*low luminosity phase*) the nominal luminosity is expected to be $2 \times 10^{33} cm^{-2} s^{-1}$. It should then increase to $10^{34} cm^{-2} s^{-1}$ (*high luminosity phase*). The LHC is expected to deliver $100 fb^{-1}$ of integrated luminosity per year at design luminosity. The machine will also be able to accelerate heavy ions to a center of mass energy of 1150 TeV with a luminosity up to $10^{27} cm^{-2} s^{-1}$. LHC parameters are listed in Table 3.1.

3.1.2 The Physics Goals of the LHC

The LHC will allow a broad and ambitious physics program. Among the most important topics to be covered are:

- **Search for a Standard Model (SM) Higgs boson from the LEPII low mass limit (114.1 GeV) up to the theoretical upper bound of 1 TeV [2].** One of the main goals is to study the actual mechanism for symmetry breaking in the electroweak sector (SU(2) x U(1)) of the Standard Model (SM). This phenomenon is associated with the Higgs mechanism, the existence of a Higgs particle and the behavior of the cross-sections involving

Table 3.1 LHC performance parameters

LHC Parameter	Symbol	Unit	Nominal Value
Energy	E	[TeV]	7.0
Dipole field	B	[T]	8.4
Luminosity	L	$[cm^{-2}s^{-1}]$	10^{34}
Beam-beam parameter	ξ		0.0034
Total beam-beam tune spread			0.01
Injection energy	E_i	[GeV]	450
Circulating current/beam	I_{beam}	[A]	0.53
Number of bunches	k_b		2835
Harmonic number	$[h_{RF}$		35640
Bunch spacing	τ_b	[ns]	24.95
Particles per bunch	n_b		1.0510^{11}
Stored beam energy	E_S	[MJ]	334
Normalized transverse emittance $(\beta\gamma)\sigma^2/\beta$	ϵ_n	$[\mu m.rad]$	3.75
Collisions			
β-value at I.P.	$\beta*$	[m]	0.5
r.m.s. beam radius at I.P.	$\sigma*$	$[\mu m]$	16
r.m.s. divergence at I.P.	σ^J*	$[\mu rad]$	32
Luminosity per bunch collision	L_b	$[cm^{-2}]$	3.1410^{26}
Crossing angle	ϕ	$[\mu rad]$	200
Number of events per crossing	n_c		19
Beam lifetime	τ_{beam}	[h]	22
Luminosity lifetime	τ_L	[h]	10

the gauge bosons, W^{+-} and Z. The LHC will explore all ranges of allowed Higgs masses and will either find the Higgs or invalidate the SM symmetry-breaking mechanism.

- **Search for Supersymmetry, extra dimensions and other exotic signals beyond the Standard Model up to masses of 5 TeV.** If SUSY particles exist, they will be produced and detected at the LHC. The lightest SUSY particle is stable but hardly interacts with matter. Therefore the search for supersymmetric particles will base itself on the hermeticity of the detector and its ability to identify missing E_T. ATLAS may be also used to detect microscopic black-holes with masses up to 5 TeV.

- **Precision measurements of SM observables such as W and top quark masses and couplings.** The LHC will provide a large number of top quarks. The $t\bar{t}$ cross-section will be about 1nb. Such high statistics will allow the experiment to obtain a top-mass resolution limited by theoretical rather than statistical uncertainties.

- **B physics and CP violation in the B hadron system.** The principal issue of B physics is the observation of CP violation in the B_d^0 system, and the goal is to measure the three interior angles of the unitarity triangle corresponding to the Cabibbo-Kobayashi-Maskawa (CKM) matrix. During the initial low-luminosity run, b-quark identification will not be hindered by pile-up in the detectors.

- **Study of phase transitions from hadronic matter to plasma of deconfined quarks and gluons.**

3.1.3 Environmental Characteristics

The LHC experiments will have to deal with complex working conditions imposed by the high center-of-mass energy and luminosity. For the two general purpose experiments, the total inelastic pp cross section at $\sqrt{s} = 14TeV$ is approximately 80 mb. At high luminosity, the expected event rate is $\approx 10^9 ev/s$. Two types of events will be characteristic of this environment:

- *Minimum bias events* due to long-distance collisions between two incoming protons, in which the momentum transfer is small (“soft “ collisions). Though the study of these events is not foreseen, they represent the majority of the pp collisions and their effective total cross section is of the order of $\sigma_{m.b}^{tot} \sim 70mb$. The final state products of these interactions (also called minimum bias events) have small transverse momentum relative to the beam line. In reality, most of them escape down the beam pipe. The particles with high enough p_T enter the active region of the detectors, giving rise to the so called *pile-up* events.

- *Hard scattering events* arise from short-range parton interactions in the incoming protons. In these interactions the momentum transfer can be large, allowing the production of final states with high p_T particles, as well as the creation of new massive ones. High p_T events are dominated by QCD jet production from quark and gluon fragmentation in the final state.

3.1.4 LHC Experimental Challenges

The first year of operation will be the crucial one, given that the LHC is the first super-conducting collider foreseen to operate with such a large beam current. Super-conducting magnets tolerate only extremely small beam losses, and up to now the precise tolerance level of the LHC magnets is not well known. In order to prevent excessive quenching of the magnets, the particles in the beam halo which slowly diffuse out towards the beam-pipe walls have to be intercepted very efficiently by collimators in a warm section of the machine. However, learning how to operate the LHC in such conditions will take some time and the initial commissioning of the machine will be done with beams of much smaller intensity than the nominal one. In order to avoid a dramatic reduction of luminosity (proportional to the square of the beam current), the transverse emittance will have to be reduced. After about one year of commissioning it is reasonable to expect that the LHC could be operated with one tenth to one fifth of the nominal beam current. Assuming that an emittance as low as 1 μm could be achieved, a luminosity

Table 3.2 LHC parameters: commissioning and nominal values

Parameter	Symbol	Unit	Commissioning	Nominal
Luminosity	L	$[cm^{-2}s^{-1}]$	10^{33}	10^{34}
Circulating current/beam	I_{beam}	[A]	0.087	0.53
Particles per bunch	n_b		0.1710^{11}	1.0510^{11}
Number of bunches	k_b		2835	2835
Normalized transverse emittance	ϵ_n	[μm.rad]	1	3.75
Beam-beam parameter	ξ		0.0021	0.0034

of $10^{33}cm^{-2}s^{-1}$ would be provided with the beam current at 16% of the nominal value (see Table 3.2).

3.1.5 Detectors Requirements

Due to the stringent requirements imposed by the LHC design, the detectors will have the following constraints:

- *Response time and granularity*. A fast detector response is required to minimize the signal contamination from minimum bias events overlapping interesting physics signals. The response time varies between sub-detectors and represents the best compromise between technological limits and detector features. High granularity is required in order to reduce the impact of pile-up. This implies a large number of read-out channels.

- *Radiation tolerance*. The high flux of particles coming from the pp collisions represents an unavoidable source of radiation for the LHC detectors. The radiation level will be different according to the sub-detector position with respect to the interaction point. For example, in the forward calorimeters, the particles flux integrated over 10 years of operations, will amount up to 10^{17} neutrons per cm^2 and up to 10^7 Gy of absorbed energy. The ATLAS electromagnetic calorimeter will receive less than 10^{13} neutrons per cm^2

and ≈ 200 Gy in 10 years running at high luminosity and in the worst location of the electronics [6].

- *Hermeticity*. At hadron colliders, the energy of interacting partons (quarks and gluons) is not known in individual events, therefore the missing energy of the final state cannot be determined. To compensate, the measurement of the transverse energy (e.g. important for SUSY searches) and the efficient reconstruction of tagging jets require a rapidity coverage up to $|\eta|$ = 5.
- *Mass and momentum resolution*. An energy resolution $\sigma/E \sim 10\%/\sqrt{E}$, with a global constant term smaller than 1%. is needed to achieve a mass resolution of 1% or better for the channels $H \rightarrow \gamma\gamma$ and $H \rightarrow 4$ l.
- *Particle identification capabilities*. Several strict requirements are imposed on the identification of electrons, photons, b-jets, taus, etc. For example, in order to observe the $H \rightarrow \gamma\gamma$ decay over a continuum irreducible $\gamma\gamma$ background, a γ/jet rejection factor of the order of 10^3, along with a photon efficiency of $\sim 80\%$, are required.
- *Trigger*. The trigger is another critical factor for the ATLAS and other experiments. The interaction rate of 10^9 events/second must be reduced to ~100 recorded events/second due to the limitations of the storage and analysis system. The ATLAS trigger is required to have a 10^7 rejection factor.

3.2 The ATLAS Detector

ATLAS [13] (A Toroidal LHC ApparatuS, Figure 3.4) is one of the two LHC general-purpose detectors. It is designed to be a multi-purpose detector, encompassing a large discovery potential for new physics such as the Higgs boson and supersymmetric (SUSY) particles [14].

The differences in overall detector layout between ATLAS and CMS are based on distinct approaches brought forth by the collaborations. The ATLAS detector magnet configuration is based on a thin inner super-conducting solenoid surrounding the inner detector cavity, and large

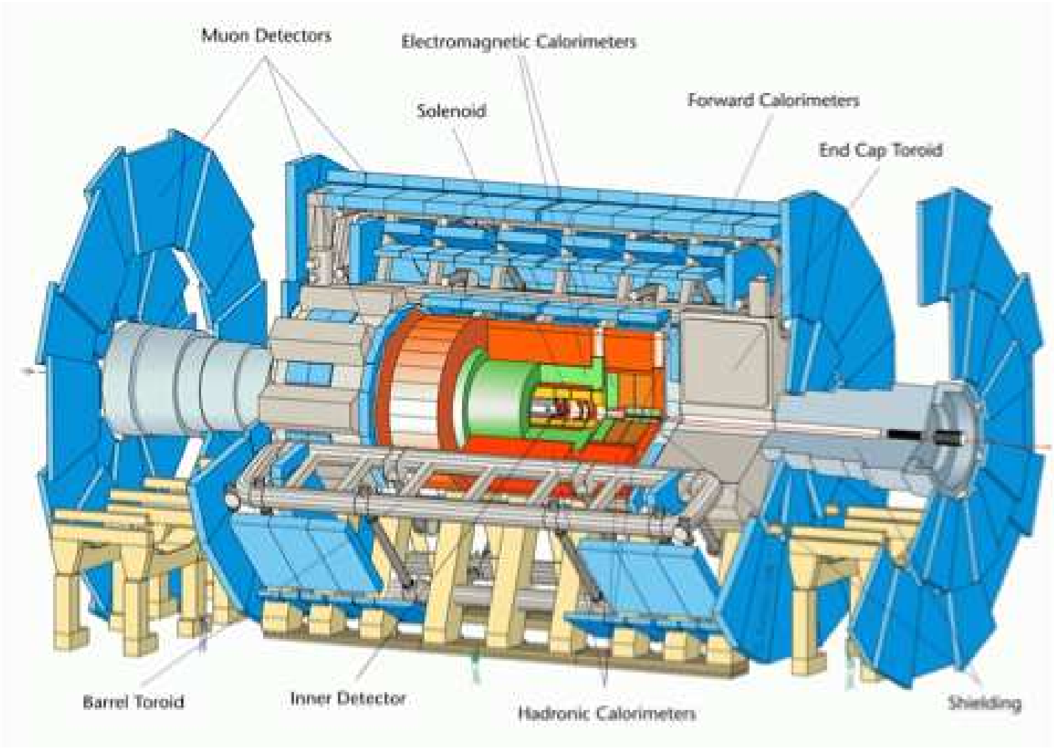

Figure 3.4 3-dimensional cutaway of the full ATLAS detector.

super-conducting air-core toroids consisting of independent coils arranged with an eighth-fold symmetry outside the calorimeters.

The Inner Detector (ID) is contained within a 7m long cylinder with a radius of 1.15m, under a solenoidal magnetic field of 2T. A combination of discrete high-resolution semiconductor pixel and strip detectors, along with a continuous straw-tube tracking detector, achieve pattern recognition, momentum and vertex measurements as well as electron identification and pion separation.

The liquid-argon (LAr) electromagnetic calorimeter exhibits excellent performance in terms of energy and position resolution. Along with the LAr end-caps (hadronic calorimeters) and the forward calorimeters, they cover up to $|\eta| = 4.9$. The bulk of the hadronic calorimetry is provided by a scintillator-tile calorimeter, which is separated into a large barrel and two smaller extended barrel cylinders, one on each side of the barrel. The entire calorimeter system provides very good jet and E_T^{miss} performance. The LAr calorimeter is contained in a cryostat with an outer radius of 2.25 m that extends longitudinally to 6.65m along the beam axis. The outer radius of the scintillator-tile calorimeter is 4.25 m and the total weight of the calorimeter is 4000 Tons.

The muon spectrometer surrounds the calorimeters and defines the overall dimensions of the ATLAS detector. The outer chambers to the barrel are at a radius of about 11 m. The half-length of the barrel toroid coils is 12.5m and the third layer of the forward muon chambers is located at 23m from the interaction point. The air-core toroid system, with a long barrel and two inserted end-cap magnets, generates a large magnetic field volume with a strong bending power. The overall weight of the ATLAS detector is about 7000 Tons.

In summary, the design of the ATLAS sub-detectors will allow for the following:

- Very good electromagnetic calorimetry for e^- and γ identification and measurement.
- Maximal hermeticity of the full calorimeter system to allow for very accurate measurements of missing transverse momentum p_T^{miss} and jet identification.

- Efficient tracking system at high-luminosity for high p_T lepton measurements and full event reconstruction capability at low luminosity.
- High-precision muon spectrometer having the capability to perform accurate measurements at the highest luminosity in stand-alone mode.

3.2.1 The Inner Detector

The layout of the ID [8] is shown in Figure 3.2.1. The ID is placed inside the magnetic field generated by the central solenoid, and provides full tracking coverage over $|\eta| < 2.5$. It provides impact parameter measurements and vertexing for heavy flavor τ tagging. It combines high-resolution detectors (pixel and silicon micro-strips (SCT)) and the inner radii and continuous tracking elements based on straw tube at the outer radii. The highest granularity is achieved around the vertex region using semi-conductor pixel detectors. The total number of precision layers is limited by both the material and monetary budgets. The combination of techniques gives very robust pattern recognition and high precision in both ϕ and z coordinates. In the barrel region, the layers are arranged on concentric cylinders around the beam axis, while in the end-cap detectors they are mounted on disks perpendicular to the beam axis. The pixel layers are segmented in $R\phi$ and z, while the SCT detector uses small angle (40 mrad) stereo strips to measure both coordinates. The barrel transition radiation tracker (TRT) straws are parallel to the beam direction. All the end-cap tracking elements are located in planes perpendicular to the beam axis. The lifetime of the ID will be limited by radiation damage, and it may need replacement after a few years, with the inner pixel layer being the most affected.

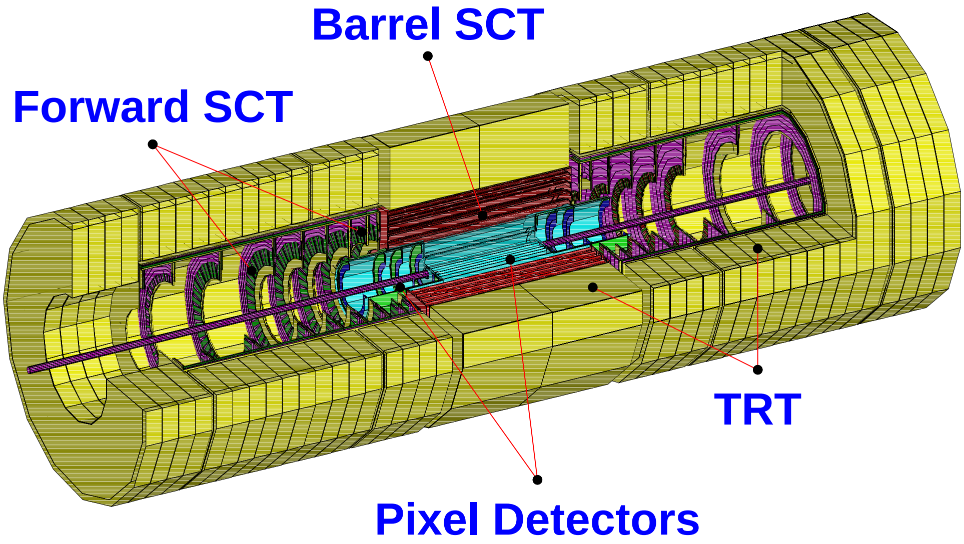

Figure 3.5 3D view of the ATLAS Inner Detector

3.2.1.1 Pixel Detector

The pixel detector is designed to provide a very high-granularity, high-precision set of measurements as close to the interaction point as possible. It provides three measurements over the full acceptance. Mechanically, it consists of three barrels at average radii of $\approx$ 4cm, 10cm and 13cm, and five disks on each side, of radii between 11 and 20 cm, which complete the angular coverage. The pixel modules are designed to be identical in the barrel and the disks. Each module is 62.4 mm long and 21.4 mm wide, with 61440 pixel elements read out by 16 chips, each serving an array of 24 by 160 pixels.

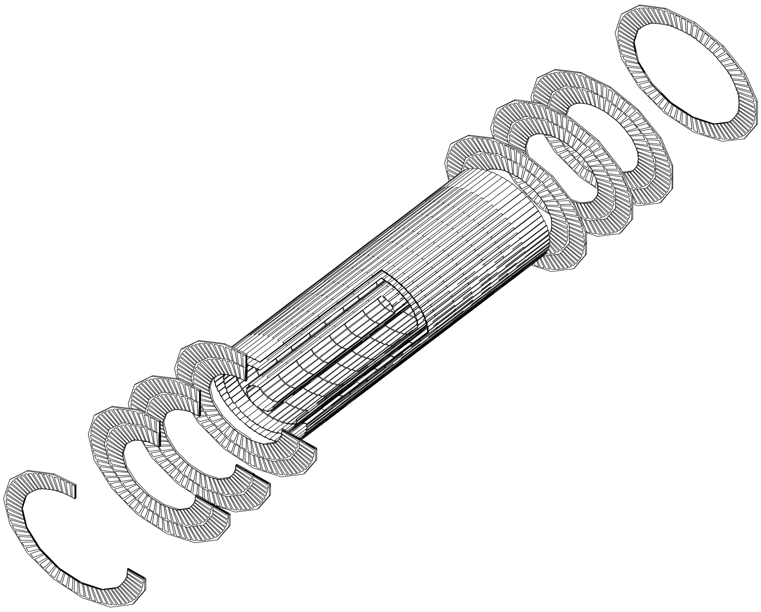

Figure 3.6 3-dimensional view of the pixel detector

3.2.1.2 Semi-Conductor Tracker (SCT)

The SCT, like the pixel detector, consists of a barrel detector and two symmetric end-cap detectors. The system is designed to provide eight precision measurements per track in the intermediate radial range, contributing to the measurement of momentum, impact parameter and vertex position. It also provides good pattern recognition. The barrel SCT uses eight layers of silicon micro-strip detectors. Each silicon detector is $6.36 \times 6.40 cm^2$ with 768 read-out strips of 80 μm pitch. The end-cap modules are similar in construction but use tapered strips, with one set aligned radially.

3.2.1.3 Transition Radiation Tracker (TRT)

The TRT is based on the use of straw detectors. Due to their small diameter they can operate at very high rates. This technique, being radiation hard, allows for typically 36 measurements per track. The barrel contains about 50,000 straws, each 4mm in diameter and divided in half at the center in order to reduce occupancy. The end-caps contain 320,000 radial straws, with the readout at the outer radius. The total number of electronic channels is 420,000. Each channel provides a drift-time measurement, giving a spatial resolution of 170 μm per straw, and two independent thresholds. These allow the detector to discriminate between tracking hits, which pass the lower threshold, and transition-radiation (TR) hits, which pass the higher one. The TRT is operated with a non-flammable gas mixture of 70$\%$ Xe, 20$\%$ CO_2 and 10$\%$ CF_4 with a total volume of 3 m^3.

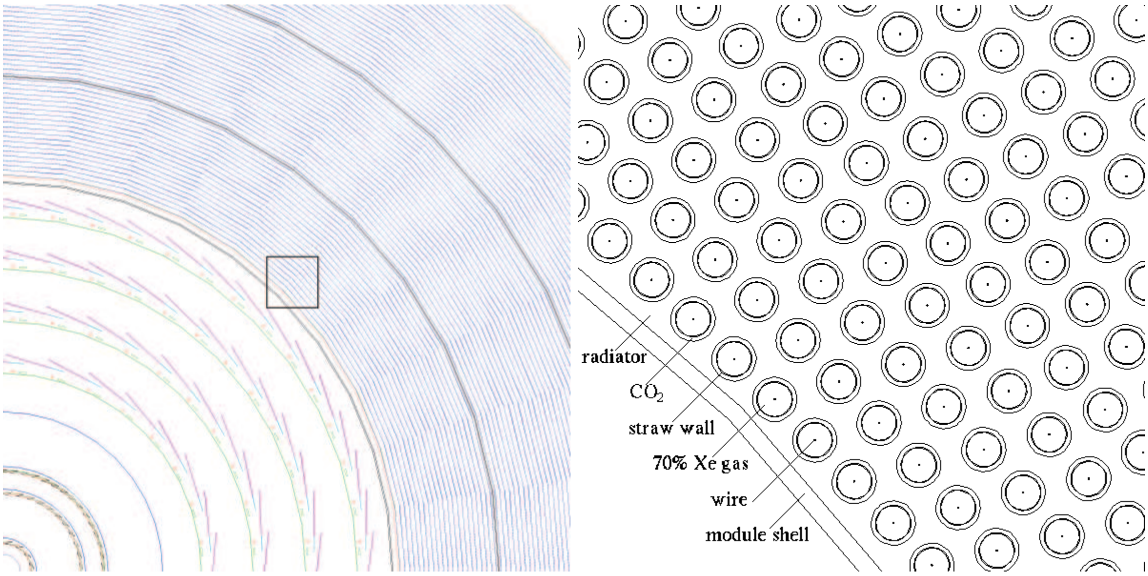

(a) Transverse view of a quarter section of the ID. (b) Detailed view of TRT straws

Figure 3.7 Schematic view of the TRT. Fig(a) represents the transverse view of a quarter section of the ID, where the TRT layers are approximated by arcs of circles. Fig(b) gives a detailed view of straws in the TRT. The view corresponds to the red box drawn in (a).

3.2.2 The Calorimeters

The calorimetric system of the ATLAS detector will provide a measure of the energy and position of photons, electrons, isolated hadrons and jets. A reliable measure of the missing transverse energy will be possible thanks to good hermeticity. Together with the inner detector, they will provide efficient and robust particle identification, exploiting the fine lateral and good longitudinal segmentation. The various parts that make up the system are described below and shown in Figure 3.8.

3.2.2.1 Electromagnetic Calorimeter

The EM calorimeter is a lead/liquid-argon sampling calorimeter with accordion geometry. It is divided into a barrel part, covering the $|\eta| < 1.475$ region and two end-caps for the $1.375 < |\eta| < 3.2$. A detailed description of the ATLAS electromagnetic calorimeter will be given in the next chapter.

3.2.2.2 Hadronic Calorimeters

The ATLAS hadronic calorimeters cover the range $|\eta| < 4.9$ using different techniques best suited for the wide spectrum of requirements and radiation environment found in their large η coverage. The hadronic calorimeters take into consideration the need for good containment of hadronic showers as well as keeping punch-through into the muon system to a minimum. Along with the large η coverage, good E_T^{miss} measurements are provided. The region $|\eta| < 1.7$ is covered by the *tile calorimeter*, a sampling calorimeter with plastic scintillator plates embedded in iron absorbers [7]. The tile calorimeter is segmented into three longitudinal samplings and the relative energy resolution is

$$\frac{\sigma}{E} = \frac{50\%}{\sqrt{E}} \oplus 3\%. \tag{3.2}$$

At larger pseudorapidities, where higher radiation tolerance is needed, the intrinsically radiation-hard liquid argon technology is used. The *hadronic end-cap calorimeter* is a copper-LAr detector with parallel plates geometry, while the *forward calorimeter* is composed of rod-shaped electrodes in a tungsten matrix using liquid argon as the active material. It is worth noting that even though the proximity of the calorimeter to the interaction point makes radiation resistance more of an issue, it provides clear benefits in terms of uniformity of the calorimetric coverage, as well as reduction of radiation background levels in the muon spectrometer. Details of the pseudorapidity coverage, granularity and longitudinal segmentation for the hadronic calorimeters can be seen in Table 3.3.

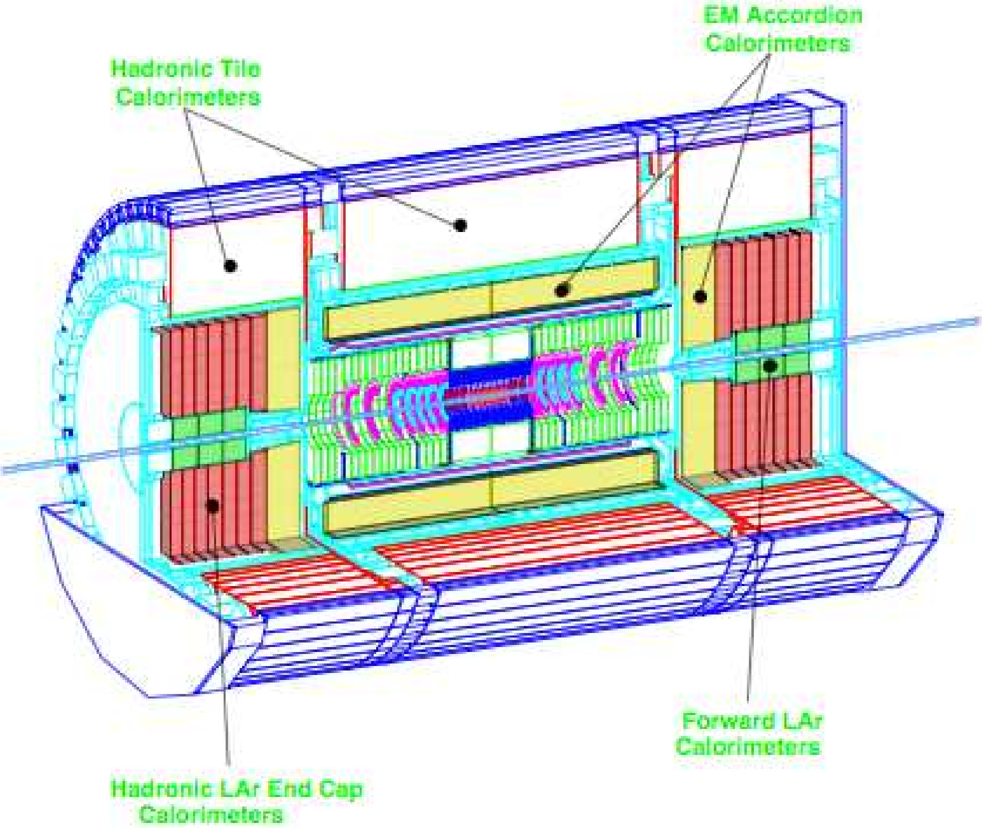

Figure 3.8 3D cutaway view of the ATLAS calorimeter, as reproduced by the Geant application.

Table 3.3 ATLAS hadronic calorimeters: pseudorapidity coverage, granularity and logitudinal segmentation

HADRONIC TILE	**Barrel**	**Extended Barrel**	
Coverage	$\|\eta\| < 1.0$	$0.8 < \|\eta\| < 1.7$	
Longitudinal segmentation	3 samplings	3 samplings	
Granularity($\Delta\eta \times \Delta\phi$)			
Samplings 1 and 2	0.1×0.1	0.1×0.1	
Sampling 3	0.2×0.1	0.2×0.1	
HADRONIC LAr		**End-cap**	
Coverage		$1.5 < \|\eta\| < 3.2$	
Longitudinal segmentation		4 samplings	
Granularity ($\Delta\eta \times \Delta\phi$)		0.1×0.1	$1.5 < \|\eta\| < 2.5$
		0.2×0.2	$2.5 < \|\eta\| < 3.2$
FORWARD CALORIMETER		**Forward**	
Coverage		$3.1 < \|\eta\| < 4.9$	
Longitudinal segmentation		3 samplings	
Granularity ($\Delta\eta \times \Delta\phi$)		$\sim 0.2 \times 0.2$	

3.2.3 The Muon Spectrometer

The layout of the muon spectrometer [11] is shown in Figure 3.10(a). Its primary function is to measure the momenta from muons that have been deflected by the magnetic fields generated by the super-conducting air-core toroid magnets. The muon tracks are reconstructed using different trigger and high-precision tracking chambers, depending on the position in η. In the barrel region, tracks are measured in chambers arranged in three cylindrical layers around the beam axis. In the transition end-cap regions (see Figure 3.10(b)), the chambers are installed vertically, also in three stations. The position of these stations of chambers has been optimized for full coverage and momentum resolution. Over most of the η range, a precision measurement of the track coordinates in the principal bending direction of the magnetic field is provided by

Monitored Drift Tubes (MDTs). At large pseudorapidities and close to the interaction point, Cathode Strip Chambers (CSCs) with higher granularity are used in the innermost plane over $2 < |\eta| < 2.7$ to withstand the demanding high rate and background conditions. The trigger system (Figure 3.9) covers the pseudorapidity range $|\eta| \leq 2.4$ and it is provided by three stations of Resistive Plate Chambers (RPCs) in the barrel and 3 stations of Thin Gap Chambers (TGCs) in the end-cap regions.

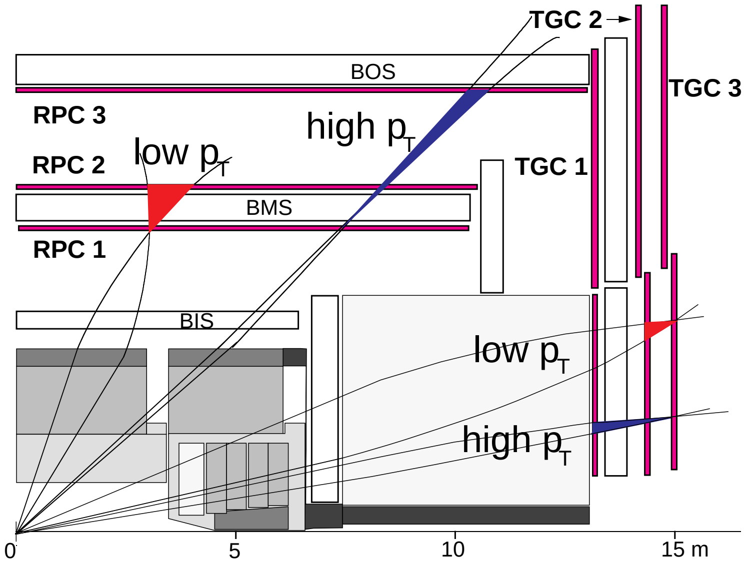

Figure 3.9 Schematic view of the triggering principle. Note that the outer layer of the end-cap MDT is not shown.

Due to the large global dimensions of the spectrometer, it is not possible to stabilize the dimensions and positions of the chambers at the 30μm level. Therefore, chamber deformations and positions are constantly monitored by means of optical alignment systems, and displacements up to ≈ 1 cm can readily be corrected in the offline analysis.

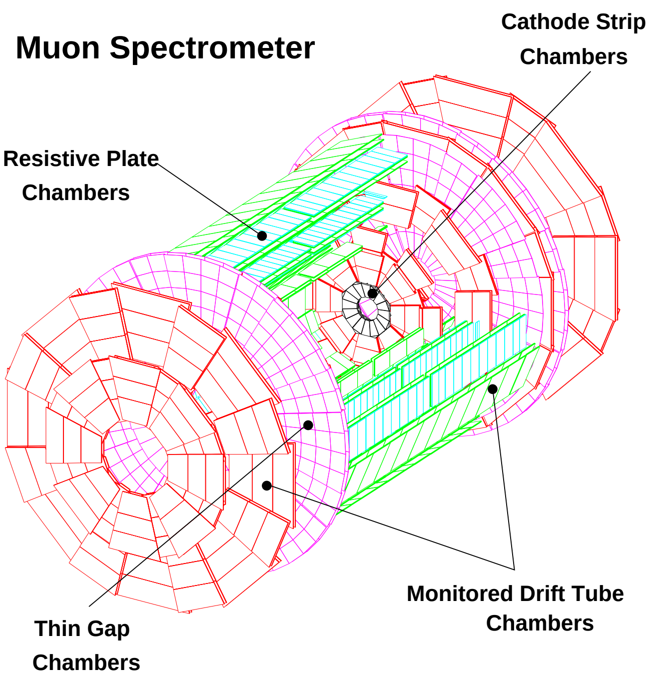

(a) Three dimensional view of the muon spectrometer with the location of the four different chamber technologies

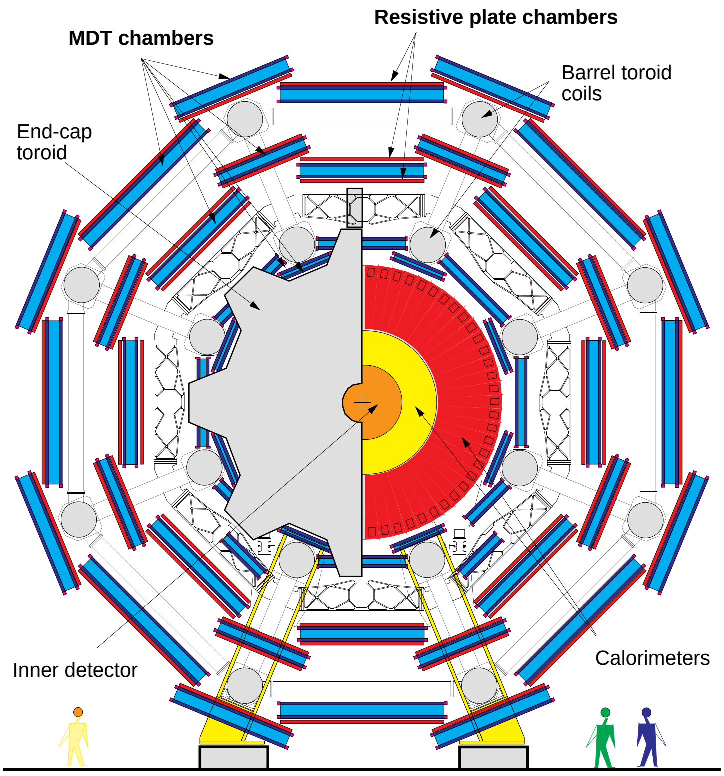

(b) Transverse view of the muon spectrometer

Figure 3.10 The ATLAS Muon Spectrometer

3.2.4 The Magnet System

A schematic view of the ATLAS super-conducting magnet system [10] can be seen in Figure 7.5(a). It comprises a central solenoid (CS) providing the Inner Detector with magnetic field, a set of eight larger air-core toroids generating the magnetic field for the muon spectrometer and 2 end-cap toroids. The CS extends over a length of 5.3 m and has a bore of 2.4 m. The overall dimensions of the magnet system are 26 m in length and 20 m in diameter. The CS provides a central field of 2 T with a peak magnetic field of 2.6 T at the super-conductor itself. The peak magnetic fields for the super-conductors in the barrel toroid (BT) and at each end-cap toroid (ECT) are 3.9 and 4.1 T respectively.

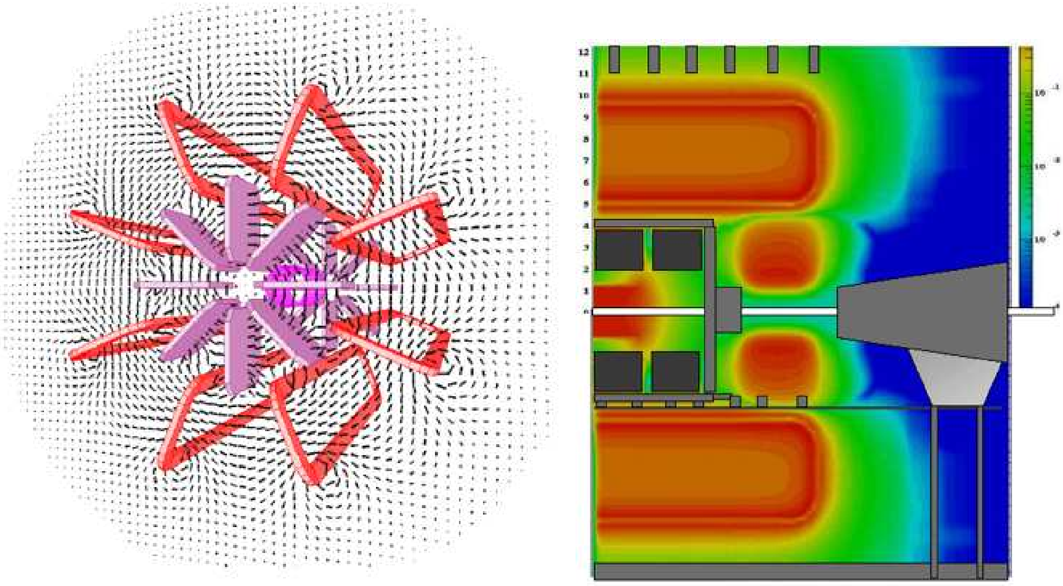

(a) Magnet Field Lines

(b) Magnetic Field Map

Figure 3.11 The ATLAS Magnet System

The CS and the electro-magnetic calorimeter share a common vacuum vessel in order to minimize material. The CS coil is a mixture of NbTi, Cu and Al, and its design is a compromise between operational safety and reliability. Each of the toroids consists of eight coils assembled radially and symmetrically (for mechanical statibility) around the beam axis. The ECT coil system is rotated by 22.5° with respect to the BT coil system in order to provide radial overlap and to optimize the bending power in the interface region of both coil systems.

3.2.5 Trigger and Data-Acquisition System

The need to process large amounts of data in the shortest possible time requires a highly efficient trigger system. The ATLAS trigger and data-acquisition system (DAQ) [12] is based on *three* levels of online event selection [33]. Each trigger level refines the decisions made at the previous level, applying additional selection criteria when necessary. The initial bunch-crossing rate is 40MHz: O(10^9) events per second at high luminosity. It must be reduced to O(100)Hz for permanent storage. This requires a rejection factor of 10^7 against "minimum-bias" events. A simplistic rendition of the ATLAS Trigger/DAQ system is shown in Figure 3.12.

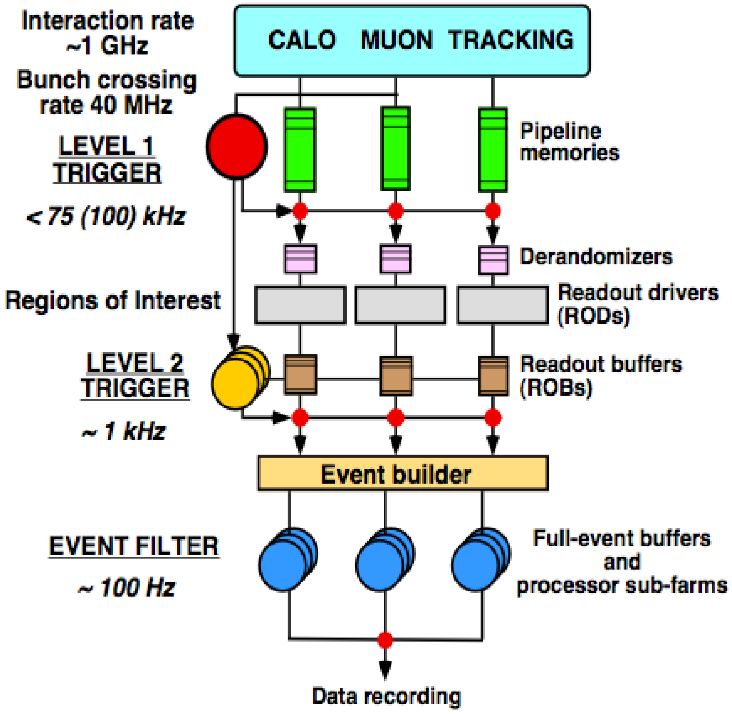

Figure 3.12 The three levels of the ATLAS trigger

The level-1 (LVL1) trigger [33] makes an initial selection based on information from the calorimeters and trigger chambers of the muon spectrometer looking for high p_T particles/jets and large missing transverse energy. It defineds the Regions of Interest (RoIs) in the entire detector. Different threshold combinations (*trigger menus*) can be set for different signatures. The LVL1 trigger should be able to reduce the event rate to 100 kHz with a latency of $\approx 2\mu$s. During this period, the information from all detectors is kept in pipelined memories. The level-2 (LVL2) trigger [12] refines the available information in the selected *Region-of-Interest* (RoI) using more detailed detector information provided by the LVL1 trigger. It is expected that LVL2 will reduce the rate to ≈ 1 kHz. The latency of this trigger varies from event to events and it will be in the range 1-10 ms. This level has access to all event data and bases its rejection power on the usage of the full granularity of the calorimeter information combined with the ID when possible. The level-3 trigger, or *Event Filter* (EF), is the last stage of the online selection. It will employ offline algorithms and methods combined with the most up to date calibration and alignment information including the magnetic field map. The EF will make the final selection of physics events which will be written to mass storage for subsequent offline analysis. The output from LVL2 is expected to be reduced to O(100)Hz ($\approx$ 100 MB/s) if the full event data are to be recorded. The EF will confirm the results from the LVL2 and will seed its own analyses in tandem.

3.2.6 Software for Simulation and Reconstruction Tools

Computing has proven to be crucial for the ATLAS experiment. A full gamut of tools has been developed to provide as accurate a description of the detector simulation and reconstruction conditions as possible. The work presented here uses version 10.5.0 of the ATLAS offline release software. The full detector simulation consists of three main steps. A short outline of these stages is given below; more detailed information can be found in [15].

- *Event generation*. The event generation phase is run separately for now in order to have a consistent input stream which can be used multiple times. Generators such as PYTHIA [1]

---

[1] PYTHIA is a program for the generation of high-energy physics events.

and HERWIG [2] are commonly used. During this step, a particle filter algorithm simulating a specific trigger level can be applied.

- *Detector simulation*. During the simulation, the particle four vectors stored in the GEANT KINE banks are projected onto the various sub-detectors and the information is recorded as HITS. In order to achieve a high level of accuracy, the geometry of the ATLAS sub-detectors has been described in extreme detail.

- *Reconstruction*. The reconstruction proceeds logically in three stages:

    1. *Digitization*. During this step the physical information registered as HITS is collected and reprocessed to produce a simulation of the real detector response of the read-out electronics in the actual experiment.
    2. *Stand-alone reconstruction*. The data related to each sub-detector are reconstructed separately. In this step, specific packages can be used. Packages have been developed to target electrons, photons, muons and jets independently of each other.
    3. *Combined reconstruction*. This step combines complete information from all sub-detectors, providing the final output file that is subsequently analyzed.

---

[2] HERWIG is a Monte Carlo package for simulating Hadron Emission Reactions With Interfering Gluons.

Chapter 4

The Liquid Argon Electromagnetic Calorimeter

4.1 General Description

Calorimeters, and especially the electromagnetic calorimeter (EMC), are expected to play a crucial role at the LHC. For ATLAS, the calorimeter system is the leading component for many measurements aimed at reconstructing physics events of great interest. The LHC experimental framework will be highly demanding, imposing constraints on the detectors in terms of special coverage, response speed and radiation tolerance amongst others. The ATLAS collaboration decided that a lead-Liquid Argon (LAr) sampling calorimeter with an accordion geometry would serve best. The specific geometry guarantees a full azimuthal coverage without cracks or dead zones. The following subsections delve into the requirements, characteristics and structure of the electromagnetic calorimeter, for it plays a pivotal part in this analysis.

4.2 Experimental Requirements of the ATLAS EMC

In general, the tasks of the calorimeters at hadron colliders regardless of their specific design are:

- Accurate measurement of the energy and position of electrons and photons.
- Measurement of the energy and direction of jets and of missing transverse momentum of the event.
- Particle identification, in particular distinction between electrons and photons on one hand and hadrons and jets on the other.
- Distinction between τ hadronic decays and jets.

- Event selection at the trigger level.

Due to the rigorous requirements imposed by the parameters of the LHC machine, such as the large center of mass energy (14 TeV), good performance is required over a large energy range. Given that the cross sections of the interesting processes are quite small, the luminosity (design luminosity $10^{34} cm^{-2} s^{-1}$) of the collider has to be very high, implying a significant number of pile-up events (see Figure 4.2) in space and time, as well high levels of radiation. At design luminosity, about twenty soft collisions will be produced, on average in every bunch crossing (every 25 ns).

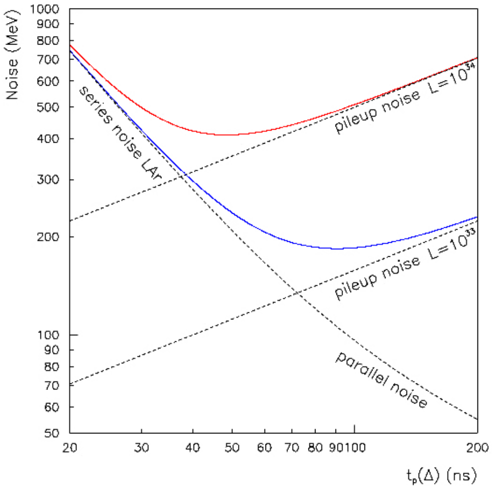

Figure 4.1 Optimization of the shaping time for high and low luminosity.

The EM calorimeter requirements specified by the physics are:

Rapidity coverage and granularity. In order to observe *rare* physics processes such as $H \rightarrow \gamma\gamma$ and $H \rightarrow 4e$ decays the largest possible acceptance will be needed. High granularity will help in the observation of these decays providing accurate position measurement and particle identification with fast response, low noise and good energy resolution.

Electron reconstruction capability from 1 to 2 GeV up to 5TeV. Soft electrons are an important ingredient for reconstructing the decay of b quarks. Tagging such decays is an important asset to a number of physics studies, including Higgs and t-quark decays. The 5 TeV value is set by the kinematic limit for the observable production of objects that may decay (semi-) leptonically.

Excellent energy resolution over the energy range 10-300 GeV. An energy resolution $\sigma/E \sim 10\%/\sqrt{E}$ with a constant term smaller than 1% is needed to achieve a mass resolution of 1% or better for the channels $H \rightarrow \gamma\gamma$ and $H \rightarrow 4l$. This level of precision on the Higgs mass also imposes limits on the maximum allowable signal non-linearity (0.5%), on the absolute precision of the EM energy scale (0.1$\%$), and on the angular resolution for the reconstruction of photons (50mrad/$\sqrt{E}$).

Linearity of response better than 0.5$\%$ in the energy range up to 300 GeV. This is to ensure optimal mass resolution for the $H \rightarrow \gamma\gamma$ and $H \rightarrow 4l$ channels. At higher energies, where the main issue considered is the measurement of the W' and the Z' mass parameters, this requirement is somehow relaxed.

Excellent γ/jet , electron/jet and τ/jet separation capability. This is mainly needed to suppress the background levels for physics processes for which the detection of electrons, γs or τs is crucial, such as the processes $H \rightarrow \tau\nu$ or $H \rightarrow \gamma\gamma$. At the LHC, the rate of isolated electrons with transverse momentum $p_T > 20$GeV/c is five orders of magnitude smaller than the rate of QCD jets with the same p_T. Therefore, a jet rejection factor of about 10^6 will be needed to extract a 90$\%$ pure inclusive electron signal.

4.3 The Physics of Shower Development

Before delving into the operational aspects of the ATLAS Liquid Argon calorimeter, it is necessary to review the interaction processes that play a role and depend on the particle and its energy. When a particle traverses matter, it will generally interact and lose (some fraction of) its energy in doing so. This section describes briefly the different processes by which particles can lose their energy and the scaling variables that allow to describe the EM shower development in a material-independent way.

When a high-energy electron/positron passes through matter, it can radiate a bremsstrahlung photon which can in turn give rise to an electron-positron pair. The subsequent particles continue with this development, and a cascade of particles with lower energy is formed. This process continues until the particles fall below the threshold for pair production.

The processes are described below:

- *Bremsstrahlung*. In their passage through matter, electrons and positrons radiate photons as a result of the Coulomb interaction with the electric fields generated by the atomic nuclei. The energy spectrum of these photons falls off as $1/E$. It extends, in principle, all the way to the energy of the radiating particle, but in general each emitted photon carries only a small fraction of this energy. In this process, the electron (or positron) undergoes a (usually small) change in direction (called multiple or Coulomb scattering). These radiative processes, which dominate the absorption of high-energy electrons and positrons, play a role for any charged particle traversing matter.

- *Photoelectric effect*. At low energies, this is the most likely process to occur. In this process, an atom absorbs the photon and emits and electron. The atom, which is left in an excited state, returns to the ground state by the emission of Auger electrons or X-rays. The photoelectric cross section is extremely dependent on the available number of electrons, and thus on the Z value of the absorber material. The cross section scales with Z^n, with n being between 4 and 5.

- *Rayleigh scattering*. This is a coherent process that is also important at low energies. In this process, the photon is deflected by the atomic electrons. However, the photon does not lose energy. As a consequence, this affects the spatial distribution of the energy deposition, but does not contribute to the energy deposition process itself.

- *Compton scattering*. In this process, a photon is scattered by an atomic electron with a transfer of momentum and energy to the struck electron sufficient to put the electron in an unbound state. This process is the most likely to occur for photons in the energy range between a few hundred keV and $\sim$ 5 MeV.

- *Pair production*. At energies larger than twice the electron rest mass, a photon may create, in the field of a charged particle, an electron-positron pair. Typically, more than 99$\%$ of the pairs are caused by nuclear electromagnetic fields. The cross section for pair production rises with energy and reaches an asymptotic value at very high energies ($>$ 1GeV). This cross section is related to the radiation length of the absorber material. Since the cross sections for the photoelectric effect and for Compton scattering decrease with energy, while the cross section for pair production increases, pair production is the most likely to occur at high energies.

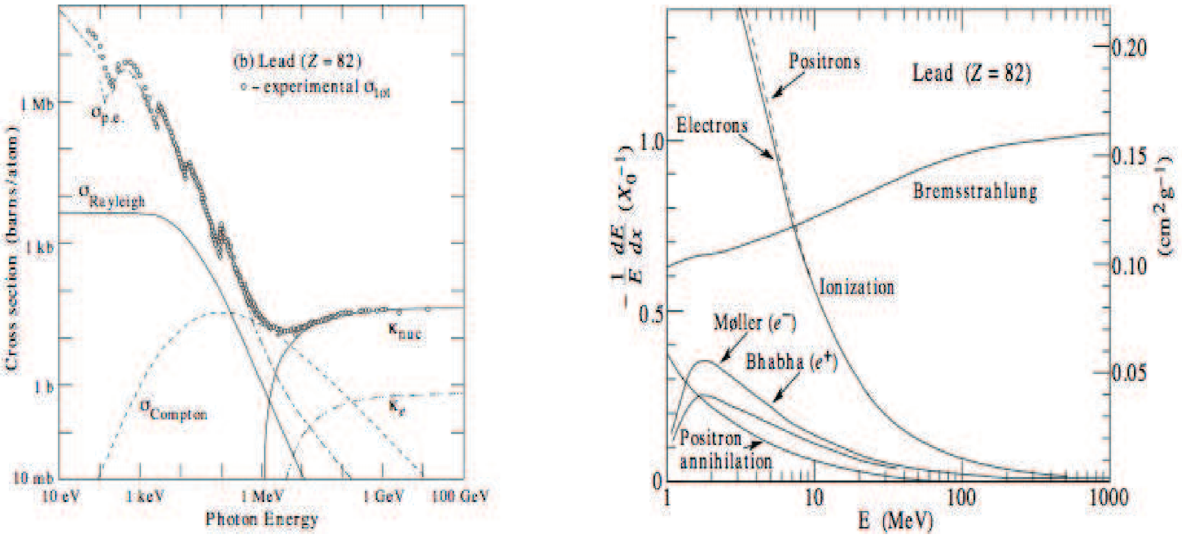

(a) Photon cross section as a function of the energy deposited in lead showing the contributions of the different processes

(b) Fractional energy loss of electrons per radiation length as a function of the energy in lead

Figure 4.2 Photon cross section and electron energy loss in lead. Figures obtained from [31].

A description of the material-independent scaling variables is given as follows:

- *Radiation length.* The radiation length is defined as the distance over which a high-energy ($\gg$ 1 GeV) electron or positron loses, on average, 63.3% (i.e. 1-e^{-1}) of its energy by bremsstrahlung. By expressing the dimension of the absorber material in units of X_0, material-dependent effects are, in first approximation, eliminated. For approximate calculation, accurate to within 3%, the Particle Data Group [31] recommends the following expression:

$$X_0 = \frac{716.4A}{Z(Z+1)ln(287/\sqrt{Z})} gcm^{-2} \tag{4.1}$$

  The radiation length for a mixture of different materials can be calculated as follows:

$$\frac{1}{X_0} = \sum_i V_i/X_i \tag{4.2}$$

in which V_i and X_i are the fraction by volume and the radiation length (expressed in mm) of the ith component of the mixture.

- *Molière radius*. This quantity is frequently used to describe the transverse development of EM showers. It is defined in terms of the radiation length X_0 and the critical energy ϵ_C, as follows:

  $$\rho_M = E_S \frac{X_0}{\epsilon_C} \tag{4.3}$$

  in which the scale energy E_S, defined as $m_e c^2 \sqrt{4\pi/\alpha}$, equals 21.2 MeV. On average, 90$\%$ of the shower energy is deposited in a cylinder with radius ρ_M around the shower axis.

4.4 Principle of Operation of the ATLAS Liquid Argon Calorimeter

The ATLAS electromagnetic calorimeter is a charge collection calorimeter [44]. Ionization charge liberated in the active medium (Liquid Argon) is the measured quantity (signal). It collects the ionization charge produced by charged shower particles. Given that liquid argon is relatively dense, there is no need for charge amplification in an avalanche[1] process, as in gas-based detectors. Liquid argon also gives enough charge to allow operation in the ionization chamber mode, which ensures a better response uniformity than gas-based detectors. Liquid sampling calorimeters are relatively uniform and easy to calibrate, given that the active medium is homogeneously distributed inside the volume and the signal collection is not subject to the cell-to-cell variations. Table 4.1 points to some important characteristics of liquid sampling calorimeters. The material properties of the calorimeter are listed in Appendix D.

The basic active element of any noble-liquid calorimeter consists of two parallel metal plates, between which a potential difference ΔV is applied. The gap between these plates is filled with the liquid sampling medium (Figure 4.4). In a standard liquid-argon sampling

---

[1] An avalanche occurs when the voltage between the anode-cathode pair is increased. The electrons produced in the primary ionization processes may acquire enough energy to be able to ionize molecules themselves. The electrons liberated in the secondary ionizations are also accelerated and produce, in turn, more ionizations, creating an avalanche.

Table 4.1 Characteristics of Liquid Sampling Calorimeters

Advantages	**Drawbacks**
Provide good energy resolution	Cryogenic equipment introduces additional dead material in front of the calorimeter (cryostat)
Stable response with time	Complex purification system
Radiation hard	Slow charge collection for classical liquid calorimeters

calorimeters, the alternating absorber and active layers are placed perpendicular to the direction of the incident particles. The ionization signal produced by the shower in the liquid-argon gaps is collected by the electrodes located in the middle of the gaps. These electrodes carry the high voltage, whereas the absorbers are at ground. The total charge collection time (500 ns) corresponds to about 20 LHC bunch crossings. Given the high event rates and the associated problems of pile-up, this is too long. In order to produce faster signals, a bipolar pulse shaping is applied with a shaping time t_p (Δ), of 45 ns. The resulting signal shape is shown in Figure 4.3, together with the triangular pulse shape typical for LAr calorimeters in which all the ionization charge is collected. In this figure successive LHC bunch crossings are indicated by dots. With this applied pulse shaping, the signal crosses the baseline after about 5 bunch crossings.

In applying this type of pulse shaping (that is, collecting a small fraction of the ionization charge) the signal-to-noise ratio might be expected to be worse than if all the ionization charge were collected. Eventually another complication appears at the LHC, arising from the increase of pile-up noise [2].

---

[2] Pile-up results from the energy deposited in the calorimeter by the particles produced in the numerous interactions taking place in each bunch crossing.

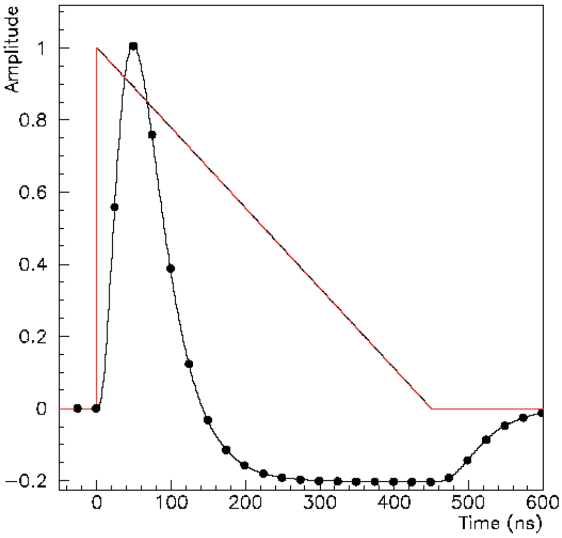

Figure 4.3 Signal shape as produced in the detector (triangle), and after bipolar shaping (curve with dots). The dots represent the position of the successive bunch crossings.

The necessary fast transfer is ensured by placing the absorber and gap layers perpendicular to the particle direction. In this way the signal from the collection electrons can be extracted directly from the front and back faces of the calorimeter and sent to the readout chain with a minimum number of cables and connections. Furthermore, in order to prevent incident particles from escaping through the liquid argon gaps without crossing the absorber, the electrodes are bent into an accordion shape, as illustrated in Figure 4.4 .

The ATLAS calorimeter takes advantage of this technique. The read-out electrodes are flexible three-layer Cu-Kapton printed circuit boards. The two Cu outer layers are connected to the HV, while the inner Cu layer, connected to the read-out channel, collects by capacitive coupling the current induced by electrons drifting in the liquid-argon gap.

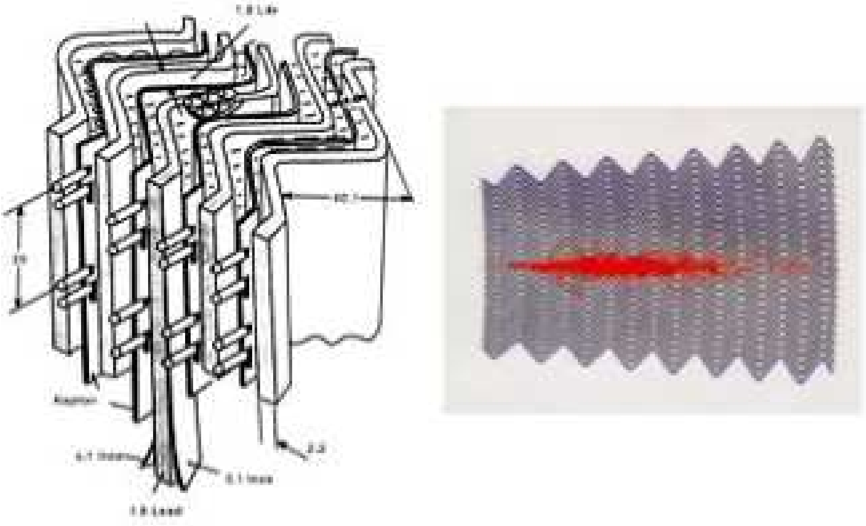

Figure 4.4 Sketch of the ATLAS Liquid Argon electromagnetic calorimeter accordion geometry (left); GEANT simulation of an electromagnetic shower developing in the EMC.

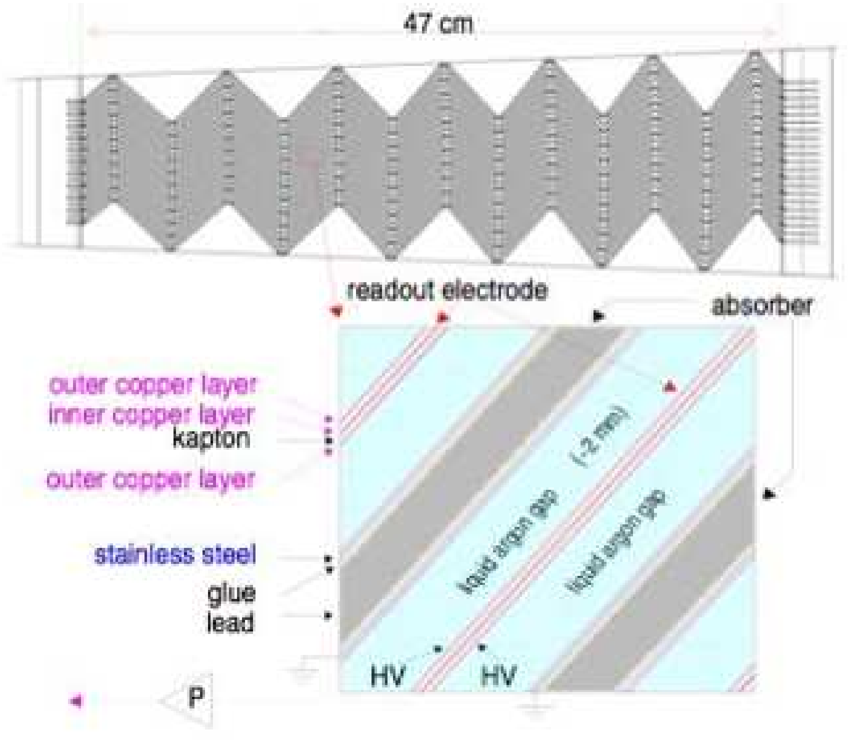

Figure 4.5 Detailed view of the EM barrel LAr electrodes.

In the ATLAS calorimeter, signal electrodes alternate with absorber plates. For each half-barrel ($0 \leq \eta \leq 1.45$), the electrode is divided into two separate elements, of size 1800 mm x 800 mm each, covering $0 \leq \eta \leq 0.8$ and $0.8 \leq \eta \leq 1.45$ respectively. The signal is extracted from the copper cells (see Figure 4.4, left) and brought to the front or back edge of the electrode. It then goes through the absorber G10 bars which are connected to the electronic boards. The electrodes are kept in place by means of honeycomb spacers. Figure 4.5 illustrates the electrode geometry of the ATLAS electromagnetic calorimeter.

The absorber electrodes are made of 1.5 mm (1.1 mm for $|\eta| > 0.8$) precision-rolled lead, sandwiched between two sheets of 0.2 mm thick stainless-steel. A layer of 0.13mm prepeg adhesive (0.33mm for $|\eta| > 0.8$ to compensate for the thinner lead), inserted between the lead and the stainless-steel, completes the absorber structure. The stainless steel is needed for mechanical strength and provides a better surface than unclad lead. The thinner lead for $|\eta| > 0.8$ increases the sampling fraction, and therefore compensates for the deterioration of the energy resolution due to the decrease of the sampling frequency with increasing rapidity.

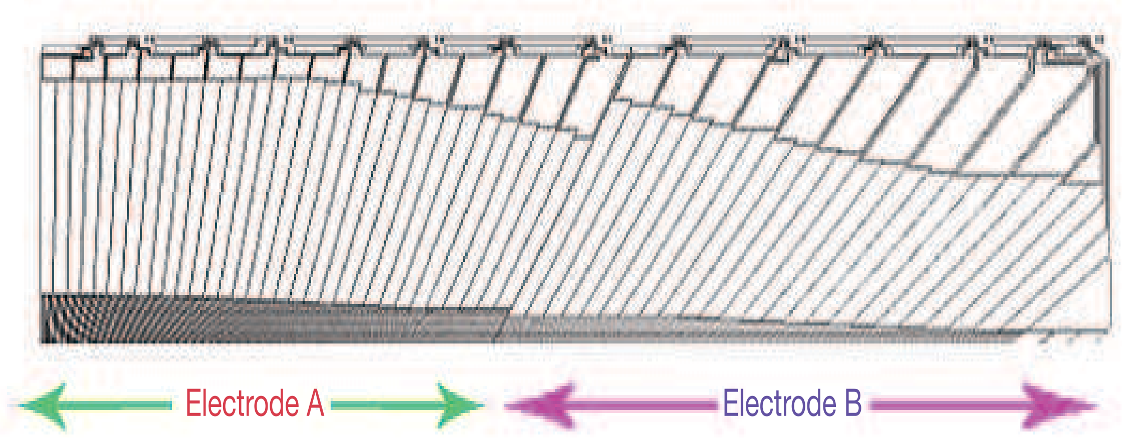

Figure 4.6 View of signal layer for barrel electrode.

The sampling fraction measures the ratio between the energy deposited by a Minimum Ionizing Particle (MIP) [3] in the active medium, and the total energy lost in the full detector (LAr

---

[3] The mean energy loss per unit path length, $< dE/dx >$, given by the Bethe-Bloch formula (see Appendix B) is often referred to as the *specific ionization* or the *ionization density*. Muons, or other particles with unity

gaps + passive lead absorbers). Maintaining a constant sampling fraction of the calorimeter as a function of radius, full projectivity in ϕ, and minimal density variation in ϕ, are three important requirements which have been considered in the optimization of the absorber design. The final optimization was achieved by varying the fold angles and pleat lenghts, as a function of radius (see Figure 4.5).

4.5 General Structure of the ATLAS EMC

The ATLAS EMC is a sampling calorimeter, consisting of a lead liquid-argon sampling structure with an accordion geometry. It is segmented into two parts: the barrel (EMB), that covers a pseudorapidity range $|\eta| < 1.375$, and the end-cap (EMEC), located in the region $1.375 < |\eta| < 3.2$. Each segment covers a full azimuth acceptance $0 < \phi < 2\pi$, providing complete ϕ symmetry without azimuthal cracks. They are housed in the barrel and end-cap cryostats shown in Figures 4.8(a) and 4.8(b). The barrel consists of two identical half-barrels separated by a small gap (6mm) at z = 0. Each end-cap calorimeter (see Figure 4.10(a)) is mechanically divided into two coaxial wheels: an outer one covering the region $1.375 < |\eta| < 2.5$ and an inner wheel covering the region $2.5 < |\eta| < 3.2$.

---

charge such as pions, with an energy corresponding to that at which $< dE/dx >$ reaches its minimum, are called *minimum ionizing particles* or *MIPs* [44]

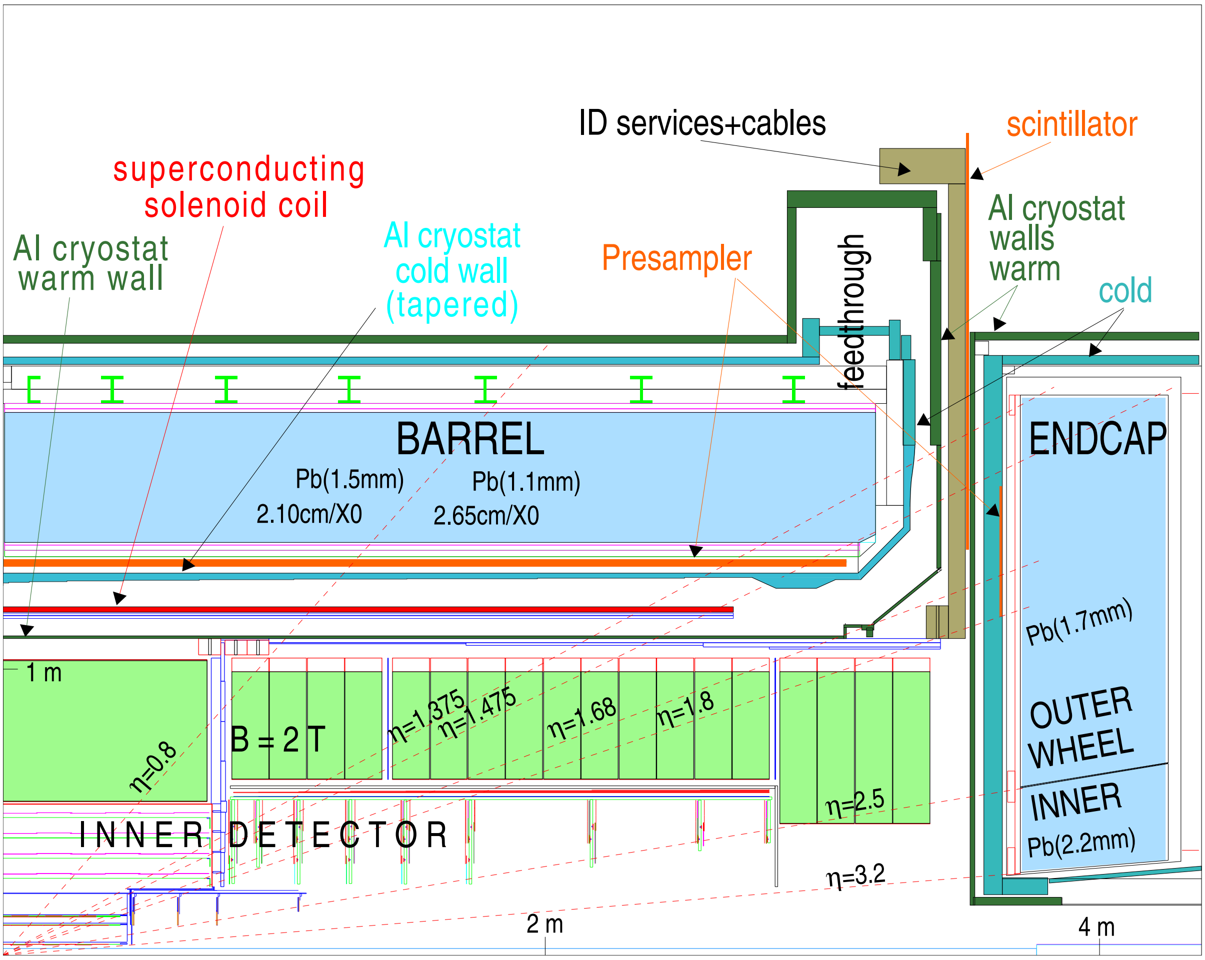

Figure 4.7 Transverse view of half-barrel of EMC

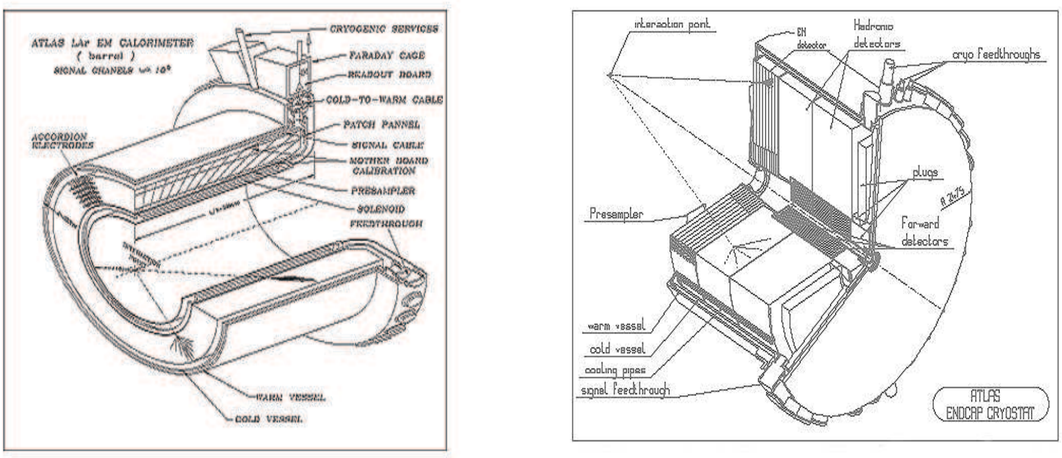

(a) Electro-magnetic Barrel encased in cryostat

(b) End-cap cryostat with its one EMEC wheel, two HEC wheels, and integrated FCal, with one electro-magnetic and two hadronic modules.

Figure 4.8 Perspective view of the half cryostat barrels for the barrel and end-cap regions.

The EMC barrel calorimeter is segmented in turn into three longitudinal sections (Figure 4.9) defined as follows:

S1 ('Front' or 'Strips'). This first section is made up of narrow strips with a pitch of 4mm in the η direction. It has a constant thickness of $6X_0$ (upstream material included) as a function of η. This section acts as a preshower detector, enhancing particle identification ($\gamma/\pi_0, e/\pi$ separation, etc.) and providing a precise position measurement in η. It has a granularity $\Delta\eta \times \Delta\phi = 0.003125 \times 0.1$.

S2 ('Middle'). This section is transversally segmented into square towers of size $\Delta\eta\times\Delta\phi = 0.025 \times 0.0245$ ($\sim 4 \times 4cm^2$ at $\eta = 0$). The depth of each tower is between 16 and 18 X_0 and their function is to collect most of the e/γ shower energy. The total calorimeter thickness up to the end of this section is $24X_0$.

S3 ('Back'). With a granularity of $\Delta\eta \times \Delta\phi = 0.05 \times 0.025$ and a depth varying between $2X_0$ and $12X_0$, this section is used to sample high energy showers and helps to separate hadronic from electromagnetic particles.

In the region $|\eta| < 1.8$, a presampler detector precedes the calorimeter. It is installed immediately behind the cryostat cold wall and it is used to correct for the energy lost in the material upstream of the calorimeter (mainly the inner tracking system, the LAr cryostat and the solenoid coil).

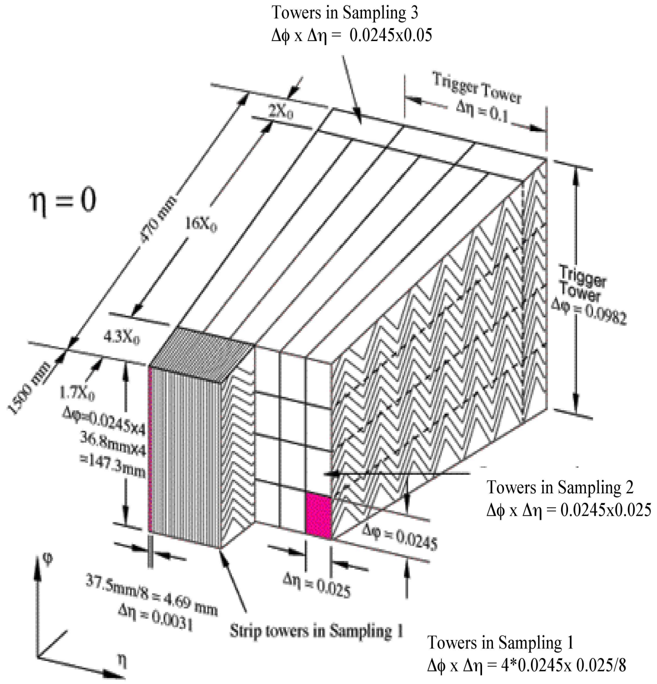

Figure 4.9 Sketch of the accordion structure of the EM calorimeter per sampling.

Table 4.2 Granularity of the EM calorimeter (η, ϕ)

η **range**	**0 to 1.4**	**1.4 to 1.8**	**1.8 to 2.0**	**2.0 to 2.5**	**2.5 to 3.2**
Presampler	0.025×0.1	0.025×0.1			
Sampling 1	0.003×0.1	0.003×0.1	0.004 × 0.1	0.006×0.1	0.1×0.1
Sampling 2	0.025×0.025	0.025×0.025	0.025 × 0.025	0.025×0.025	0.1×0.1
Sampling 3	0.050×0.025	0.050×0.025	0.050 × 0.025	0.050×0.025	
Trigger	0.1×0.1	0.1×0.1	0.1×0.1	0.2 × 0.2	
Readout channels	110208	25600	12288	24064	1792

There are 2 end caps (Figure 4.10(a)). Each one contains the electromagnetic wheel, the two hadronic wheels and the forward calorimeter. They are mechanically divided into eight wedge-shaped modules (Figure 4.10(b)). In order to accommodate the accordion geometry in this region, the absorber plates are arranged radially like the spokes of a bicycle wheel and the accordion waves run parallel to the beam axis. The amplitude of the waves scales with the radius. Due to construction reasons behind the absorber plates, the ratio of inner to outer radius of a given plate is limited to about three. As a consequence each end-cap EM wheel consists of two concentric wheels, the large one spanning from $1.4 \leq \eta \leq 2.5$, and the small one from $2.5 < \eta \leq 3.2$.

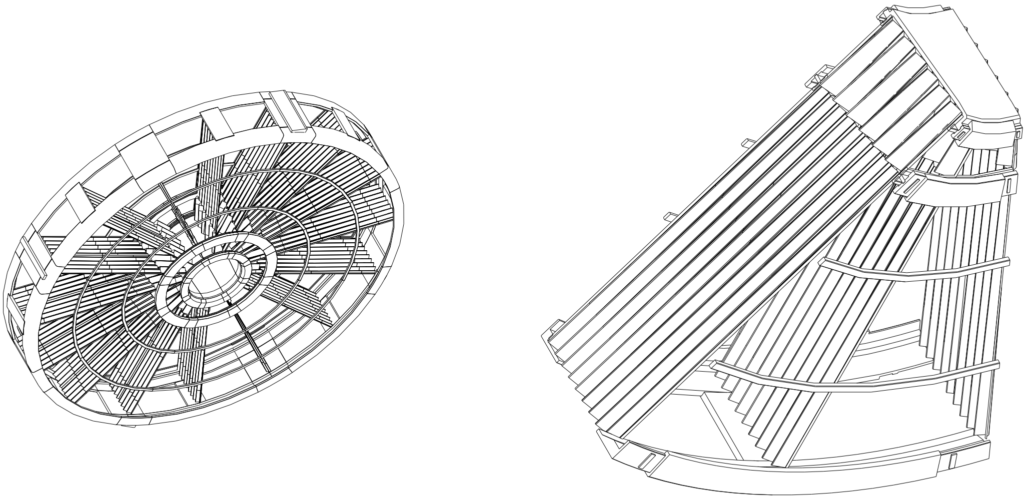

(a) General view of an electromagnetic end-cap calorimeter containing only a few absorbers.

(b) Schematic view of an electromagnetic end-cap module. Only 3 absorbers out of 96 (in the outer wheel) are represented.

Figure 4.10 General view of an electromagnetic end-cap calorimeter and end-cap module

4.6 Energy Resolution of the ATLAS EMC

One of the issues that ATLAS will have to face is the fact that the resolution of its electromagnetic calorimeter is determined and limited by fluctuations that directly result from the reality that the shower energy is sampled (*sampling fluctuations*). Furthermore, the operation of liquid argon in the ionization chamber mode will add the contribution from the electronic noise, which is a dominant and limiting factor of the energy resolution at low energies. Sampling fluctuations are dominated by fluctuations in the number of different shower particles contributing to the signals. The relative width of the distribution is equal to $\sqrt{n}/n = 1/\sqrt{n}$ where n is the number of charged particles. The relative precision of the energy measurement with a calorimeter can therefore be expressed as:

$$\frac{\sigma_E}{E} = \frac{a}{\sqrt{E}} \tag{4.4}$$

Extrapolating equation (4.4) to the ATLAS EM calorimeter and adding the contribution for the electronic noise ($\frac{b}{E}$) and a constant term c to account for instrumentation effects independent of the development of the shower, we get:

$$\frac{\sigma_E}{E} = \frac{a}{\sqrt{E}} \oplus \frac{b}{E} \oplus c \tag{4.5}$$

One of the methods proposed to reduce these fluctuations, improving the EM energy resolution, is to increase the sampling fraction. An increase in the sampling fraction is equivalent to an increase in the amount of active material in the volume in which the showers develop. Though, too big a sampling fraction can also interfere with the calorimeter compensation.

This study incorporates the noise and constant terms derived with data from the 2004 test beam.

4.6.1 Noise Contribution to the Energy Resolution

The contribution from electronic noise is an instrumental effect that will affect the energy resolution. It is decoupled from the sampling term a, for it does not scale with $E^{-1/2}$. This means that the relative contribution to the total energy resolution is energy dependent. Most effects, namely those causing energy-independent fluctuations, will dominate the energy resolution at very high energies where the contributions from the processes governed by Poisson statistics are small. However, the electronic noise is an exception to this rule, since it dominates the resolution at low energies.

The signals produced by sampling calorimeters correspond to the charge collected during a certain period, called the *gate time*. Since the detector has a certain capacitance, there is a contribution of the electronic noise to the signals; meaning that in the absence of a showering particle, the integrated charge collected during this gate time will fluctuate from event to event.

The standard deviation of these fluctuations, σ_{Noise}, is measured in units of charge and is converted into an equivalent amount of calorimetric energy (ENC [4]) that depends on many factors (e.g. gate time, detector capacitance, properties of amplification electronics). σ_{Noise} corresponds to a certain fixed energy. The contribution of this noise to the energy resolution, σ/E, scales like E^{-1}.

Figure 4.11 illustrates the rms of the electronic noise for the ATLAS calorimeter as a function of pseudorapidity for three different cluster sizes.

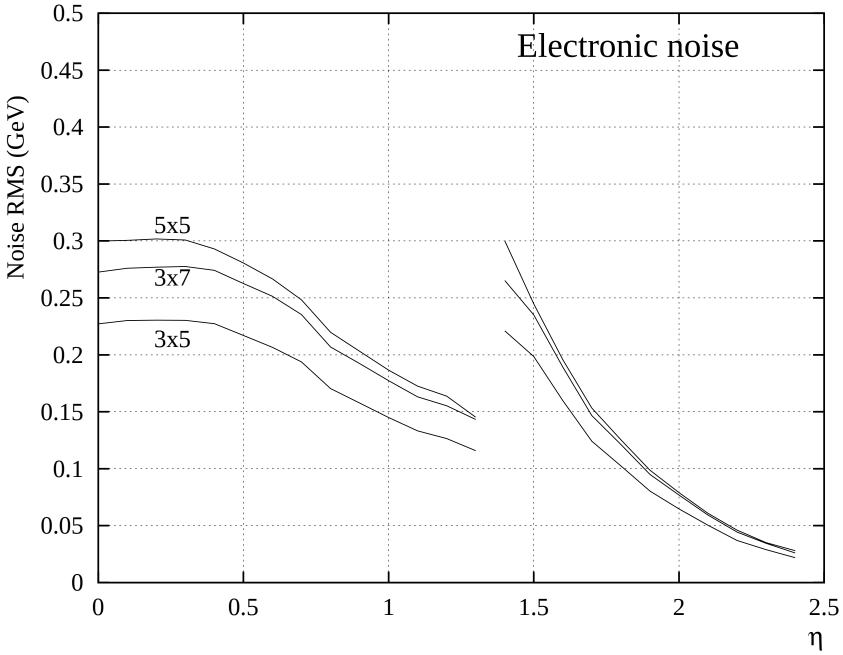

Figure 4.11 RMS of the electronic noise as a function of pseudorapidity for 3 x 5, 3 x 7 and 5 x 5 cluster sizes.

4.6.2 Constant Term

To meet the LHC physics requirements outlined in Chapter 3, the global constant term of the energy resolution over the full calorimeter coverage, must be equal to or smaller than 0.7$\%$. In order to achieve this, the strategy is to have a small constant term, by construction, over a

---

[4] For the case in which the capacitance is not matched to the ionization chamber gap capacitance, the relationship for the equivalent noise charge due to series noise is: $E\bar{N}C^2 = \frac{1}{2}e_n^2 C_{tot}^2 I_1$, in which e_n is the series noise voltage density for the amplifier, C_{tot} is the sum of the detector capacitance and the channel capacitance of the transistor at the amplifier input, and I_1 is the series noise integral. [5]

limited region of the calorimeter coverage (the so-called ’local’ constant term). The calibration of long-range non-uniformities can be done *in situ* by using physics samples (e.g. Z$\rightarrow$ ee events).

Many sources of non-uniformity contribute to the local and overall constant terms of the calorimeter. They are listed below and are based on the experience gained in the construction and during the test of various prototypes. They are grouped by range.

- Short Range:
    - Detector Geometry
    - Mechanics
    - Calibration
- Long Range:
    - Signal dependence of LAr impurities
    - Signal dependence on temperature
    - HV Variations
    - Others (e.g. upstream material, mechanical deformations, cable lengths.)

The goal is to achieve a local constant term over a calorimeter region of size $\Delta\eta \times \Delta\phi = 0.2 \times 0.4$, which corresponds to the size of a motherboard in the middle compartment, or 0.5 $\%$. In the absence of imperfections in the detector mechanics and electronics, a constant term of about 0.25$\%$ was obtained for particles incident in a given cell of the barrel ([13], Section 4.3.5).

4.7 Effects of Upstream Material on the EM Energy Measurement

The electromagnetic calorimeter has a substantial amount of ’dead’ material installed upstream (Figure 4.13). The presampler serves primarily to alleviate the problems caused by the material. The principle of a presampler detector is based on the fact that the energy deposited in a thin active medium is proportional to the energy lost in the passive medium in front of it. The difference with the case of a sampling calorimeter is that the passive material, the ’absorber’, is very thick, typically about 1-2X_0 and that there is only one layer of passive and active material.

If an electron passes through the passive material in front of the presampler, it continuously loses energy by ionization. The total deposited energy in the passive material is approximately constant and can be easily calculated assuming the energy is lost by a MIP. The electrons can also lose energy by bremsstrahlung. The emitted photons will not deposit any energy in the presampler. Their mean free path until the creation of an electron-positron (e^+e^-) pair is $\frac{9}{7}X_0$.

The pair can be produced in the active material, in the active medium of the presampler or in the calorimeter. The particles can still undergo bremsstrhalung or pair production, developing an electromagnetic shower. The shower development process stops when the energy of the particle becomes lower than a threshold (critical energy E_0 [5]) and the ionization process takes over.

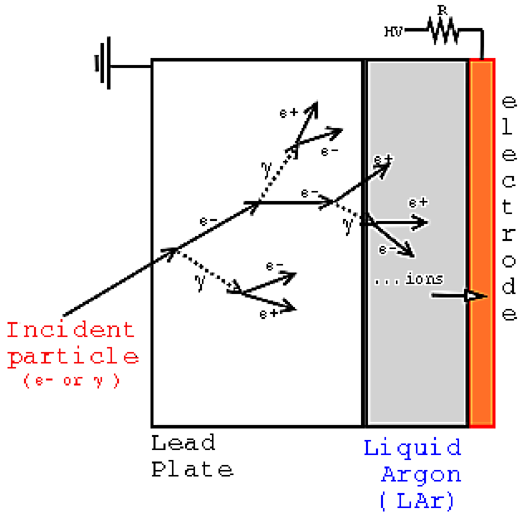

Figure 4.12 EM shower development

---

[5] For electrons, the critical energy is approximately $E_c^{elec} = \frac{610MeV}{Z+1.24}$

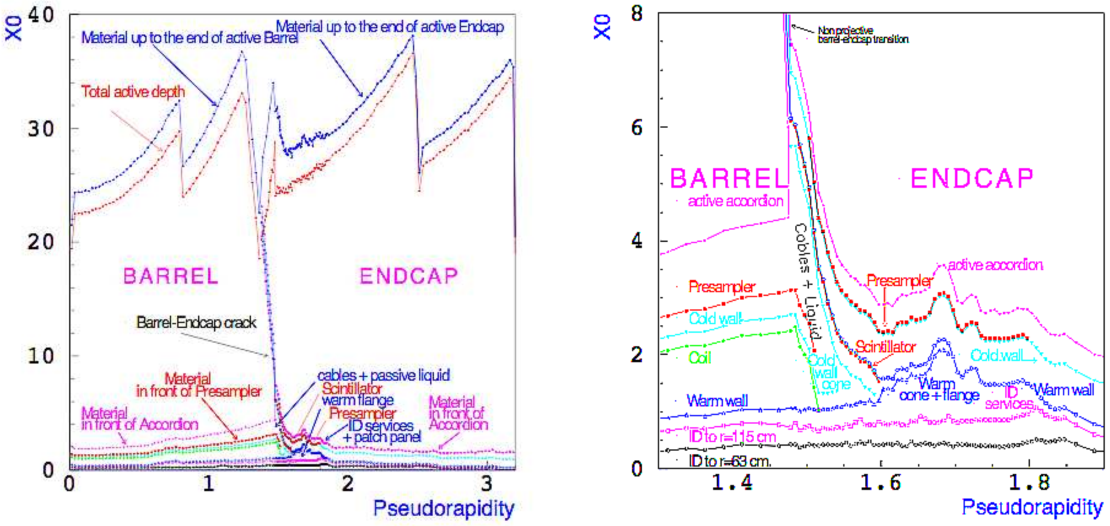

(a) Total thickness (in radiation lengths) of the ATLAS EM calorimeter as a function of rapidity.

(b) Breakdown of the material distribution in front of the EM calorimeter at the barrel/end-cap transition.

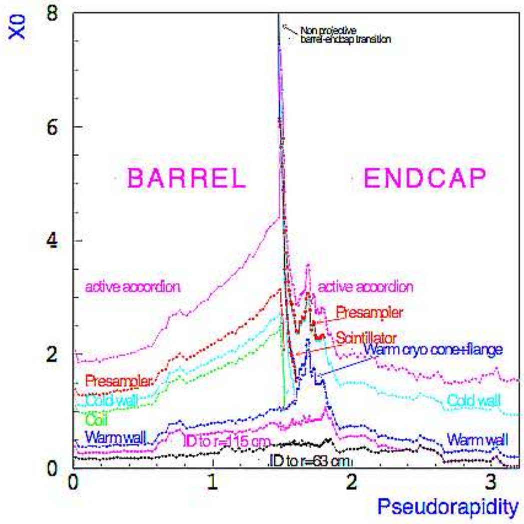

(c) Breakdown of the material distribution in front of the EM calorimeter, over the full rapidity coverage.

Figure 4.13 Material Distribution

4.8 Calorimeter Corrections

The precise calibration of the ATLAS calorimeter during the commissioning phase and during the actual data taking is an important issue for many physics analyses. Two of the most serious problems are:

- The equalization of response of different physical regions of the EMC.
- The correction of (mostly) upstream material effects during the energy reconstruction through the application of longitudinal weights for the different sampling of the LAr calorimeter.

These issues have been addressed in Technical Design Reports ([6] and [8]), while understanding of the calorimeter response has been the main goal of several ATLAS LAr Calorimeter Test Beams [25] [28].

4.8.1 Cluster Level Corrections

The energy deposition of an electron or photon is stored in the cells of the EMC. These are then collected in clusters (of variable size [6]) built around the cell (including the shower barycenter) in the middle compartment. Corrections directly related to hardware variations or defects are applied to the cell energies. Only a few ones are present in the Monte Carlo simulation.

A number of cluster level e/γ corrections are applied during reconstruction using the ATLAS software framework (ATHENA). Such corrections are applied at the cluster level because they are particle type and/or clustering scheme dependent. The corrections implemented in release 10.5.0 are:

- **S-shape correction:** corrects the reconstructed position of an EM cluster along η. Within a sampling the cluster position is the energy-weighted average of the positions of the cells

---

[6] Clusters in the second sampling can be made up of 3x3, 3x5, 3x7, 5x5 cells in $\Delta\eta = 0.025$ and $\Delta\phi = 0.025$ bins

included in the cluster. Due to the steeply falling lateral profile of the EM shower, the finite granularity of the calorimeter induces a systematic shift of the shower barycenter toward the center of the cell, an effect known as S-shape. In the case of the ATLAS accordion calorimeter, this is specially true in the η direction, since in the ϕ direction the accordion waves induce a better energy sharing between neighbouring cells.

- ϕ **Modulation:** corrects the energy response as a function of the cell impact point in the ϕ-direction. The variation of the cell energy response is caused by the varying amount of passive material crossed by an incident particle due to the accordion geometry.
- **Offset in ϕ:** corrects the cluster position along the ϕ-direction for effects caused by the accordion shape of the cells and the shower depth. The position of a cluster in ϕ is measured in the middle compartment.
- η **Modulation:** corrects the energy response as a function of the cell impact point in the η-direction.
- **Out-of-cone correction:** corrects the energy for finite lateral containment, taking into account the energy depositions which fall outside the clustering cone. Though this correction has strong correlation with the longitudinal weights, it is not absorbed in the overall energy scale.

4.8.2 Calibration for Electromagnetic Showers

The electromagnetic shower energy response of a calorimeter with longitudinal segmentation is affected by several effects that deteriorate the total energy resolution and alter the value of the total energy. Some of these effects can be *reversed* by the application of a layer weighting technique where the weights are known as *longitudinal weights*.

Given the longitudinal segmentation of the calorimeter, the reconstructed e/γ energies are a function of the responses of the different samplings. The standard function (or parameterization) for the reconstructed energy is a simple weighted sum of the individual sampling responses given by:

$$E_{Rec} = \lambda \times (b + W_0 E_{PS} + E_1 + E_2 + E_3) \tag{4.6}$$

where b is an offset with the units of energy, and W_0 is the factor correcting for losses upstream of the presampler.

In the presence of η-dependent material thickness upstream of the EMC, the standard parameterization may need modification in order to preserve a good energy linearity and resolution [36]. These weights are, in principle, particle dependent. The ones implemented in the ATHENA framework have been derived using electrons [25]. One of the goals of the present study is to derive these weights for test beam photons using the available Monte Carlo tools as well as the test beam data.

4.8.3 Back Leakage

Given that the electromagnetic shower is not fully contained, there is a fraction of energy that leaks out of the back of the calorimeter, notwithstanding its thickness (about 22 X_0 at η =0.4). Previous studies [36] have shown that 20 GeV electrons deposit approximately 100 MeV behind the last sampling of the calorimeter, while for 180 GeV electrons, the leakage can be about 1.2 GeV. Therefore about 0.5$\%$ to 0.7$\%$ of the electron energy is lost behind the calorimeter.

At lower rapidities, where the thickness of the calorimeter is reduced, significant fluctuations of the leakage are observed. This can be corrected on an event-by-event basis. There are two variables sufficiently correlated to the leaking energy to be used: the energy in the back compartment and the mean shower depth. The last one is defined by:

$$< l >= \frac{\sum_{i=0}^{3} E_i l_i}{\sum_{i=0}^{3} E_i} \tag{4.7}$$

where E_i is the energy in each compartment and l_i is the position of each compartment in radiation lengths. Figures 4.14 illustrates the method above described for 100 GeV electrons.

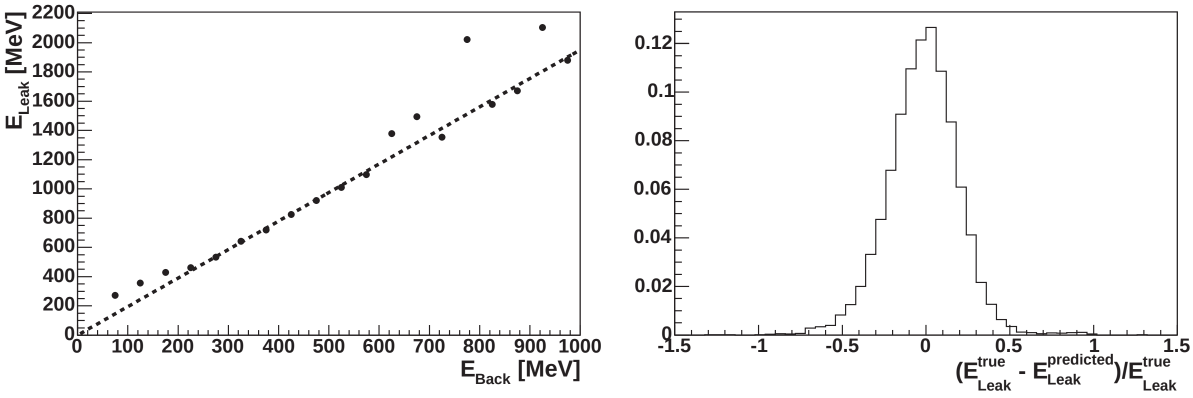

(a)

(b)

Figure 4.14 (a) Correlation of the energy deposit in the back compartment and the leaking energy for 100 GeV electrons at η = 0.4. (b) Accuracy of the leakage correction using the back compartment [36].

4.8.4 Effects of the Charge Collection

Due to the geometry of the electrodes [6] in the liquid argon calorimeter, accompanied by non-uniformities in the electric field and edge effects, there are ionization charge losses leading to a decrease in the calorimeter visible energy. This effect, which is η and ϕ dependent, accounts for 6-7$\%$ of the energy loss in the accordion region. In addition, there is a loss of amplitude in the ionization charge pulse due to the LC nature of the electron along the path of the pulse to the front end electronics (FEE). This accounts for a 3-5$\%$ loss that is corrected by the Optimal Filtering Coefficient (OFC) method. Both of these effects are simulated in detail in the ATLAS simulation and digitization processes.

The total combined effect for the presampler is 0.8 and for the accordion is 1.102 [38]. These factors are obtained from the MC itself; however, they contain a difference in the visible energy between data and MC which is about 2$\%$ (Geant4 version geant4-07-01). This last factor was extracted independently using electron beam runs from Period 5 of the combined test beam. It carries a systematic error ($<$0.3$\%$) due to the uncertainties in the absolute beam energy scale.

Chapter 5

Signal Reconstruction and Electronic Calibration of the EM Calorimeter

This section aims to give a detailed account of the methods used to perform the electronic calibration of the ATLAS electromagnetic calorimeter. The physics goals imposed by the LHC, as well as the high energy and large luminosity of the collider, set new demands on calorimeter read-out electronics. On the other hand, in order to guarantee good energy resolution over the entire energy range, the constant term in the resolution must be kept small ($< 0.7\%$). Part of this constant term stems from the accuracy with which the electronics chain is calibrated. It is then imperative that the contribution from the constant term coming from the calibration system be less than 0.25$\%$ for the EM calorimeters, less than 1% for the HEC and less than 2% for the FCAL.

5.1 Signal Read-out Scheme

Signals from the detector are processed in various stages before being read out by the DAQ system. The logical flow and the basic elements of the system are shown in Figure 5.1 . The first part of the electronic system is located inside the cryostat (*cold electronics*) and it is responsible for signal collection. The second part is placed directly on the calorimeter, outside the cryostat (*front-end electronics*) and provides amplification, shaping and digitization of the physics signals (see next section). The remaining part is located far from the detector, in the counting room, and performs signal processing, system control and monitoring.

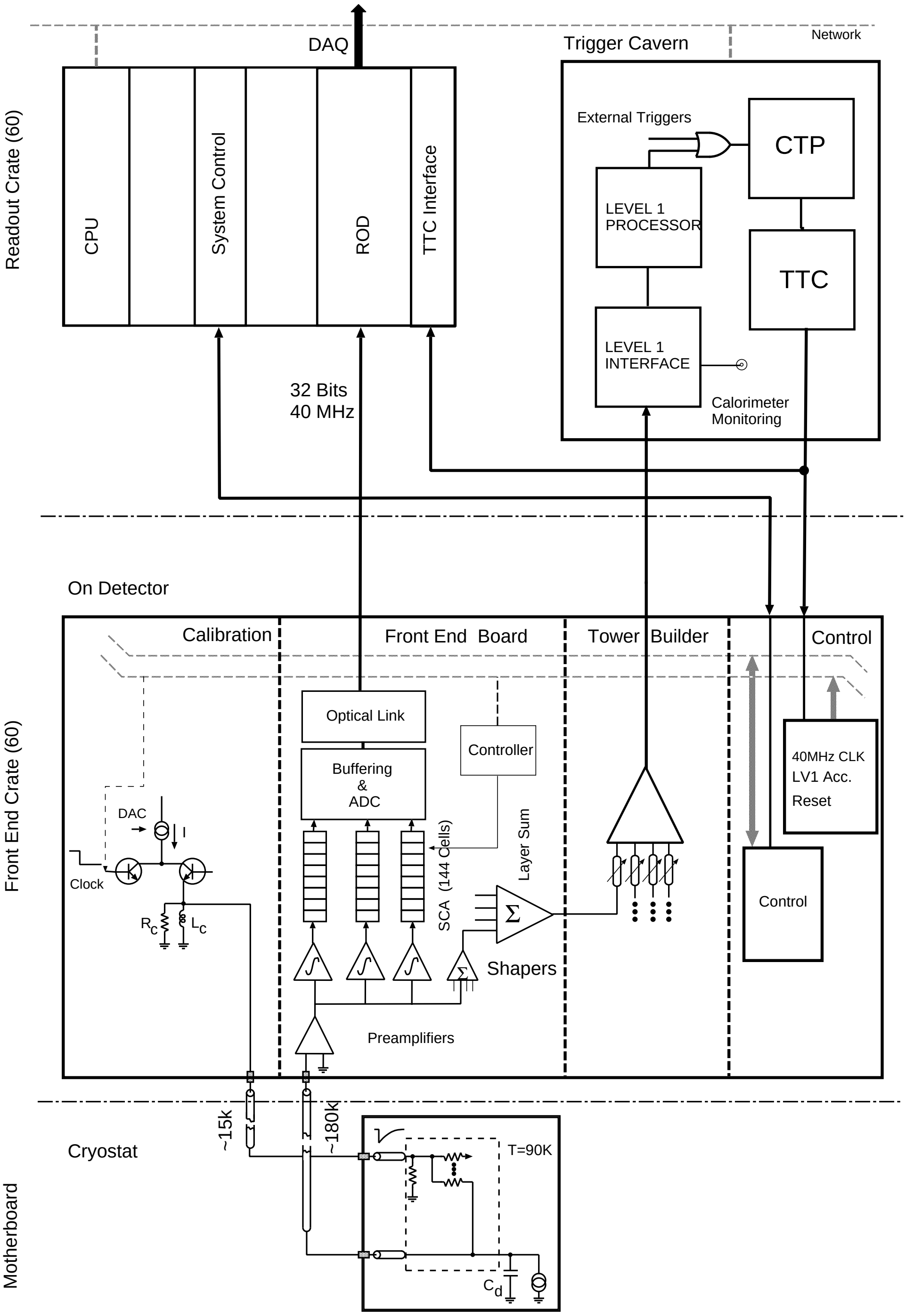

Figure 5.1 Block diagram of the read-out electronics. In the drawing, warm preamplifiers are located on the front-end board, which is the case for the EM and FCAl calorimeters. For the hadronic end-cap calorimeter, a preshaper - that interfaces preamplifiers located in the liquid argon to the standard shaper chip - replaces them.

5.2 Electronics Calibration

5.2.1 Calibration System

One of the important advantages of liquid argon calorimetry is the stability and uniformity of the ionization signal. In order to exploit this advantage, it is necessary to provide a very precise system to calibrate the electronics chain. This will ensure, as previously stated, that the constant term in equation (4.5) will remain small. The requirements demanded by the physics on the calibration system are as follows:

1. The dynamic range of the system must allow for matching the maximal current of the preamplifier (up to 10 μA in the EM calorimeter). At the low end of the energy scale, the system must permit the understanding of the response down to the level of a minimum ionizing particle energy deposition.
2. The dynamic range should be in one linear scale. This will allow inter-calibration of the three gains of the shaper.
3. The signal shape should be as close as possible to the real signal given the fact that the charge is not totally integrated. The rise time should be less than a few nanoseconds and the decay time should be close to the drift time of the signal induced by incident particles.
4. The relative timing between the calibration and the physics needs to be adjusted in order to provide best accuracy with the minimum number of calibration parameters.
5. The calibration elements should be radiation tolerant and flexible enough to allow for the calibration events taking during the physics runs.

5.2.2 Calibration Signal

An accurate electronics calibration is achieved by making the calibration signal resemble the physics signal as much as possible. The calorimeters deliver a triangular shape signal with a fast rise time (a few ns) (see Figure 4.3) , decreasing to zero at the end of the drift time of ionization electrons in liquid argon ($\sim$ 450ns).

5.2.3 Read Out Chain

The ionization signal collected by the electrodes in the calorimeter is brought out of the cryostat via cables to the front end crates (FEC). These crates, located on the cryostat, house both the Front End Boards (FEBs) and the calibration boards.

On the FEB, the calorimeter signals are received, amplified, split into three gain scales (1:9.2:92, called low, medium and high gain) and shaped with a bipolar shaping function. For any given channel, the signals are then sampled at the bunch crossing frequency of 40 MHz and stored in an analog pipeline (Switched Capacitor Array) until the trigger decision. Upon acceptance of a Level-1 trigger, the samples (N) are digitized by a 12-bit ADC. This digitization is done either on each gain or on the best gain according to a hardware gain selection. The decision is based on the amplitude of a fixed sample in the medium gain. The digitized samples are then stored in small digital memories on the FEB before optical transmission to the Read Out Driver (ROD) module.

The response dispersion of the electronics read-out is about 2%. To account for such an effect and for the different detector capacitances of each calorimeter cell, the calibration board provides a signal to all channels that resembles closely the calorimeter ionization signal. The principle of the calibration is illustraded in Figure 5.2.4. Precise DC current I_p is generated and flows into an inductor. When a pulse command is applied on the transistor Q_2, the transistor Q_1 is cut off and the current is diverted to ground. The magnetic energy stored in the inductor produces a fast voltage pulse with an exponential decay across the cable impedance and a 50 Ω termination resistor in parallel. This pulse is propagated inside the cryostat through a 7m long 50 Ω cable and is applied across a precise injection resistor R_{inj} (0.1%) in the cold on the motherboards, close to the electrodes. This is done in order to preserve the pulse uniformity of the board, guaranteeing a small sensitivity of the amplitude to the exact value of the cable characteristic impedance. The amplitude uniformity dispersion is better than 0.2%. One calibration signal is distributed through precise resistors 8 (32) calorimeter cells for the middle (front) compartment whose location is chosen such that cross-talk can be studied.

5.2.4 Cross-talk

The read-out signal of the calorimeter cells is affected mostly by capacitive cross-talk [20], which is the dominant coupling between the finely segmented strips of the first sampling. This is not the case for the middle and the back samplings, where the inductive coupling dominates.

Detailed measurements have been performed during previous test beams and a cross-talk map shown in Figure 5.2 has been produced. The largest cross-talk (about 7%) can be observed between neighboring strip cells.

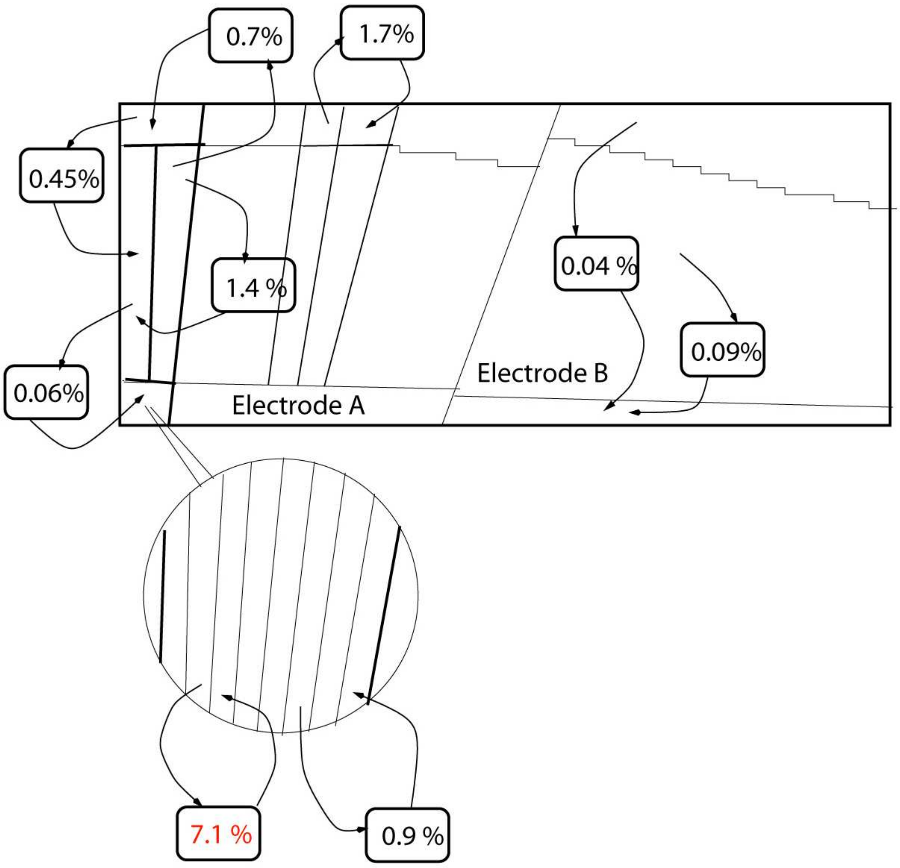

Figure 5.2 Cross-talk measured in module M13

Further details on the electronic calibration can be found in [17].

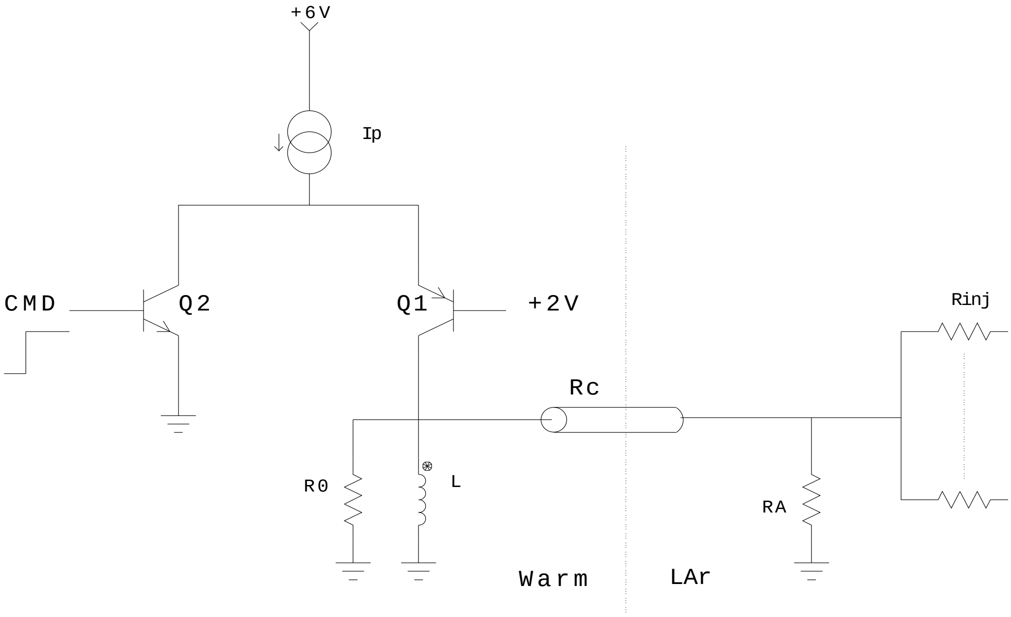

Figure 5.3 *Principle of the calibration.* The calibration pulse is created when the current is switched from Q1 to Q2, arising from the electro-magnetic energy stored in the inductor L. The cable, with characteristic impedance R_c, transports the signal to a network of resistors connected in the cold to the detector electrodes.

5.3 Cell Energy Reconstruction

The reconstruction of the cell energy in ATLAS is done at the level of the ROD (Read Out Driver). The RODs receive the raw data and reconstruct the energy (E_{Rec}) and the time of flight (τ) of the particle using the optimal filtering technique (see Section 5.5). The reconstructed energy has the following expression:

$$E_{rec} = f \sum_{0 \leq i < Sample}^{i} a_i (ADC_i - Pedestal) \tag{5.1}$$

$$\tau . E_{rec} = f \sum_{0 \leq i < Sample}^{i} b_i (ADC_i - Pedestal) \tag{5.2}$$

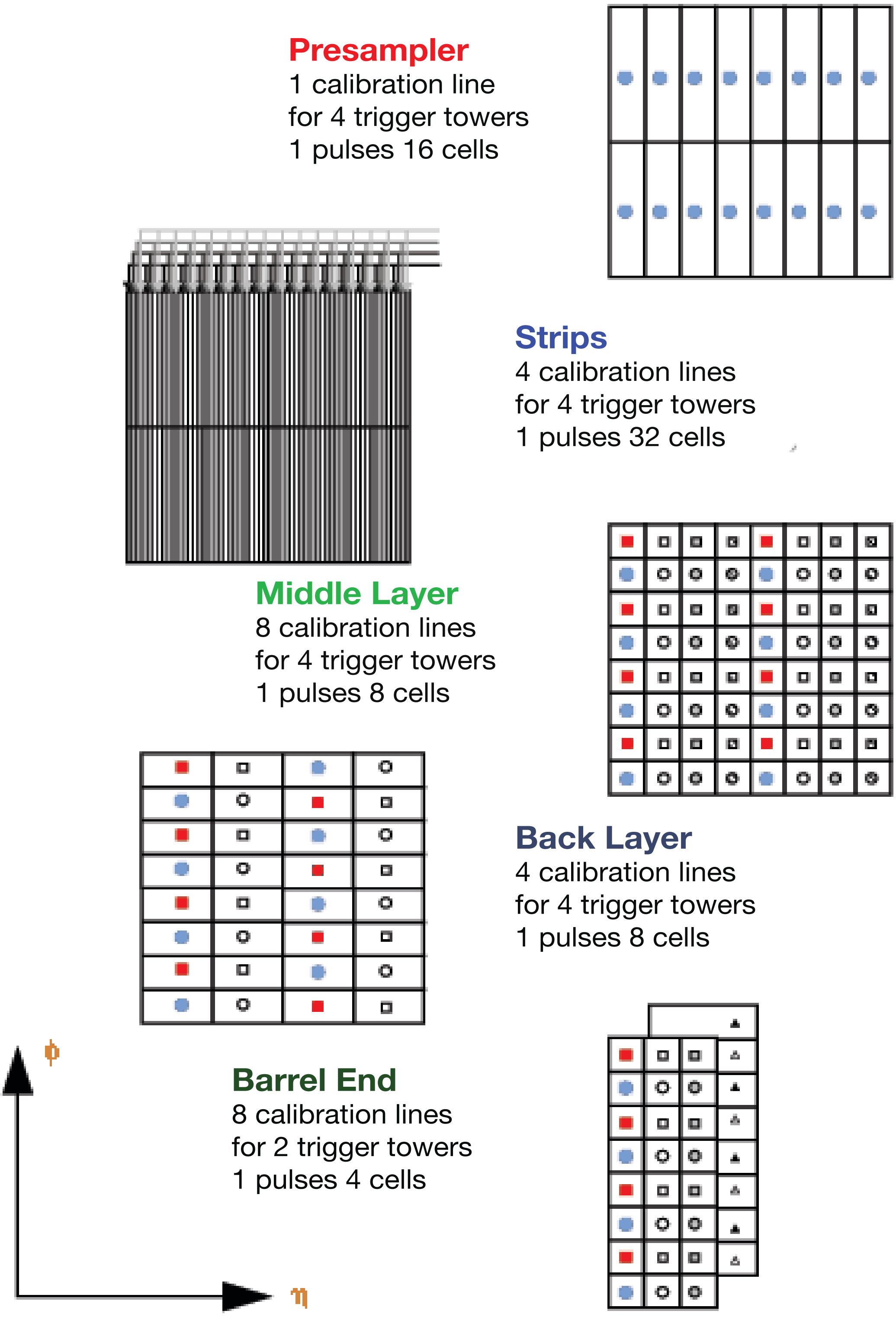

Figure 5.4 Symbolic representation of the calibration pattern in the EM barrel calorimeter. Within a given depth layer, calibration lines with common symbols are pulsed simultaneously.

The energy is computed as a linear sum of the (ADC-Pedestal) values in which the coefficients a_i and b_i are such that E is in *electron* linear scale and f is a factor that converts ADC counts for each gain to currents (μA) and from current to energy (MeV). a_i and b_i are the optimal filtering coefficients that can be derived from the shape of the physics pulse and the noise. The index *i* represents the number of samples taken to calculate the pulse. For ATLAS this number is 5. ADC_i is the value of the ADC cut in a particular sample. As a function of the detector modes, the DSPs (ROD processors) are initialized with different algorithms that allow for data taking in physics or calibration modes.

The decay time is determined by the pulser circuit. In order to obtain a 0.1% precision it is essential to form the pulse right on the electrodes, so that the path for calibration signals be as close as possible to the path for physics signals.

5.3.1 Pedestal

The pedestal of a read-out channel is the output signal when there is neither a beam nor a calibration pulse. The pedestal levels are calculated by computing the average output of each channel over all the pedestal events. Together with their standard deviation (which corresponds to the electronic noise) the pedestal levels are stored in a database for later use with calibration and physics data, where they are subtracted channel by channel as explained above.

5.4 The Current-to-Energy Conversion Factor

A charged particle which passes through the detector induces ionization in the liquid argon all along its track. The corresponding charges are collected by the anodes of the detector. After the amplification and the shaping, five samples of the signal are digitized by an ADC (Analog to Digital Converter). At this stage, the signal is measured in ADC-counts.

In order to get the measured current in units of visible energy a factor $f_{I/E}$, which is assumed to be independent of the beam energy is applied to each cell. Since the EM calorimeter contains two different geometries, the factors need to be calculated independently.

5.4.1 Accordion

Given that the accordion is a sampling calorimeter, the conversion factor μA2MeV_{acc} can be estimated in the following way:

$$\mu A2MeV_{acc} = \frac{1}{I/E \times f_{sampling}} \tag{5.3}$$

Where I/E is the energy to current conversion factor given by:

$$I/E = \frac{q_0}{W_0} f_{recomb}(E) V_d(E) \frac{E}{HV} \tag{5.4}$$

where:

- $q_0 = 1.6 \times 10^{-19} C$ is the electron charge.
- $W_0 = 23.6 eV$ is the ionization potential of the Liquid Argon.
- E is the electric field.
- $f_{recomb}(E)$ takes into account recombination effects (typically a few percent for $E = 10 kV.cm^{-1}$).
- $V_d(E)$ is the drift velocity.
- $HV = 2000V$ is the high voltage.

In the straight sections of the accordion calorimeter $E = HV/g$ where g is the gap width (2.12 mm). If we define $t_{drift} = g/V_d$ we can express I/E in the straight section as:

$$\begin{aligned} I/E_{straight} &= \frac{q_0}{W_0} f_{recomb}(E) \frac{V_d(E)}{g} \\ &= \frac{q_0}{W_0} f_{recomb}(E) t_{drift} \end{aligned} \tag{5.5}$$

In the accordion foldings, the electric field behaves differently (the charge collection is different) and the formula $E = HV/g$ no longer holds. To account for this difference, equation 5.4 needs to be integrated for charges deposited in the full LAr gap. The size of this effect is around 7%.

The values of I/E in the straight parts of the accordion from the simulation and the data are $14.2 nA/MeV$ and $16 nA/MeV$ respectively. Since the differences are not understood as of yet, the value obtained from the data will be used.

$f_{sampling}$ is the sampling fraction which translates the visible energy deposited in the liquid argon (E^{act}) into the total deposited energy (E^{tot}):

$$f_{sampling} = \frac{E^{act}}{E^{tot}} \tag{5.6}$$

It can be estimated knowing the energy deposited by ionization dE/dx (deposited by a MIP) and the additional energy e/μ deposited by radiation by an electron:

$$f_{sampling} = \frac{e}{\mu} \times \frac{dE/dx|_{act}}{dE/dx|_{act} + de/dx|_{pas}} \tag{5.7}$$

The additional effect of the electric field is taken into account by computing the visible energy from the simulated current I_{sim} using $I/E_{straight}$:

$$E^{act} = \frac{I_{sim}}{I/E_{straight}} \tag{5.8}$$

which lead to a value of $f_{sampling}$ 7% lower than with 5.7:

$$\begin{aligned} f_{sampling} &= 0.1667 \text{ for } \eta < 0.8 \\ &= 0.1959 \text{ for } \eta > 0.8 \end{aligned} \tag{5.9}$$

The dependence of the sampling fraction on the shower depth is taken into consideration at the cluster level.

5.4.2 Presampler

Given that the presampler is not a sampling calorimeter, the conversion from current to energy is done by replacing $f_{sampling}$ with a factor that is specific to the presampler: F_{PS}.

$$\mu A2MeV_{PS} = \frac{1}{I/E \times F_{PS}} \tag{5.10}$$

Since there is no bending in the presampler, the electric field suffers no deformations. The gap width however,varies according to η between 1.9 and 2.0 mm introducing an η dependence in *I/E* and a higher value for I/F_{PS} than I/E_{acc}. For simplicity, only one value of I/E is used for the whole presampler, averaging over the gap widths. Only 11 mm out of the 13 mm of the active layer of the presampler are exposed to the electric field. Therefore, the current Geant 4 simulation needs to be adjusted in order to take this fact into consideration. Future releases will cure this problem. The presampler conversion value can be deduced from the accordion by multiplying I/E_{acc} by the ratio of the gap width:

$$\begin{aligned} I/E_{PS} &= I/E_{acc} \times \frac{g_{acc}}{g_{PS}} \\ &= 16 \times \frac{2.12}{1.95} \\ &= 17.4 nA/MeV \end{aligned} \tag{5.11}$$

5.5 Optimal Filtering Technique

A digital filtering technique is used to extract the peak amplitude A and the signal time. This employs 5 signal samples (S_i) where A is expanded in a linear weighted sum of coefficients (OF) and the pedestal is subtracted from the signal in each sample (see equation 5.1).

This method ensures a non-biased way of cell energy reconstruction which minimizes noise contributions in particular during low luminosity periods. The coefficients are calculated using the expected shape of the pulse, its derivative and the noise autocorrelation function. The noise contribution is minimized respecting the constraints on the signal amplitude and its time jitter [1]. The noise autocorrelation function is determined from randomly triggered events.

The shape of the physics signal g_i ($g_i \equiv g(t_i)$) can be predicted using a formula with four free parameters, which can be extracted from a fit to the measured physics pulse shape [5] . The OF coefficients are then calculated in such a way that the variance of equations 3.1 and 3.2 is minimized satisfying a series of constraints [39]. The shapes of the measured and predicted physics pulses agree within 2 $\%$.

For a detailed calculation of the optimal filtering coefficients, see Appendix A.

---

[1] A shift on t_0 , τ or on the sampling frequency due to a jitter on the clock can cause an extra contribution to the constant term of the energy resolution, thus degrading the latter [46]

Chapter 6

The 2004 Combined Test Beam (CTB04)

As we approach the experiment start-up, the results obtained during the various test beam exercises increase in importance. The 2004 test beam has proven crucial to the experiment given that it is the first time where all sub-detectors were assembled in such a way to mimic a slice of the ATLAS detector. This study is based on photon runs obtained during CTB04 and will help to unveil the response of the ATLAS detector and, in particular, the Liquid Argon calorimeter. This chapter is aimed at describing the setup as well as the steps needed to have a successful photon run.

6.1 The H8 SPS Beam Line

The H8 beam line in the North Area of CERN (Figure 6.1) was designed to deliver secondary and tertiary beams of various particle types (hadrons, electrons, muons, ions), as well as an attenuated primary proton beam to a fixed target experiment (T4) located in the experimental hall area. In the case of our test beam, the secondary beam is produced by protons extracted from the SPS with momenta ranging from 10 GeV/c up to the maximum SPS momentum of 450 GeV/c. The protons impinge into the T4 target producing a shower of secondary particles. The creation of tertiary beams is handled by placing a second target located at about 130 m downstream of the T4 target.

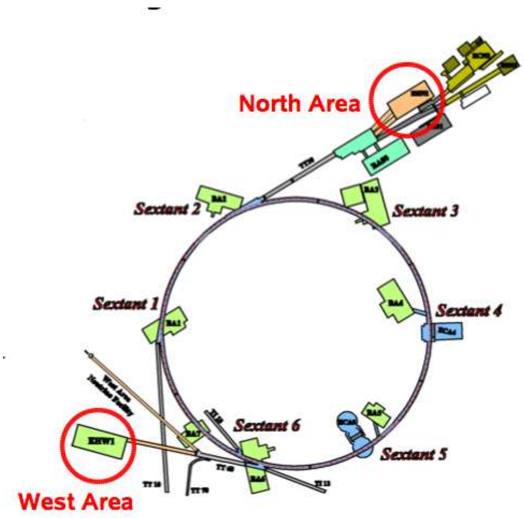

Figure 6.1 SPS H8 beam line

A large spectrometer constructed of six MBN dipole magnets is used for the momentum definition. In addition to the above mentioned beams, the H8 beam line offers the possibility of producing very low energy range particles (i.e. down to 1 GeV/c). This is achieved by redirecting a secondary beam from T4 towards a secondary target (T48) located at about 40m upstream of the experimental setup.

6.2 The CTB Reference System

The reference system is defined to be as consistent as possible with the ATLAS reference system. The (x, y, z) reference system is defined as follows:

- x-axis along the H8-beam;
- z-axis horizontally towards the South East ;
- y-axis vertically towards the sky;
- $x = y = z = 0$ on the axis of the H8-beam, at the front surface of the Inner Detector Magnet (MBPSID).

6.2.1 The Detectors

The entire volume of the test beam setup (see Figure 6.2.1) has been designed to include all sub-detectors in addition to the pre-existing beam line elements. The most challenging of these inclusions was that of the EM barrel calorimeter prototype module (M0). Due to the large size of the cryostat, an argon excluder (a block of Rohacell [1]) was installed in front of the module.

---

[1] Rohacell is a rigid-foam with very low density

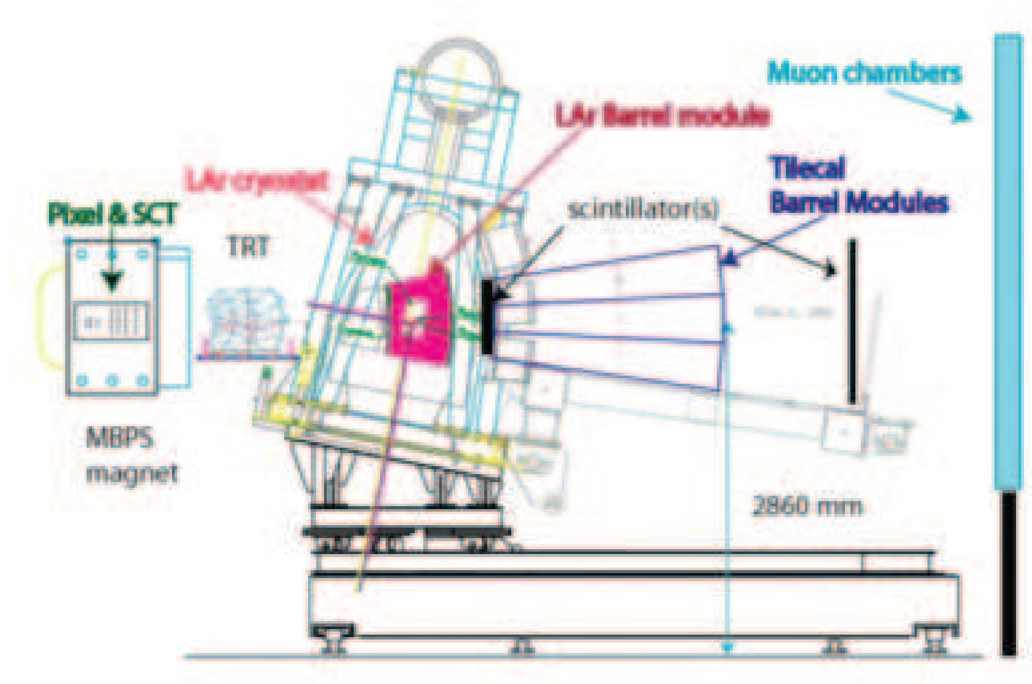

Figure 6.2 Schematic of the test beam table setup. The beam particles first hit the pixel and SCT modules and then continue towards the TRT, calorimeters and muon modules. In the coordinate system used, the beam travels in the positive x direction, y points upwards and z points out of the paper.

Behind the back wall of the cryostat, three tile calorimeter modules are stacked. The calorimeter modules (82 Tons) are placed perpendicular to the beam line and they rest on a rotating table. Said table rotates around the vertical axis and translates on the horizontal axis. These two motions allow for the simulation of different impact points in η. The table, however, cannot be rotated around the horizontal axis, therefore, to simulate different impact points in ϕ a deflecting magnetic field is needed.

Figure 6.3 shows the LAr-Tile calorimeters setup together with their reference systems.

Upstream of the cryostat, the MBPSID is placed. It generates the magnetic field for the inner detector elements. The SCT and Pixel modules are placed inside this magnet. The pixel detector is made of 6 modules and each module has a size of $z \times y = 60.8 \times 16.4mm^2$. The SCT detector consists of 4 layers with 2 modules per layer, each module covers an area $z \times y = 120 \times 60mm^2$.

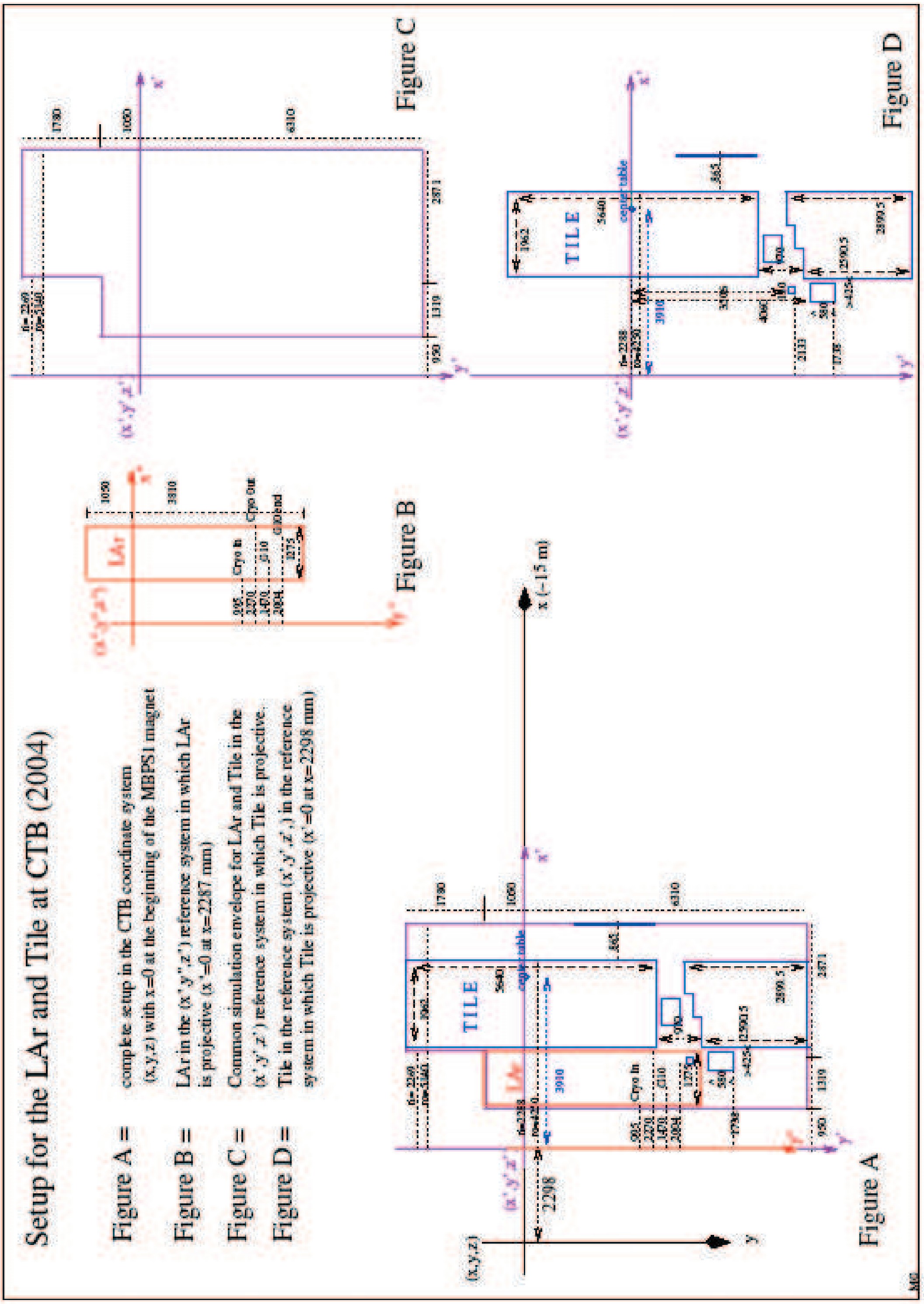

Figure 6.3 Liquid Argon and Tile setup

The TRT detector is made of two barrels and due to its size it is kept outside the MBPSID magnet. The distance in ATLAS between the last SCT layer and the first TRT plane is 40 mm, while in the Combined Test Beam layout is increased to ≈ 1114 mm, leaving a clearance for magnet coils and the TRT support structure.

On the back of the Tile Calorimeter modules there are racks and Muon Wall scintillators on the support table. Further downstream, a massive block of concrete (Beam Dump) has been placed to stop all particles except for muons. Several stations of muon chambers have been placed behind the beam dump.

6.3 Beam Instrumentation

Various beam instruments, aside from the detectors described above, were placed on the H8 beam line. The data obtained from these elements were recorded together with the event data to allow for offline data quality control. The layout of the beam instruments is shown in Figure 6.4.

The beam instruments are as follows:

- **Cherenkov counters** were used to distinguish pions and electrons at low energy.
- **Beam chambers** were used to verify the beam profile.
- **Scintillators** were installed in the beam line and some of them were used for trigger purposes.
  - *Muon Veto* was used to veto muons passing through the high energy beam stop during low energy runs.
  - *S1* was a big ($10 \times 10cm^2$) scintillator located after the first quadrapole magnet. Its amplitude and its signal were measured.
  - *Muon Halo* vetoed muons outside the beam axis.
  - *S2 and S3* were used for trigger purposes and were read out by photomultipliers.
  - *Cryostat Scintillators* were placed between the liquid argon cryostat and the Tile calorimeter.

- *Muon Wall* consisted of 12 scintillators located behind the tile calorimeter.
- *Muon Tag* was placed behind the beam dump in order to identify muons.

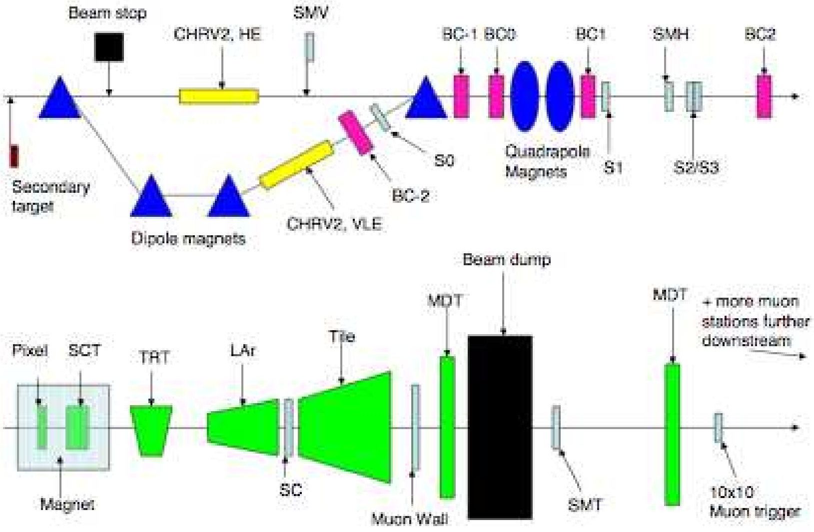

Figure 6.4 Schematic outline of the beam line instrumentation, and of the ATLAS sub-detector elements.

Chapter 7

Event Selection

The complexity of the initial conditions of photon run 2102966 made the event selection process an arduous one. The surviving events ready for analysis, after reconstruction and clean-up cuts, represented only 25$\%$ of the original sample. This chapter describes in detail the steps needed in order to set-up the photon beam for the run, as well as the process of event selection.

7.1 Photon Run Setup

Of the many different studies performed with the combined test beam, the photon study is the subject of this thesis. The photon beam was obtained by colliding electrons, momentum of 50 or 180GeV/c , with a 0.1 X_0 lead target, producing bremsstrahlung photons (Figure 7.1). Two magnets, downstream of the target, swept away electrons from the photon trajectory. The first magnet separated the electron from the photon in the η plane, while the second one deviated it in the ϕ plane. The separation changed with the different magnetic fields. Each magnet had a maximum bending power of 3.8 Tm. For photon runs where the inner detector was active, a $1X_0$ converter, followed by scintillators, was placed in the photon beam to detect photon conversions into e^+e^- pairs. Electrons were triggered by a scintillator (8x8 mm^2) .

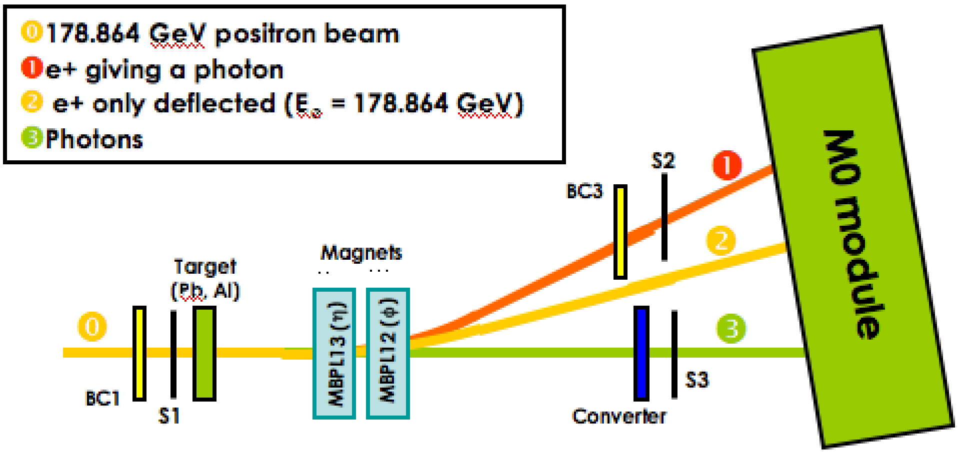

Figure 7.1 Schematic view (from the top) of the photon beam setup for runs with and without inner detector participation.

7.2 Data Readiness

The preparation for the photon run was no trivial task, for there were two main questions that needed to be answered prior to the actual run:

- How to obtain as pure as possible a photon beam without having too many photons convert in the first target?
- What are the ideal magnetic fields for the positron bending that will not clip it or place it outside the calorimeter?

The first question relates to the thickness of the target, and it was answered by running a Geant4 simulation of 100000 electrons impinging on different target thicknesses and counting the number of single, double and triple photons coming out of the back of the plate. Four different target thicknesses were used (see Table 7.1) and it was concluded that a thickness of 0.6mm provided a good compromise between the number of clean photons and the contamination arising from multiple bremsstrahlung and photon conversions. As far as the conversions

Table 7.1 Target Thickness Results

Target Width	**Single γ**	**Double γ**	**Triple γ**
0.2 mm	152	18	2
0.6 mm	283	119	22
1.0 mm	345	235	62
1.2 mm	354	261	71

are concerned, the probability for a photon to convert is given by

$$\begin{gathered} P_C = 1 - P_{NC}, \text{ where} \\ P_{NC} = \frac{N}{N_0} = e^{-\frac{\Delta x[X0]}{9X0/7}} \text{ and} \end{gathered} \tag{7.1}$$

Δx is the amount of material expressed in X_0 s that the photon will traverse before converting. In our case the material used was Pb and its X_0 was 0.56 cm . A target of $0.1X_0$ was chosen, giving $\approx 8\%$ of photon conversions.

The second question was twofold, for unlike in previous test beams, this time there were two magnets to tune so that the positron and the photon would hit the calorimeter at two distinctive and well separated locations.

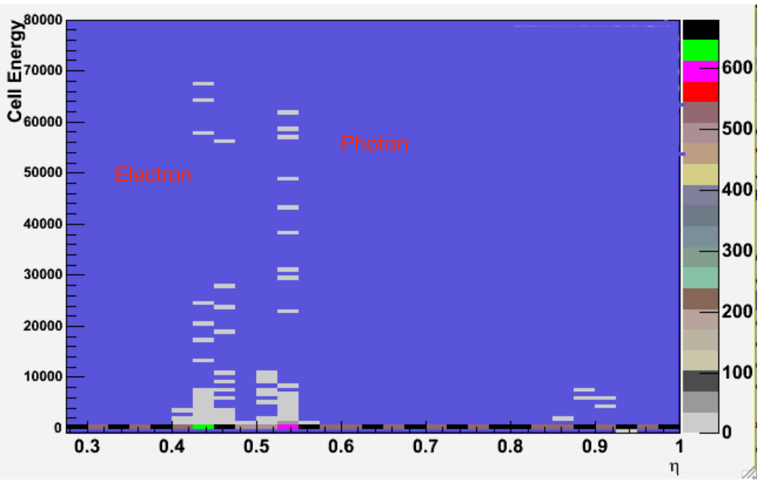

Figure 7.2 Photon/Electron separation at the cell level in sampling 2.

The most important tuning was done with the first magnet because at least three-cell-separation in sampling 2 was needed between the impact points in order to reconstruct the clusters properly. This preliminary study yielded a separation of 5 second-sampling cells in η using a magnetic field of 3.0 Tm on electrons of 180GeV/c in momentum. The cell distribution showing the separation between the particles can be seen in Figure 7.2. For the specific run here analyzed the magnetic fields expressed in Tesla meters were $B_y = 1.25$ Tm and $B_z = 1.4$ Tm.

7.3 Data Reconstruction

The data were reconstructed using the ATLAS official offline software (Athena) version 10.5.0, adapted for the test beam. The optimal filtering coefficient method (see Appendix A) was applied to obtain the reconstructed energy on a 3×3 cluster scheme. The initial number of events was ≈100,000. After the clean-up cuts, only 25% of the events survived.

7.4 Data Clean-up Procedure

The clean-up cuts were run dependent. For this study run number 2102966, corresponding to Period 8 [1] was used. This run included only the TRT and the LAr sub-detectors. The most important criterion for choosing a run was that it complied with the right separation between the photon-positron pair. The topology of most events from this run can be seen in Figure 7.3(a). A typical event with the required separation is shown in Figure 7.3(b). The number of cells in each cluster after the reconstruction is shown in Table 7.2.

The run, without cuts applied, contained photon-positron pairs and single positrons as well as muon contamination. The second lower energy peak in Figure 7.4(a) is representative of the single positrons, while the peak at very low energies shows the beam halo muons. Figures 7.4(a) and 7.4(b) show the distributions before and after cuts.

---

[1] During the combined test beam there were 8 different run periods corresponding to different beam configurations.

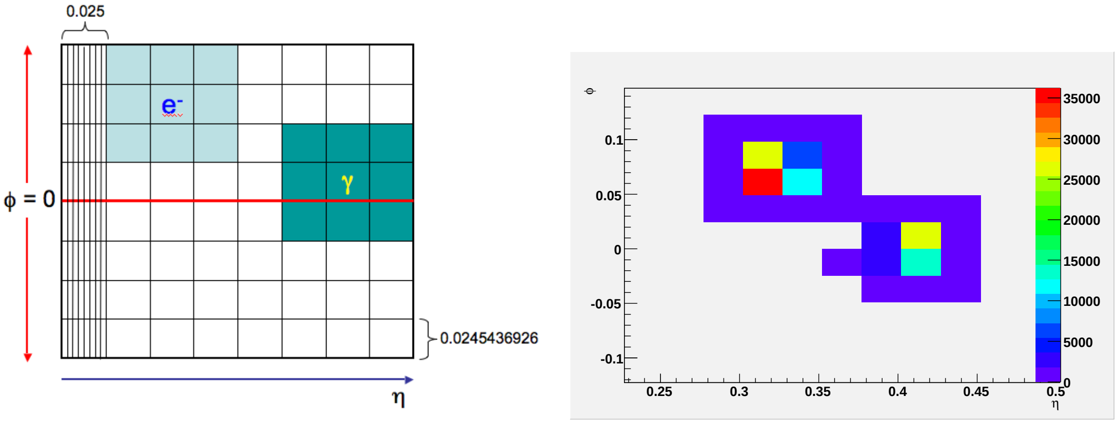

(a) Topology of an expected event.

(b) Topology of event number 88. Photon run number 2102966.

Figure 7.3 Topology of an event on the second sampling of the calorimeter.

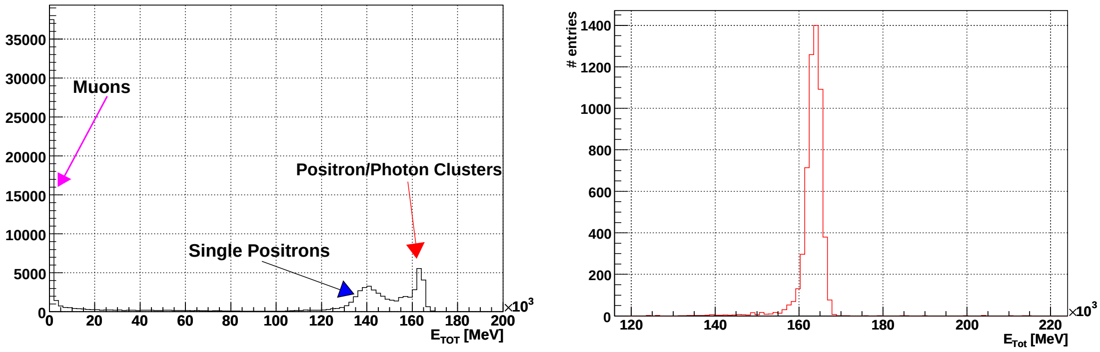

(a) Total Energy Distribution (before cuts)

(b) Total Energy Distribution (after cuts)

Figure 7.4 Total Energy Distribution in the EM calorimeter.

In order to be considered a good event, said event had to satisfy the following criteria:

- **Energy Seeds:** Two high energy seeds had to be present, one for the positron and one for the photon. Each seed was to have a minimum energy of 30 GeV and 10 GeV for positron and photon respectively. This seed cut made sure that only events with two clusters were present.

- **Muon Contamination:** Two cuts, identified by beam cleaning studies, were applied to remove contamination by muons (see Figures 7.5(a) and 7.5(b)). They were based on the number of scintillator ADC counts. There were two scintillators, one tagging the muons and the other one catching the halo muons. The cuts applied on the tagging scintillator required that the analyzed clusters had more than 470 ADC counts, while the halo tagger required for the good clusters ADC counts between 800 and 4000. The number of events attributable to muon contamination for this analysis is 3%.

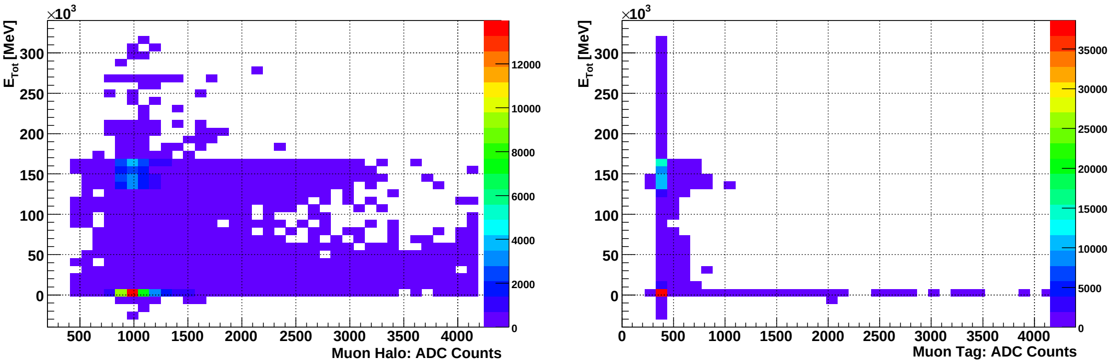

(a) Muon Halo (b) Muon Tag

Figure 7.5 Muon Halo and Tag ADC counters.

- **Lower Energy Tails:** Two are the identified causes of the low energy tails
  - Given that the photon impact point (seed) on the cell is not always at $\phi > 0$ the number of strips that is reconstructed varies from 24 to 48 causing higher noise to be absorbed by the photon cluster. A constraint on the number of strips is applied and the noise contribution is considerably reduced.
  - There is a total energy dependence on the η position in the calorimeter linked to the amount of material a particle traverses. In order to deal with this effect, a cut was applied on the η position of the photon strips to remove this tail (see Figure 7.6). This effect is common to all test beam runs.

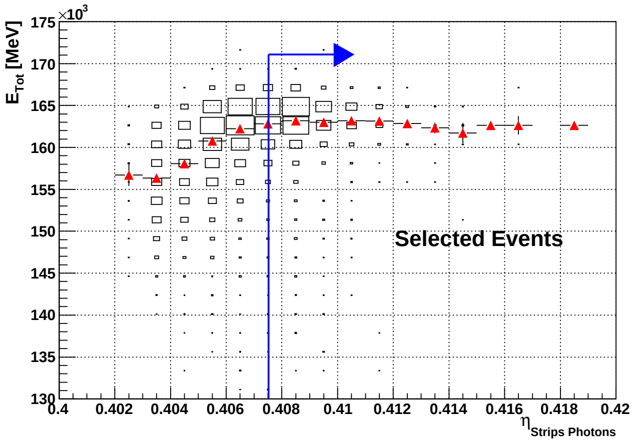

Figure 7.6 Total energy as a function of the position in the strips. Only points with $\eta > 0.4075$ are kept.

Table 7.2 Number of Cells in Clusters per Calorimeter Sampling.

Sampling	**Cluster γ**	**Cluster e^+**
Presampler	6	6
First Sampling	9	9 or 18
Second Sampling	9	9
Third Sampling	6	6

7.5 Noise Treatment

As stated in Chapter 4, one of the biggest contributors to the deterioration of the total energy resolution in the ATLAS LAr calorimeter is the electronic noise level. One of the benefits derived from our test beam analysis was the fact that we were able to obtain a value fot the noise contribution per cell, mostly in high gain mode, by fitting the energy distribution of each cell to a Gaussian, obtaining the rms noise for each cell of our 3 x 3 cluster size. The fits were performed for electrons, then for electrons and photons. The results are shown in Figures 7.7 and 7.8 respectively.

The total noise contribution, σ_{Noise} was then calculated based on the number of cells contained in each cluster as seen on Table 7.3. The contribution can then be expressed as:

$$\sigma^2_{Noise} = \sigma_{NoisePS} \oplus \sigma_{Noise1S} \oplus \sigma_{Noise2S} \oplus \sigma_{Noise3S} \tag{7.2}$$

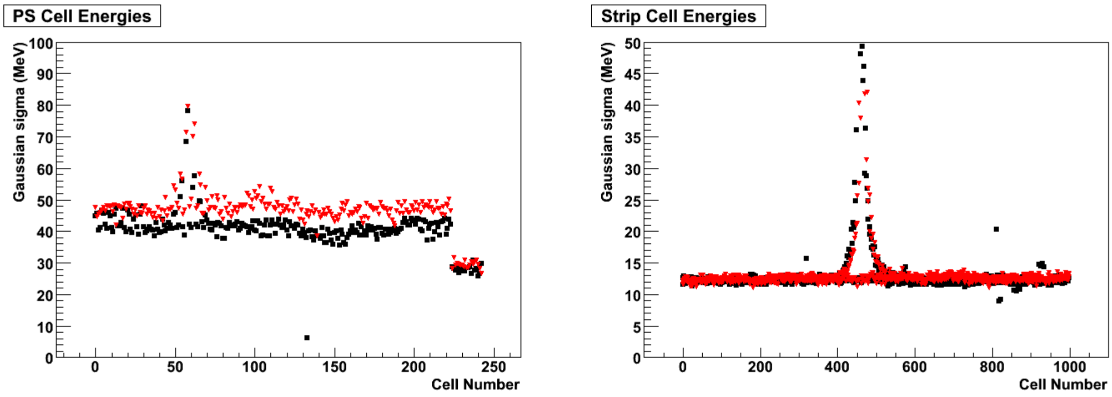

(a) Presampler Cell Energy: σ_{Noise} (b) First Sampling Cell Energy: σ_{Noise}

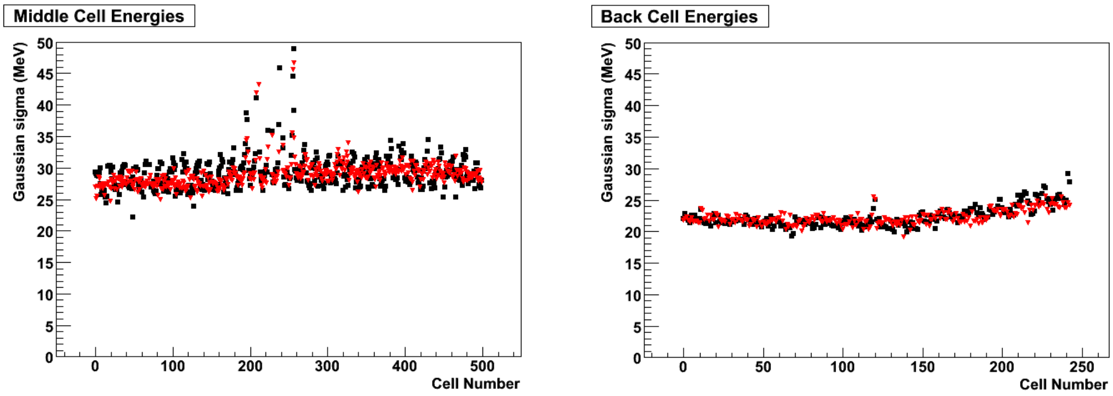

(c) Second Sampling Cell Energy: σ_{Noise} (d) Third Sampling Cell Energy: σ_{Noise}

Figure 7.7 σ_{Noise} at the cell energy level for the presampler and the 3 layers of the EM calorimeter computed with OFC reconstruction for electron run 1000952. Monte Carlo distributions are in red, data in black. (High Gain)

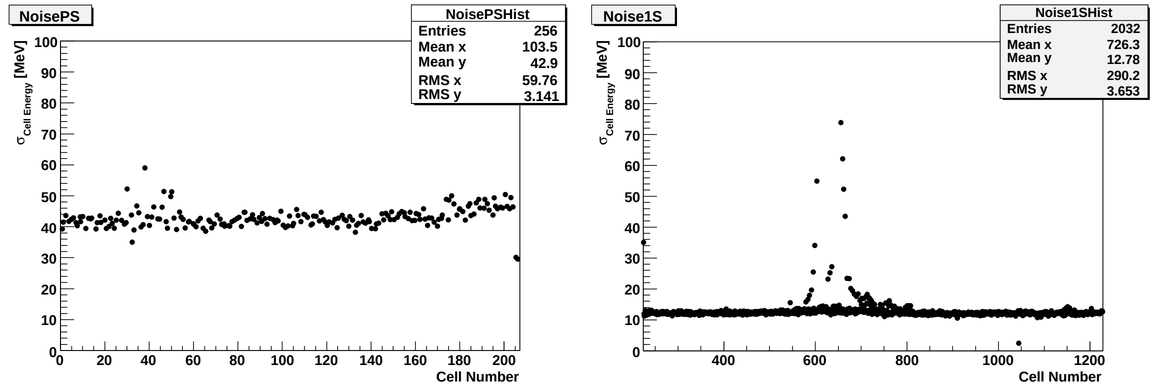

(a) Presampler Cell Energy: σ_{Noise}

(b) First Sampling Cell Energy: σ_{Noise}

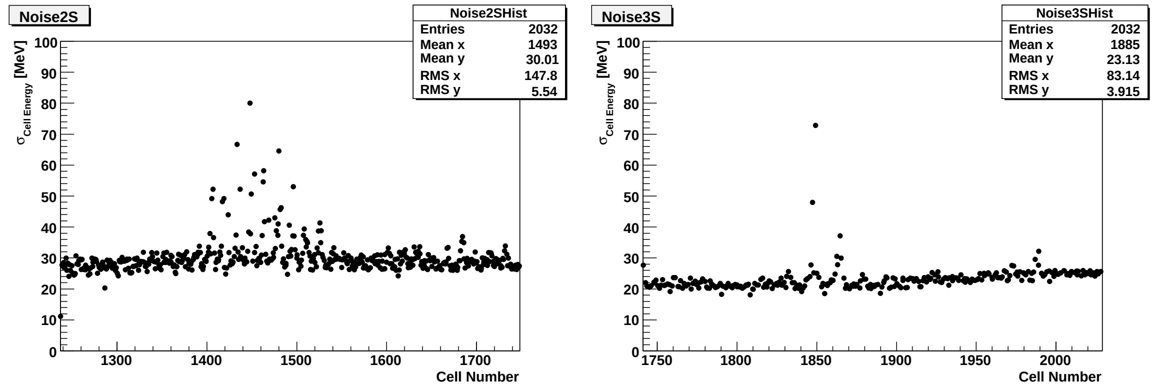

(c) Second Sampling Cell Energy: σ_{Noise}

(d) Third Sampling Cell Energy: σ_{Noise}

Figure 7.8 σ_{Noise} at the cell energy level for the presampler and the 3 layers of the EM calorimeter computed with OFC reconstruction for photon run 2102966. The computation is based on the high gain mode.

Table 7.3 σ_{Noise} contribution per calorimeter sampling for 100 GeV electrons (1 cluster) and for electrons and photons with total energy $\sim$ 163 GeV (2 clusters).

	Electrons in [MeV]		**Electrons and Photons in [MeV]**	
Sampling	$\sigma_{NoisePerCell}$	$\sigma_{NoisePerSampling}$	$\sigma_{NoisePerCell}$	$\sigma_{NoisePerSampling}$
Presampler	40	97.9	42.84	148.40
First Sampling	12	83.14	12.78	76.68
Second Sampling	27	81.0	30.01	127.32
Third Sampling	22	53.8	23.14	80.159

The noise contributions were found to be ~ 165 MeV for one 3 x 3 electron cluster and ~ 224 MeV for two 3 x 3 positron and photon clusters, based on high gain.

7.6 Local Constant Term

This term was obtained with electrons of 20, 50, 80, 100 and 180 GeV energies hitting the calorimeter at η = 0.45 and ϕ = 0.

These electrons were reconstructed with the optimal filtering coefficient method and with corrections for the ϕ-modulation. Figure 7.6 shows a local constant term of 0.26 $\%$. The local constant term was obtained by fitting the curve σ/E with the function $c^2 + a^2/E$. The value of the parameter c that adjusted the fitting function to the curve gave the value of the local constant term. The value of the local constant term accounts for local non-uniformities and it is in agreement with previous benchmark studies [13].

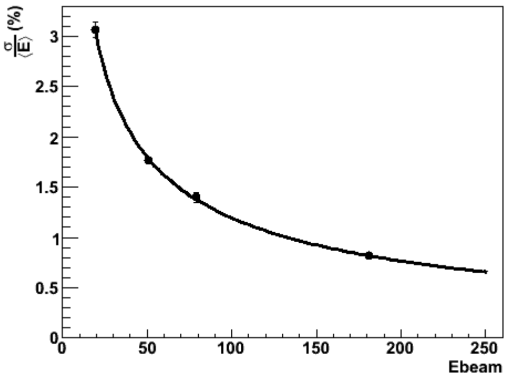

Figure 7.9 Local constant term extracted from test beam electrons.

7.7 Beam Energy Determination for Photon Run 2102966

In order to conduct this study, a precise determination of the beam energy was needed [35]. The H8 beam line around the bending magnets region is shown in Figure 7.7 . The beam energy was obtained from the bending power of the magnets.

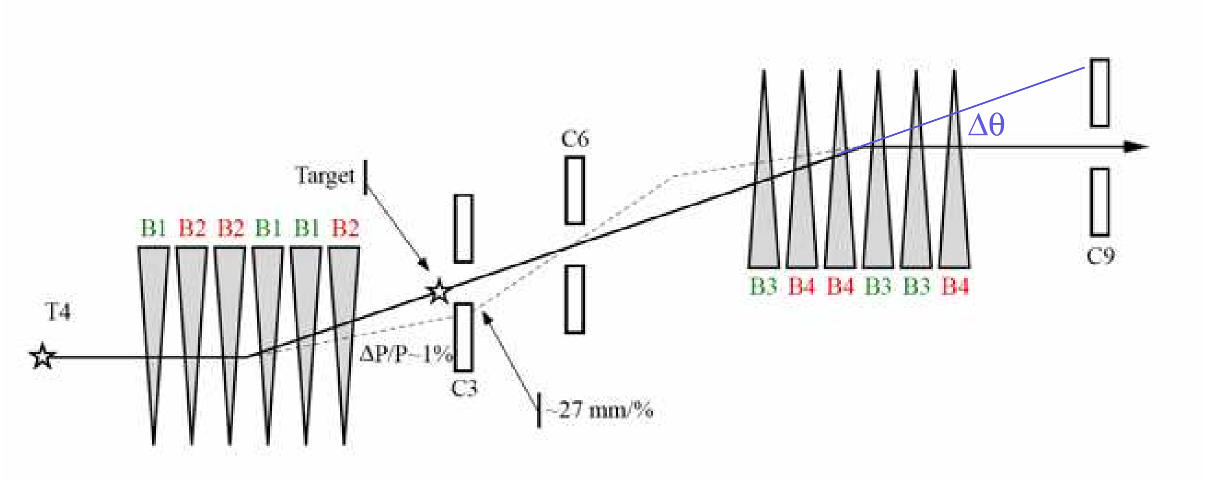

Figure 7.10 H8 beam line. Detailed description of magnets and collimators.

This particular calculation included the following:

- Currents set and measured in magnets B3 and B4
- Positions of the beam collimators C3 and C9
- Energy and the error on the absolute energy
- Energy spread-in percentage due to the opening of the collimators
- Error due to the uncertainty of the currents in the magnets of 0.2 A
- Effects of synchrotron radiation (0.814±0.004 GeV)

The final beam energy obtained for this run was **178.864 ± 0.936 GeV**.

Chapter 8

Monte Carlo Simulation of the Test Beam Setup

One of the most challenging aspects of this analysis proved to be the Monte Carlo simulation of the photon run. Not only for the 8.5 % reduction in the total energy due to the reconstruction with OFCs and other effects, but also for the difficulties arising from the tuning of the different elements of the beam line (i.e. magnets). This chapter describes the necessary steps for the production of the Monte Carlo using the ATHENA framework as it pertains to this run, as well as the needed corrections applied to the Monte Carlo in order to obtain as close as possible a description of the data.

8.1 Monte Carlo Production

8.1.1 Simulation

The ATLAS software possesses a package called the *Particle Generator* [41] [29]. This generator receives input from the user regarding the type of particle to be generated, its energy, the calorimeter coordinates, the beam spot as well as the starting point of the beam. The particles, are then sent to Geant4 for complete detector simulation. Geant4 was chosen because it describes the electromagnetic interactions with good accuracy. It is incorporated into the ATLAS software framework and it is configurable via python-based scripts, known as jobOptions files.

This method works well with single particles; however, the photon run contains two particles (positron and photon), rendering the generation more complex.

On the other hand, the distributions of either of the particles were not monochromatic and as far as the photon was concerned, its own energy distribution had non-Gaussian tails. This posed a problem with respect to the energies to be given to the generator. After careful consideration, it was decided that a spectrum would be fed into the generator (for the photon) and that its positron partner would acquire its energy by subtracting the photon energy to that of the beam.

After the data cleanup cuts, a photon spectrum (see Figure 8.1) was obtained, but as mentioned before its distribution was shifted by $\sim 8.5\ \%$, given that the data reconstruction used OFCs. Since we did not want to alter the original beam energy, the spectrum was scaled up by said amount.

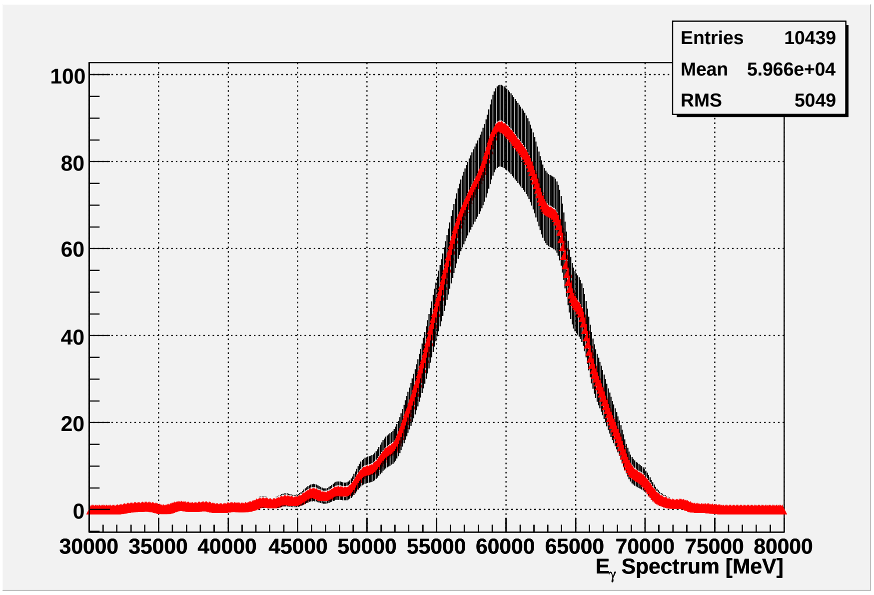

Figure 8.1 Photon spectrum derived from run 2102966 after cleanup cuts. The spectrum serves as input to the MC generation.

Up to this moment, the Monte Carlo used a constant electric field in the liquid argon electrodes. The magnetic fields of the bending magnets (see Chapter 7) had to be tuned so that the MC would match the impact point on the cells for both photon and positron.

8.1.2 Digitization and Reconstruction

The same method used for data reconstruction applied to the Monte Carlo. The greatest difference was that the output of the simulation had to be digitized before it could be reconstructed. Digitization is a process whereby the output of the detector simulation called *hits* are converted to a raw-data format. This stage introduces effects of the readout chain such as electronic noise and cross-talk. This is generally done by applying corrections factors and not by a detailed simulation of the detector readout. The file obtained during the digitization can then be processed by the reconstruction software.

The MC reconstruction shared the same characteristics with the data reconstruction described in Chapter 7.

8.2 Monte Carlo/Data Comparison and MC tuning

One sample of Monte Carlo for this specific photon run was simulated. It contained no extra material in front of the calorimeter (first cryostat wall). To account for the differences in normalization between the Monte Carlo and the data, four adjustable correction factors were allowed on the Monte Carlo to match the data. One factor was applied to the presampler, while the other three were applied to the photon, electron and total reconstructed energies.

The presampler energy was rescaled due to the fact that the argon-filled gas was 13mm wide, but the electric field was only simulated to cover 11mm. In the simulation, the full gap was regarded as an active region, therefore the presampler had to be weighted by a factor 11/13.

At the data level, we had the presence of the cross-talk, which is responsible for changing the scale of the energy measurement in the strips compartment. The electronic calibration signal was lowered due to signal loss toward the neighboring cells, thus the overestimation of the physics signal. Since this effect was not simulated, the energy in the strips (data) was reduced by $\sim 7\ \%$.

Due to mismatches in the η coordinate for both photons and positrons, it was necessary to adjust the value of their individual energy depositions. The positron deviated by about 5%, so the best mach to the data was achieved by scaling down its energy (MC) by a factor of 0.9493. For the photon, the mismatch was not as large (impact point off by one strip cell) so its energy (MC) was scaled by a factor 0.973. To match the sum of the distributions a small factor (1.003) was applied to the total Monte Carlo energy. Figures 8.2(a)), 8.4(c) and 8.4(b) display the distributions with the factors applied.

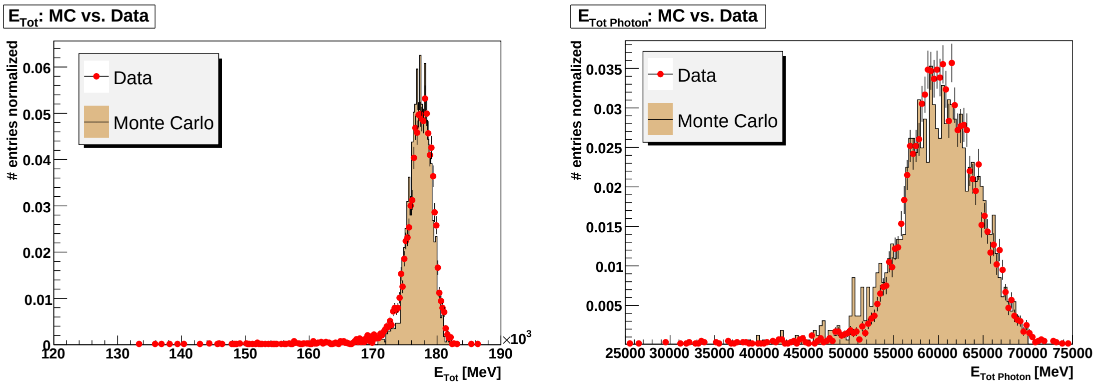

(a) Total Accordion Energy

(b) Total Photon Accordion Energy

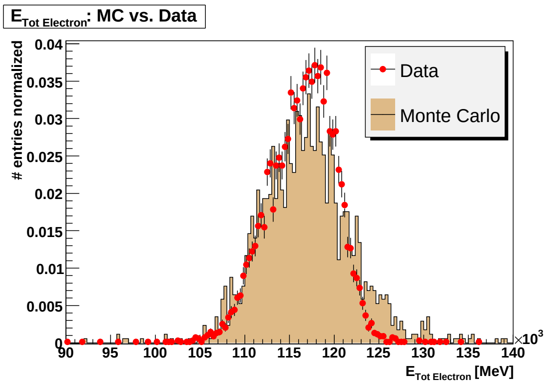

(c) Total Positron Accordion Energy

Figure 8.2 Total accordion energy deposit for the sum of the particles energies and for the particles separately.

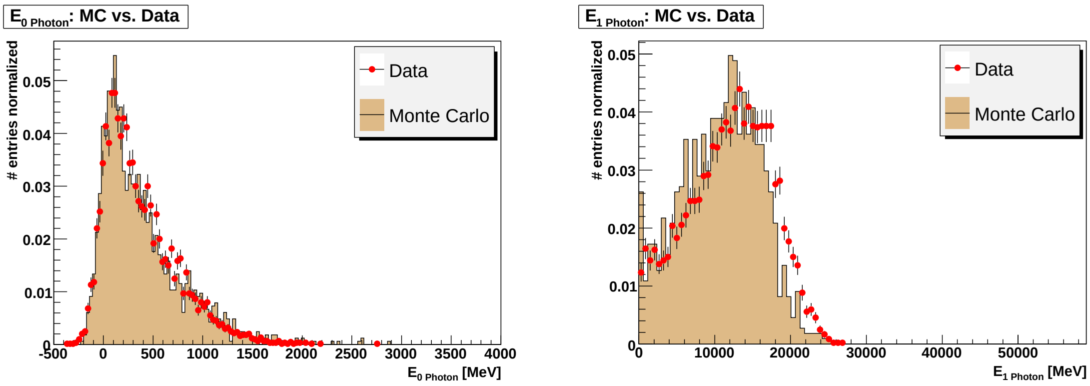

(a) Presampler (b) First Sampling

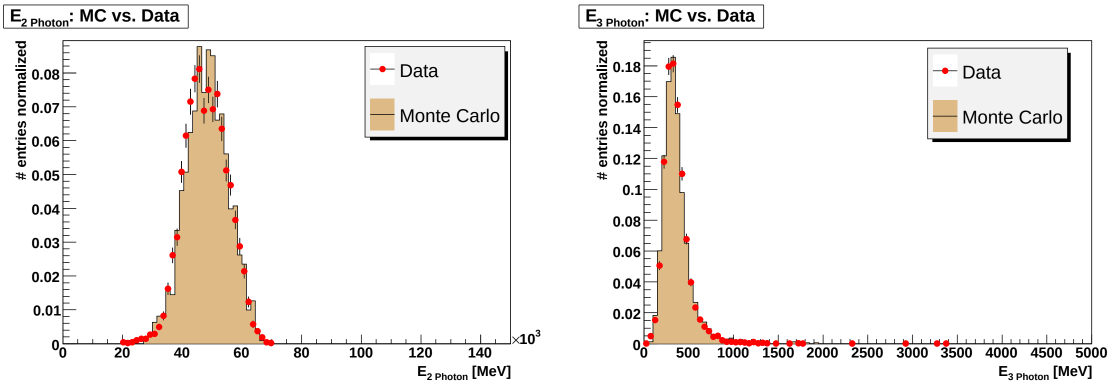

(c) Second Sampling (d) Third Sampling

Figure 8.3 Total energy deposit in each compartment of the calorimeter for data and simulation for 60 GeV photons.

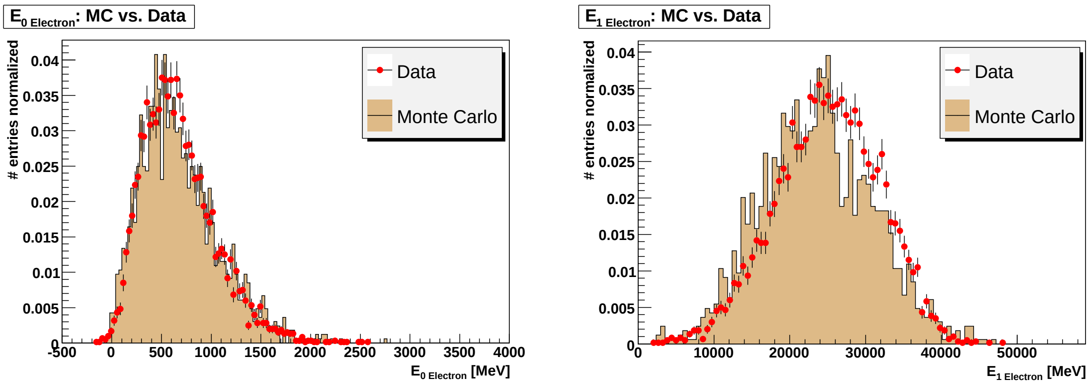

(a) Presampler (b) First Sampling

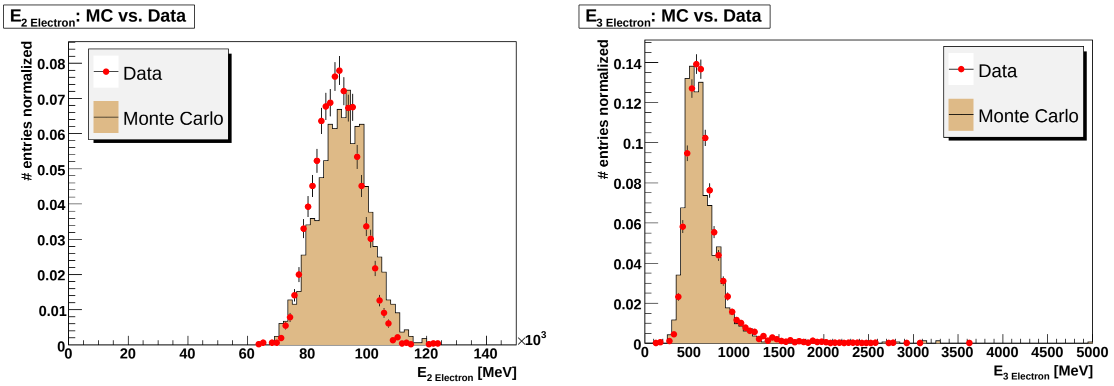

(c) Second Sampling (d) Third Sampling

Figure 8.4 Total energy deposit in each compartment of the calorimeter for data and simulation for 120 GeV positrons.

The slightly wider distributions seen in the first and second samplings of the Monte Carlo (positrons) could be attributed to the absence of the positron trigger scintillator in the simulation. By taking the ratio between the fitted means of samplings 1 and 2 for the photons and positrons respectively, we see that the energy shift is consistent for both samples. The effects are still under investigation and there are four possible causes for the shifts:

- There exists the possibility of extra material placed upstream of the calorimeter during data taking, but not present during the simulation.
- There could be extra material between the presampler and the strips.
- Extra losses in the middle compartment could be due to wider showers in real data.
- The strips (data) may have more cross-talk than the estimated.

Chapter 9

Calibration Hits Studies

When performing Monte Carlo studies, it is possible to save and identify the energy deposits in all of the materials of the ATLAS detector, as well as the leakage energy information. This functionality allows for the better understanding of the data being analyzed, given that with the real data these options do not exists. The energy depositions are recorded in objects called calibration hits. This study takes full advantage of these simulated objects in order to better understand the behavior of photons and electrons in the combined test beam 2004 using the photon run setup.

9.1 Calibration Hits Defined

Calibration hits are a means of obtaining the true visible energy deposited in each compartment of the calorimeter. This way of measuring the energy avoids biases introduced by the reconstruction algorithms. They are used in special simulation runs for:

- Calibration of the ATLAS sub-detectors;
- Understanding of the full energy balance of specific event types such as the evaluation of missing visible energy which can be caused by energy deposits in dead materials and by leakage;
- Identification of full energy associated with each jet and multi-jet events.

There is a common design for the energy deposit treatment in both the liquid argon and the tile calorimeters. The calibration hits allow us to define regions of active, passive and dead material (i.e. cryostat walls, coil, support, cables, etc) in both calorimeters as well as in the entire detector. All materials in the inner detector are considered dead.

9.2 Beginning of the Calibration Exercise

Since one of the aims of this study was geared to establish the similarities and/or differences between photons and electrons at the calorimeter level by applying the corrections for electrons on photons, it was necessary to produce hits for electrons and photons. The energies generated were approximated to those from the photon run under study (i.e. electrons of momenta of 60 and 120 GeV/c and photons of momentum 60GeV/c). The goal of the calibration hits exercise was to find out the percentage level difference between the energy of electrons and photons defined by $R = \frac{E_\gamma}{E_{e^-}}$. It considered the extra effects available at the calibration hits level including corrections for upstream material, out of cone energy and energy leakage, otherwise biased and not distinguishable during the reconstruction process. These effects were calculated based on a 3 × 3 cluster size for both electrons and photons. The corrections derived from the calibration hits were later applied to the photon test beam data. The following expression was used to obtain the energies for photons and electrons:

$$E_{Particle} = \mathit{Offset} + W_0 \times E_0^{Vis} + \frac{1}{f_{sampling}} \times E_{Accordion}^{Vis} + E_{OutOfCone} + E_{BackLeakage} \tag{9.1}$$

and R was found to be:

$$\begin{aligned} R &= \frac{E_\gamma}{E_{e^-}} \\ R &= \frac{60.39 \pm 0.03 \mathit{GeV}}{59.78 \pm 0.01 \mathit{GeV}} \\ R &= 1.0102 \pm 0.0006 \end{aligned} \tag{9.2}$$

The greatest challenge in this exercise was imposed by the following conditions, which needed to be satisfied in order to apply the corrections to the data:

- The sampling fractions for electrons and photons in the LAr calorimeter should be within a small percentage difference;
- The ratio of the presampler weights between electrons and converted photons should be ~ 1.

- The offset for non-converted photons should be negligible.

The following subsections explore these conditions and describe the out-of-cone and leakage calculations.

9.2.1 Sampling Fractions

The sampling fraction for electrons and photons is calculated using the following formula:

$$f_{sampling}^{particle} = \frac{E^{Act}}{E^{Act} + E^{Pas}} \tag{9.3}$$

where E^{Pas} is the energy deposited in the passive (inactive) material. The sampling fractions are independent of the amount of material in front of the calorimeter. Figure 9.1 depicts the sampling fraction distributions for 60 GeV photons and electrons as well as for 120 GeV electrons for 3×3 cluster sizes.

9.2.2 Offset and Presampler Weight

These two factors correct for energy losses upstream of the presampler. They constitute the longitudinal weight corrections mentioned in Chapter 4. The offset (in units of energy) was motivated by the 2002 test beam analyses of electrons and it was found to simultaneously optimize electron energy linearity and resolution [28]. In the case of electrons, it represents the average energy lost by ionization by the beam electron. For photons the presampler weight takes into account that the $e^{+}e^{-}$ pairs produced in the passive material or in the active medium have only traversed part or none of the material in front of the presampler. These factors can only be extracted from a Monte Carlo simulation because they depend on the specifics of the experimental setup. The definition for the presampler weight is as follows:

$$W_0 = \frac{E_{Loss}^{UpstreamPS} + E_{Loss}^{BetweenPSandS1} + E_{PS}^{Active} + E_{PS}^{Passive}}{E_{PS}^{Active}} \tag{9.4}$$

For this study, both the offset and the presampler weight were obtained with Monte Carlo simulations by performing a linear fit of the energy loss [1] upstream of the first sampling of the

---

[1] Depending on their initial energy, particles may loose energy due to different effects. High energy electrons and positrons will lose energy due to bremsstrahlung (photon radiation) as a result of the Coulomb interaction

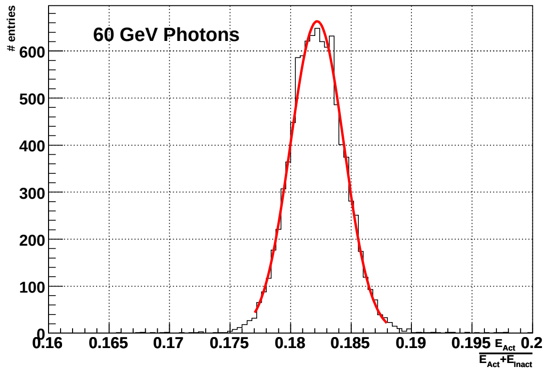

(a) 60 GeV Photons

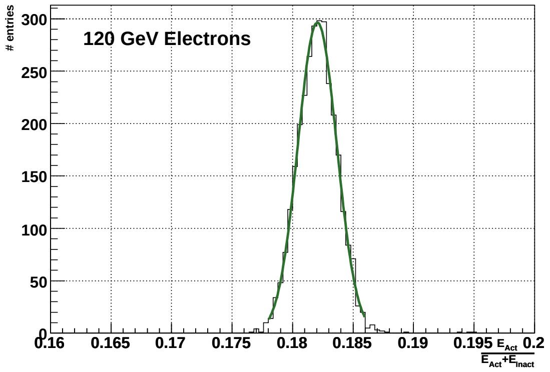

(b) 120 GeV Electrons

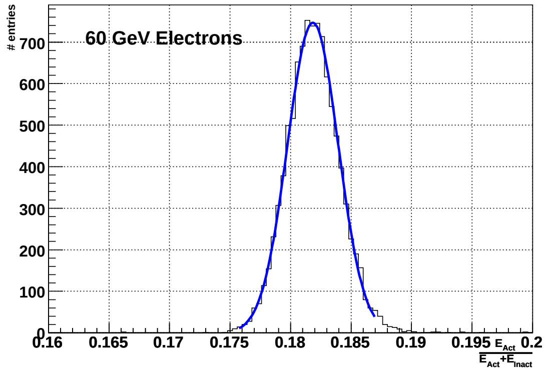

(c) 60 GeV Electrons

Figure 9.1 Sampling Fractions for electrons and photons obtained with calibration hits.

calorimeter versus the energy deposited in the active region of the presampler. Figures 9.2(a) , 9.2(b) and 9.2(c) show the linear fits on 60 GeV electrons and photons and on 120 GeV electrons.

Table 9.1 expresses the values of the presampler weight and offset for photons and electrons at different energies.

Table 9.1 Offset and presampler values for electrons and photons.

Calibration Hits		
Particle	Offset [GeV]	W0
Photon 60 GeV	114.65± 4.15	19.68 ± 0.17
Electron 60 GeV	318.1 ± 5.8	17.27 ± 0.4
Electron 120 GeV	358.5 ± 11.3	17.83 ± 0.25

As in the fit results, the presampler weight (slope) ratio between electrons and photons approaches unity. The same behavior can also be observed when examining the offsets (line intercept).

$$\begin{aligned}\frac{W0_\gamma}{W0_{electron}} &= \frac{19.68 \pm 0.17}{17.27 \pm 0.4} \\ &= 1.13 \pm 0.02\end{aligned} \tag{9.5}$$

Due to the non linearity of the photons as seen in Figure 9.2(b), it was necessary to begin the fit from a value of $E_{PSActive} > 5MeV$. The pronounced split could be used in the future as a discriminant between photons behaving in an electron-like fashion vis-à-vis other photons (i.e. non-converted). Photons with $E_{PS} <$ 100 MeV have an offset of 0.028 GeV and a presampler weight of 20.9. A more detailed examination of the energy losses upstream allowed us to see where the photons acquired the non linear behaviour. This occurred between the presampler and the first sampling of the calorimeter, as can be seen in Figure 9.3(b).

---

with the electric field generated by the atomic nuclei of the element they traverse. Photons, on the other hand, are affected by four different processes: the photoelectric effect, coherent (Rayleigh) scattering, incoherent (Compton) scattering and electron-positron pair production.

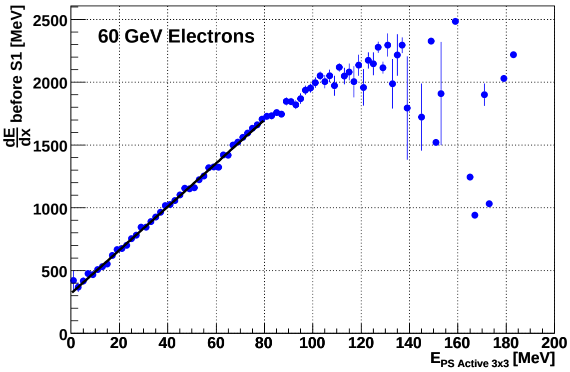

(a) 60 GeV Electrons

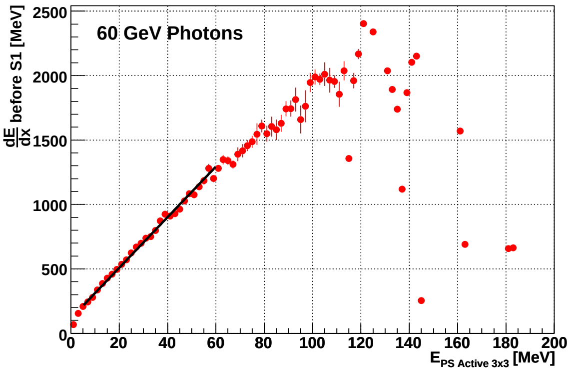

(b) 60 GeV Photons

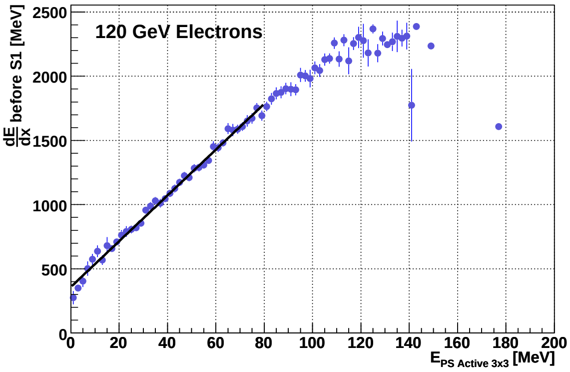

(c) 120 GeV Electrons

Figure 9.2 Energy loss upstream of the first sampling as a function of the energy deposited in the active layer of the presampler

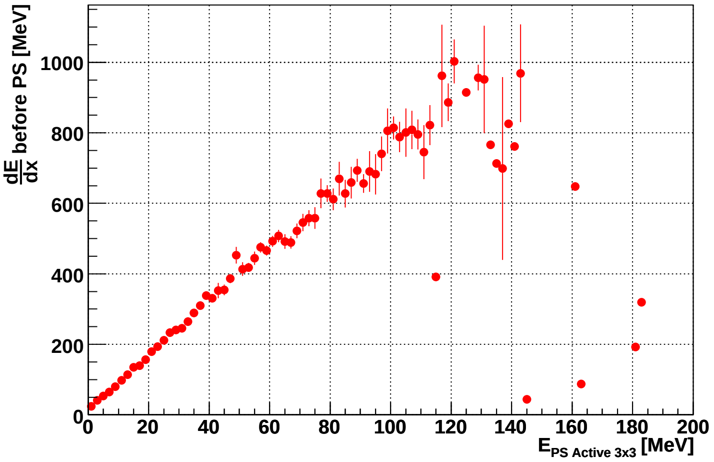

(a) Energy loss before presampler

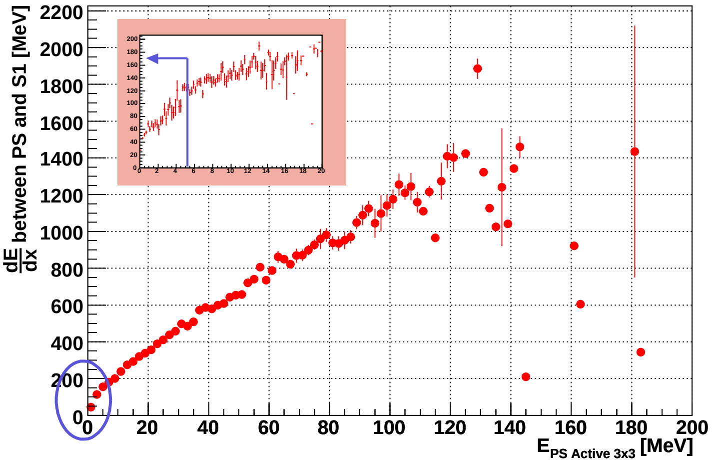

(b) Energy loss between the presampler and the first sampling

Figure 9.3 Energy loss for photons upstream of the presampler (a) and between the presampler and the first calorimeter layer (b).

To further investigate the possible causes of this non linearity in the photon behavior, the late conversions up to the first sampling of the calorimeter were studied (see Appendix C).

9.2.3 Energy Leakage

The energy leakage out of the back of the calorimeter causes a degradation of the energy resolution as well as tails in the energy distributions. The calibration hits allowed us to recover the mean energy leakage for 60 GeV photons and electrons and 120 GeV electrons. The energy leakage is expressed as follows:

$$E_{Leakage} = E_{Beam} - (E_{TotalActive} + E_{TotalInactive} + E_{LostUpstream}) \tag{9.6}$$

Figures 9.4(a), 9.4(b) and 9.4(c) show the values for the three different samples.

The energy leakage is directly proportional to the energy of the particle, and the values used in this exercise are those of the most probable value (MPV) of the Landau fit.

9.2.4 Out-of-Cone Energy Correction Factor

The out-of-cone factor is dependent on the clusterization algorithm used. A '3×7' cluster will have a smaller out-of-cone factor than a '3×3' cluster. The factor is obtained by subtracting the energy deposited in a 3×3 cluster to the total energy deposited in the calorimeter (active and inactive) and later divided by the 3×3 energy. This factor, in terms of calibration hits, is given by:

$$E_{Total} - E_{3\times3} = f_{\text{Out Of cone}} \times E_{3\times3} \tag{9.7}$$

and the input value for the energy calculation is taken from the mean of the Gaussian fit of the distributions shown in Figures 9.5(a), 9.5(b) and 9.5(c).

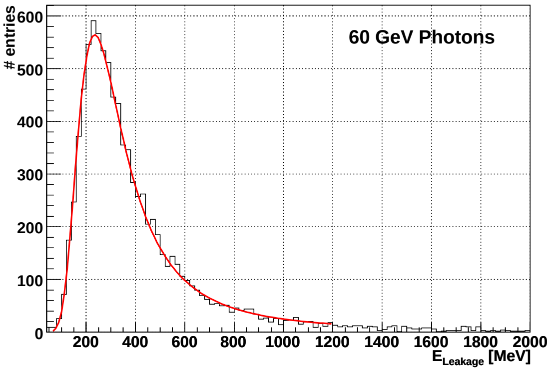

(a) Energy leakage for 60 GeV Photons

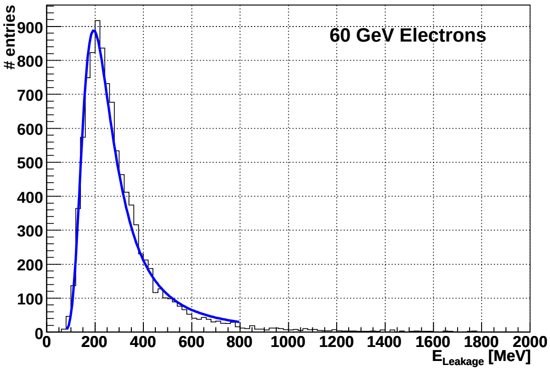

(b) Energy leakage for 60 GeV Electrons

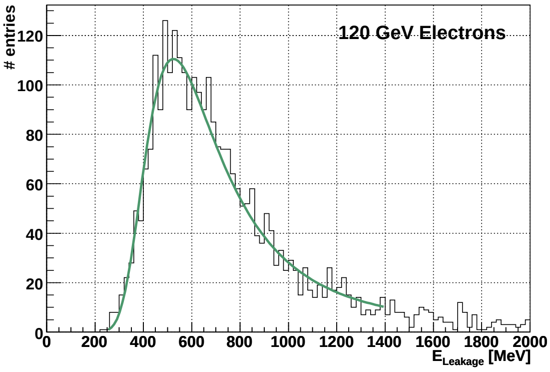

(c) Energy leakage for 120 GeV Photons

Figure 9.4 Energy leakage distribution (fitted) for 60 GeV photons and electrons and 120 GeV electrons.

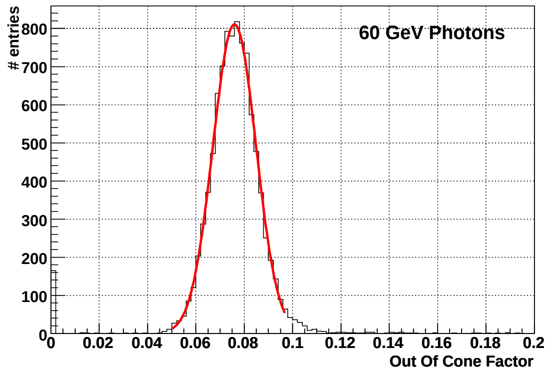

(a) Out-of-cone factor for 60 GeV Photons

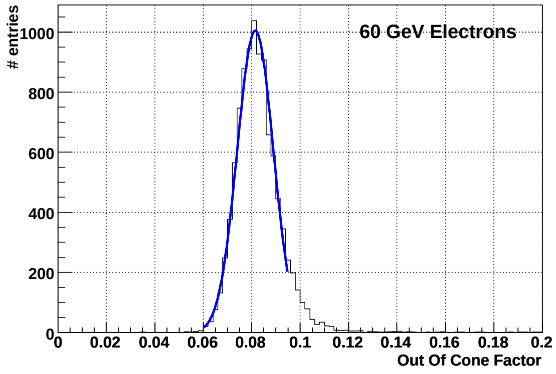

(b) Out-of-cone factor for 60 GeV Electrons

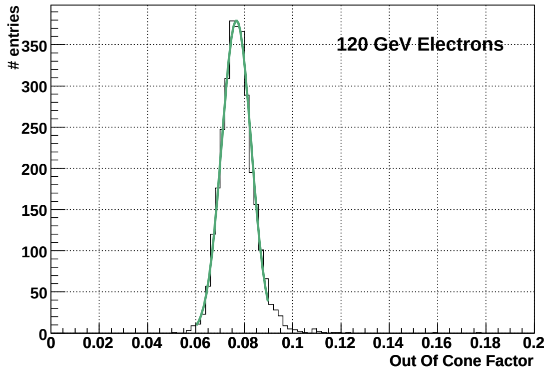

(c) Out-of-cone factor for 120 GeV Photons

Figure 9.5 Out-of-cone factors (fitted) for 60 GeV photons and electrons and 120 GeV electrons.

9.3 Summary of Calibration Hits Results

Table 9.2 displays the values obtained during the calibration hits studies for the electrons and photons.

Table 9.2 Summary Table

Parameters	Electron 120 GeV	Electron 60 GeV	Photon 60 GeV
Sampling Fraction	0.182	0.182	0.182
Offset (GeV)	0.358 ± 11.13	0.318 ± 5.8	0.115 ± 4.15
Presampler Weight (W_0)	17.83 ± 0.25	17.27 ± 0.4	19.68 ± 0.17
Energy Leakage (GeV)	0.546	0.202	0.249
Out of Cone Factor	0.077	0.081	0.076

Chapter 10

Determination of the Photon Global Energy Scale

This study assesses the response of the liquid argon calorimeter to photons. In order to do this, we take as a baseline the knowledge we have of electrons and their behavior. The idea is to correct the photon energy deposition in the calorimeter by using the correction constants derived for electrons with one change pertaining to the total energy scale and the other relating to the photons being converted or non-converted. This study considers all photons as *interacting* ones. The work presented here bases itself on MC calibration hits (Chapter 9) studies to derive the correction constants. The constants are later applied to the data to measure the photon energy scale. Results are compared to the value R derived in the previous chapter.

10.1 Corrected Reconstructed Cluster Energy

As seen in Chapter 5, a refined parametrization to calculate the energy per cell of a particle (electron) was obtained. Said parameterization took into consideration the calibration of sampling calorimeters as well as the various corrections for energy losses downstream and upstream of the LAr calorimeter as it related to electrons of different energies and pseudorapidities (η). Equation 10.1 expresses the partcle energy parameterization in terms of the visible energies and the constants obtained by means of the calibration hits (Chapter 9). It also involves the out-of-cone and leakage corrections (Chapter 9) as well as the charge collection effects (Chapter 4).

$$E_{RecCorr} = (\mathit{Offset}_{CH} + F_{ChC} \times W0_{CH} \times E0^{Vis} + f_{ChC} \times \frac{1}{f_{sampCH}}(E1 + E2 + E3)^{Vis} \\ + E_{OutOfCone_{CH}} + E_{Leakage_{CH}}) \tag{10.1}$$

where

- The subscript CH indicates a calibration hits derived quantity.
- F_{ChC} is the charge collection correction for the presampler.
- f_{ChC} is the charge collection correction for the accordion.
- The superscript Vis refers to visible energies.

Since we are trying to correct for the photon energy, assuming the electron energy is fully and correctly calibrated, we could express the total energy as:

$$E_{Tot} = E_{Electron/Positron} + \lambda \times E_{Photon} \tag{10.2}$$

Where λ should approach $\frac{1}{R}$. This λ is sensitive to the nature of the photons (see Chapter 9). We believe that this type of calibration scheme, where λ is derived by fitting the total energy resolution, could be applied to the problem at hand.

10.2 Data Calibration: Deriving the Photon Energy Scale

As previously stated, the goal was to calibrate the photons taking advantage of our knowledge of the electron behavior. Converted photons (outside the inner detector) will use the calibration constants derived for electrons, while non-interacting ones will require a different tuning (i.e. different offset and presampler weights). This means we must obtain a specific energy scale for non-converted photons from the data sample. In our case, we consider all photons as having interacted. In addition, all photons have already undergone two corrections during the reconstruction phase; they have been subject to the η and ϕ modulation corrections described in Chapter 4 .

The energy scale was obtained by fitting the total energy of positrons and photons through minimization of the function: $\Sigma\frac{(E_{Rec}-E_{True})^2}{\sigma^2_{EMB}}$, where E_{Rec} is the total reconstructed (measured) energy, E_{True} is the true beam energy and σ_{EMB} is a calorimeter resolution parametrization. The input variables to the fit were the offset, the presampler weight, the back leakage, the out-of-cone and charge collection factors. For the Minuit [34] fit [1] the positrons took as input the values obtained for 120 GeV electrons, while the photons accepted as input the values for 60 GeV electrons.

This parameterization technique has proven successful mostly for ATLAS electrons at various energies and η positions [25] and it has been used to some extent for ATLAS photons as well [4].

10.2.1 Effects of the Photon Scale and Corrections on the Total Energy Resolution

In principle the photon scale should linearize the response of the calorimeter to photons; however, the data analyzed do not allow for a linearity study given that during the combined test beam they were only taken at a particular energy and η region (η = 0.4). Since the longitudinal weights obtained using the calibration hits are there to correct for upstream energy losses of the calorimeter, we expect an improvement on the total energy resolution. The λ from fitting the total energy resolution using equations 10.2 and 10.1 is:

$$\lambda = 0.9895 \pm 0.0001 \tag{10.3}$$

This value satisfies the requirement imposed by the photon to electron energy ratio described in Chapter 9. Thus we have:

$$\begin{aligned} R &= \frac{1}{\lambda} \textit{ then} \\ R &= 1.0106 \pm 0.0001 \end{aligned} \tag{10.4}$$

To see the effect on the resolution pre and post energy scale fit and corrections the total energy distributions are shown in Figures 10.1(a) and 10.1(b).

---

[1] Minuit is conceived as a tool to find the minimum value of a multi-parameter function and analyze the shape of the function around the minimum. The principal application is foreseen for statistical analysis, working on chisquare or log-likelihood functions, to compute the best-fit parameter values and uncertainties, including correlations between the parameters. It is especially suited to handle difficult problems, including those which may require guidance in order to find the correct solution.

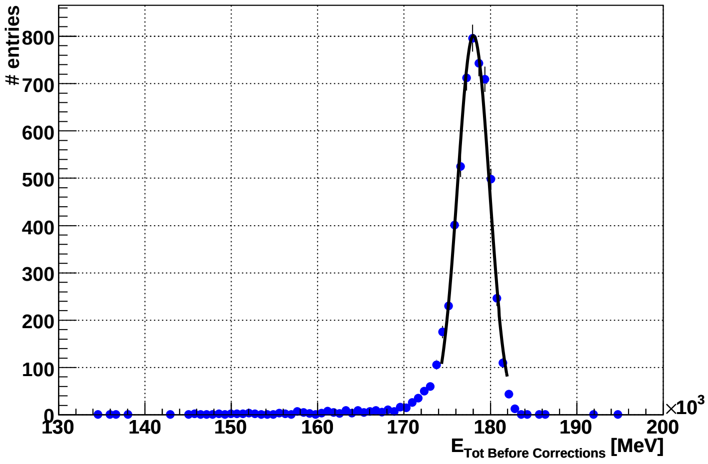

(a) Total Cluster Energy uncorrected

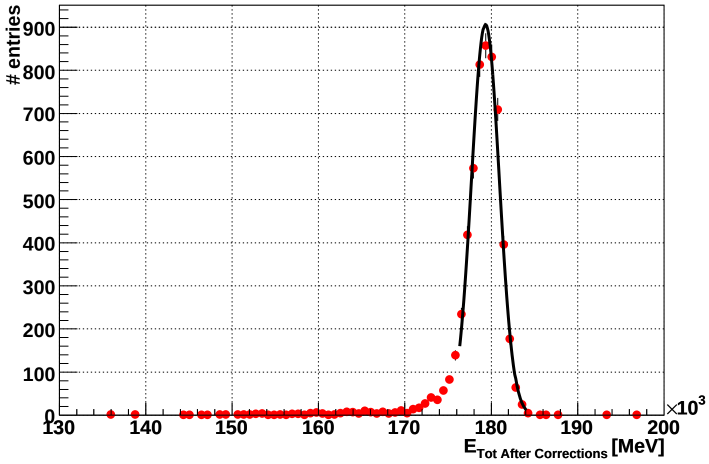

(b) Total Cluster Energy after application of energy scale and longitudinal weights.

Figure 10.1 Total cluster energy before and after all corrections.

While the mean of the distribution is $\sim$ 1 GeV apart between the corrected and uncorrected plots, there is a 15$\%$ improvement in their widths before and after corrections.

As far as the resolution is concerned, and taking into consideration the contributions from the noise and the constant term derived in Chapter 4, we have:

Before Corrections:

$$\frac{\sigma}{E} = \frac{0.224GeV}{178.0GeV} \oplus \frac{13.23\%}{\sqrt{178.0GeV}} \oplus 0.26\%$$

After Corrections:

$$\frac{\sigma}{E} = \frac{0.224GeV}{179.3GeV} \oplus \frac{11.34\%}{\sqrt{179.3GeV}} \oplus 0.26\%$$

10.3 Systematics

The sources of the systematic errors are legion. This section addresses the ones with larger impact on the measurement of the photon scale.

10.3.1 Systematics of the Photon Scale

Three systematic errors were included in this study:

1. Error of the measured beam energy;
2. Error due to the addition of extra material in front of the calorimeter;
3. Error due to the use of 60 GeV photon parameters.
4. Leakage from positron cluster into photon cluster.

Measured Beam Energy: Since the error on the measured beam energy is an important error in this calculation, it was obtained with independent electron beam data from period 5. This error was of the order of 0.3%.

$$\lambda = 0.9895 \pm 0.0001 \pm^{+0.003}_{-0.003}$$

Addition of Extra Material: The discrepancies seen when comparing the Monte Carlo simulations to the data, especially for the electron sample, suggests that the simulation is missing material that was measured in the test beam. Though the simulation with extra material was not available at the time of this thesis, the effect was simulated during the Minuit fit. The offset was increased by 10% and the presampler weight (W_0) by 1%. The new λ became:

$$\lambda = 0.9895 \pm 0.0001^{+0.003}_{-0.003} \pm 0.001$$

Use of Photon Parameters: When the parameters obtained for 60 GeV photons were used to determine the energy scale we incurred on the following systematic:

$$\lambda = 0.9895 \pm 0.0001^{+0.003}_{-0.003} \pm 0.001 \pm 0.003$$

Energy Leakage into Photon Cluster: When using the photon parameters a $\lambda = 0.9973 \pm 0.0001$ was obtained; however, a value of 1.0 was expected. This 0.27$\%$ difference hinted at the possibility of other effects being present. The energy leakage from the positron cluster into the photon cluster was analyzed and a 0.3-0.4$\%$ overestimation of the photon energy unveiled. Figures 10.2(a) through 10.2(d) show the leakages in the three different compartments of the calorimeter with the second sampling having the bulk of the contribution.

10.3.2 Systematics of the Total Energy Resolution

There is a small systematic from the difference between the arrival of the physics (particle) signal and the sampling of the signal maximum that needs to be found by the shape of the calibration pulse. If the maxima do not coincide within the 25 ns cycle of the master clock, the energy measurement is smeared. This small difference can be accounted by analyzing the total energy distribution as a function of the clock values. The effect is of the order of 300MeV. The addition of this systematic to our energy resolution yields;

$$\frac{\sigma}{E} = \frac{0.224GeV}{179.3GeV} \oplus \frac{11.10\%}{\sqrt{179.3GeV}} \oplus 0.26\% \oplus \frac{\sigma_{Clock}}{E}$$

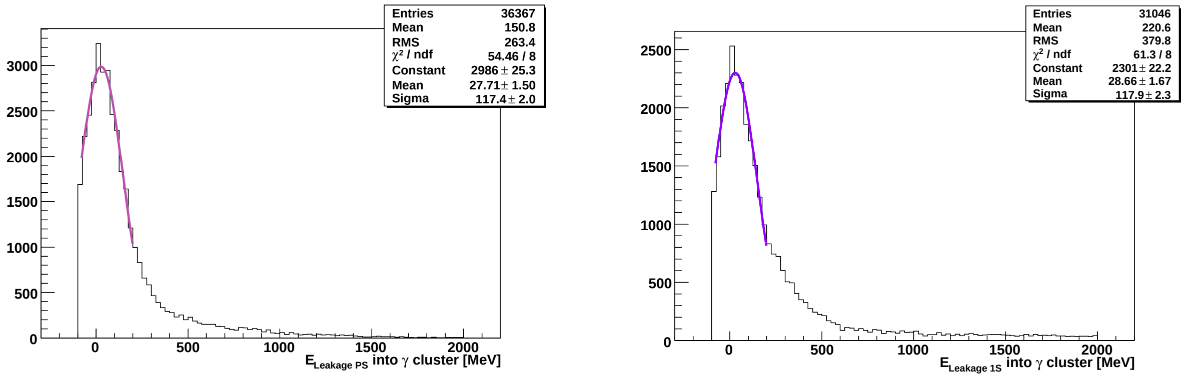

(a) Presampler

(b) First Sampling

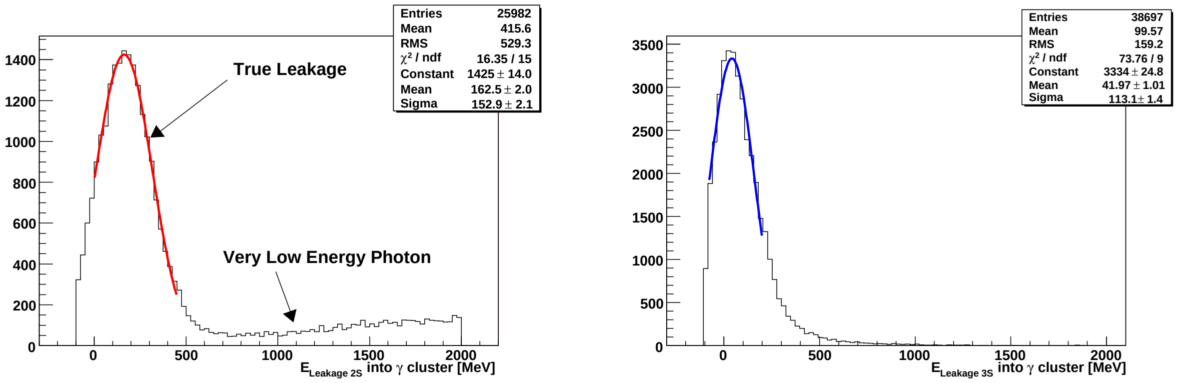

(c) Second Sampling

(d) Third Sampling

Figure 10.2 Energy leakage from the positron cluster into the photon cluster per sampling

Chapter 11

Results

This chapter presents a summary of the results and of their systematics where appropriate.

11.1 Calibration Hits

Calibration hits on 3×3 clusters were studied to assess the similarities between electrons and photons of the same energy (60GeV). The sampling fractions, longitudinal weights, energy leakage and out-of-cone corrections were derived for 60 GeV electrons and photons, as well as for 120 GeV electrons. They are summarized in Table 11.1 .

Table 11.1 Calibration Hits Results: Summary Table

Parameters	Electron 120 GeV	Electron 60 GeV	Photon 60 GeV
Sampling Fraction	0.182	0.182	0.182
Offset (GeV)	0.358 ± 11.13	0.318 ± 5.8	0.114 ± 4.15
Presampler Weight (W_0)	17.83 ± 0.25	17.27 ± 0.4	19.68 ± 0.17
Energy Leakage (GeV)	0.546	0.202	0.249
Out-of-Cone Factor	0.077	0.081	0.076

The percentage level difference (R) between electrons and photons of the same energy, making use of the electron corrections for both samples, was found to be:

$$\begin{aligned} R &= \frac{E_\gamma}{E_{e^-}} \\ R &= \frac{60.39 \pm 0.03 GeV}{59.78 \pm 0.01 GeV} \\ R &= 1.0102 \pm 0.0006 \end{aligned} \tag{11.1}$$

11.2 Photon Energy Scale

The parameters obtained with the calibration hits were applied to the total energy reconstruction using test beam data for photon run 2102966. The photon energy scale was calculated by performing a Minuit [34] fit on $E_{Beam} = E_{Electron/Positron} + \lambda \times E_{Photon}$ using the parameters obtained for 60 and 120 GeV electrons. The λ was found to be:

$$\lambda = 0.9895 \pm 0.0001$$

11.2.1 Systematics of the Photon Energy Scale

Three systematic errors were included in this study:

- Error on the measured beam energy;
- Error due to the addition of extra material in front of the calorimeter;
- Error due to the usage of 60 GeV photon parameters.

The three systematic checks are summarized below:

Measured Beam Energy:

$$\lambda = 0.9895 \pm 0.0001 \pm^{\mathbf{+0.003}}_{\mathbf{-0.003}}$$

Addition of Extra Material:

$$\lambda = 0.9895 \pm 0.0001^{+0.003}_{-0.003} \pm \mathbf{0.001}$$

Use of Photon Parameters:

$$\lambda = 0.9895 \pm 0.0001^{+0.003}_{-0.003} \pm 0.001 \pm \mathbf{0.003}$$

11.3 Total Energy Resolution

The parameters obtained with the calibration hits and the photon scale derived from the data fit were implemented in the calculation of the total energy resolution. Using equation 4.5 from Chapter 4 we have:

$$\frac{\sigma}{E} = \frac{0.224GeV}{179.3GeV} \oplus \frac{11.34\%}{\sqrt{179.3GeV}} \oplus 0.26\%$$

This yields an improvement of $\sim$ 16% in the stochastic term over the uncorrected value (13.23%). Since we are considering the electron and the photon to share the same stochastic term, electrons and photons will have the following resolution:

$$\frac{\sigma}{E_{Particle}} = \frac{0.224GeV}{E_{Particle}} \oplus \frac{11.34\%}{\sqrt{E_{Particle}}} \oplus 0.26\% \tag{11.2}$$

11.3.1 Systematic of the Total Energy Resolution

There is a small systematic induced by the difference between the arrival of the physics (particle) signal and the sampling of the signal maximum that is found by the shape of the calibration pulse. If the maxima do not coincide within the 25 ns cycle of the master clock, the energy measurement is smeared. The effect is of the order of 300MeV. The addition of this systematic to our energy resolution yields;

$$\frac{\sigma}{E} = \frac{0.224GeV}{179.3GeV} \oplus \frac{11.10\%}{\sqrt{179.3GeV}} \oplus 0.26\% \oplus \frac{\sigma_{Clock}}{E}$$

11.4 Monte Carlo Tuning

Agreement to within a few percent was seen when comparing the Monte Carlo production to the data sample. However, the origin of the discrepancies found on the energies of the first and second samplings for both photons and positrons remain unclear. Four feasible scenarios, outlined below, hypothesize on the causes of the shifts.

- There exists the possibility of extra material placed upstream of the calorimeter during data taking, but not present during the simulation.
- There could be extra material between the presampler and the strips.

- Extra losses in the middle compartment could be due to wider showers in real data.
- The strips may have more cross-talk than the estimated.

The possible causes of these fluctuations are currently under investigation.

Chapter 12

Conclusions and Outlook

The LHC physics program combined with the ATLAS physics goals will place stringent requirements on the performance of the electromagnetic calorimeter sub-system.

Accurate offline calibration will be paramount in the pursuit of an early Higgs discovery in the lepton and photon channels. In this thesis, the longitudinal weights, photon energy scale with a 0.3% error and other offline corrections are derived using a specialized Monte Carlo simulation (calibration hits) and are later applied to calibrate the 2004 photon test beam data. The improvements seen at the level of the energy resolution (data) after the calibration procedure allude to the possibility of a combined calibration strategy for electrons and photons.

Comparisons between data and Monte Carlo indicate that there are still issues to be resolved if our goal is an accurate Monte Carlo description of the data. The accuracy would be given by the data-Monte Carlo agreement for both photon and positron energies. Furthermore, in order to perform the right extrapolation to ATLAS, the test beam Monte Carlo wil have to use the same geometrical models as the ATLAS detector simulation. This feature will be included in future versions of the ATHENA framework.

The work presented in this thesis has been performed using the ATHENA Object Oriented framework, version 10.5.0, adapted to the test beam.

In the future, this exercise should be extended to encompass the different η regions and energies available to us in the test beam, and new constants should be derived for photons interacting in the inner detector region. The constants derived for interacting photons will allow us to test them in the $H \rightarrow \gamma\gamma$ channel. Further studies need to be performed to test the hypothesis that non-interacting photons can be distinguished by applying a cut on the presampler energy.

LIST OF REFERENCES

[1] https://uimon.cern.ch/twiki/bin/view/Atlas/CaloSimulation.

[2] L3 ALEPH, DELPHI, OPAL Collaborations, and the LEP working group for Higgs boson searches. Search for the Standard Model Higgs Boson at LEP. *ALEPH 2001-066 CONF 2001-046*, 2001.

[3] N. Besson and M. Boonekamp. Absolute lepton scale determinatino using z boson decays. application to the measurement of m_w. 2005.

[4] L. Carminati. *Calibration of the ATLAS electromagnetic calorimeter and its impact on the* $H \rightarrow \gamma\gamma$ *decay channel*. PhD thesis, Università Degli Studi di Milano, Facoltà di Scienze Matematiche, Fisiche e Naturali, 2003.

[5] W.E. Cleland and E.G. Stern. Signal processing considerations for liquid argon ionization calorimeters in a high rate environment. *Nuc. Inst. Meth. A*, A338:467–497, 1994.

[6] The ATLAS Collaboration. Liquid Argon Calorimeter Technical Design Report. Technical Report CERN/LHCC/96-41, CERN, 1996.

[7] The ATLAS Collaboration. Tile Calorimeter Technical Design Report. Technical Report CERN/LHCC/96-42, CERN, 1996.

[8] The ATLAS Collaboration. Inner Detector Technical Design Report. Technical Report CERN/LHCC/97-16, CERN, 1997.

[9] The ATLAS Collaboration. Inner Detector Technical Design Report. Technical Report CERN/LHCC/97-17, CERN, 1997.

[10] The ATLAS Collaboration. Magnet System Technical Design Report. Technical Report CERN/LHCC/97-18, CERN, 1997.

[11] The ATLAS Collaboration. Muon Spectrometer Technical Design Report. Technical Report CERN/LHCC/97-22, CERN, 1997.

[12] The ATLAS Collaboration. ATLAS DAQ, EF, LVL2 and DCS Technical Progress Report. Technical Report CERN/LHCC/98-16, CERN, 1998.

[13] The ATLAS Collaboration. Detector and Physics Performance Technical Design Report. Technical Report CERN/LHCC/99-14, CERN, 1999.

[14] The ATLAS Collaboration. Detector and Physics Performance Technical Design Report. Technical Report CERN/LHCC/99-15, CERN, 1999.

[15] The ATLAS Collaboration. Computing Technical Design Report. Technical Report CERN/LHCC/2005-022, CERN, 2005.

[16] F. Djama. Using $z^0 \rightarrow e^+e^-$ for Electromagnetic Calorimeter Calibration. *ATL-LARG-2004-008*, 2004.

[17] B. Aubert et al. Performance of the atlas electromagnetic calorimeter barrel module 0. *Nuc. Inst. Meth. A*, A500:202–231, 2003.

[18] B. Di Girolamo et al. ATLAS Barrel Combined Run in 2004 Test Beam Setup and its evolutions. *EDMS Note: ATC-TT-IN-0001*, 2005.

[19] B. Di Girolamo et al. Beam instrumentation in the 2004 combined ATLAS testbeam. *ATLAS Communication ATL-COM-TECH-2005-001*, 2005.

[20] F. Hubaut et al. Test beam Measurement of the Crosstalk in the EM Barrel Module 0. *ATL-LARG-2000-007*, 2000.

[21] L. Neukermans et al. Understanding the ATLAS electromagnetic barrel pulse shapes and the absolute electronic calibration. *ATLAS Internal Note LARG Internal Note*, 2001.

[22] M. Bettinelly et al. Analysis of the inclusive $h \rightarrow \gamma\gamma$ channel with dc1 samples. 2005.

[23] M.Escalier et al. Search for a Standard Model Higgs boson in the ATLAS experiment on the $h \rightarrow \gamma\gamma$ channel. 2005.

[24] R.M. Barnett et al. Review of particle properties. *Phys. Rev. D54 1*, 1996.

[25] S. Paganis et al. Combined Intercalibration and Longitudinal Weight Extraction for the ATLAS Liquid-Argon EM Calorimeter. *ATLAS Internal Note*, 2004.

[26] R. Sacco et al. for the ATLAS Liquid Argon Collaboration. Performance of the fine lateral segmentation of the first compartment of the ATLAS EM calorimeter. *ATLAS Note*, 2004.

[27] R. Sacco et al. for the ATLAS Liquid Argon Collaboration. Position resolution and particle identification with the ATLAS EM calorimeter. *ATLAS Note submitted to Elsevier Science*, 2005.

[28] T. Carli et al. for the ATLAS Liquid Argon Collaboration. Energy Linearity and Resolution of the ATLAS Electromagnetic Barrel Calorimeter and Electron Test-Beam. *Preprint submitted to Elsevier Science*, 2005.

[29] M. Gallas. Private communications.

[30] Michel Goossens, Frank Mittelbach, and Alexander Samarin. *The LaTeXCompanion*. Addison–Wesley Pub. Co., Reading, MA, 1994.

[31] Particle Data Group. Review of Particle Physics. *Physics Review D*, 2004.

[32] The ATLAS Electromagnetic Liquid Argon Calorimeter Group. Performance of the ATLAS electromagnetic calorimeter barrel module 0. *CERN-EP/2002-087*, 2002.

[33] The ATLAS Level-1 Trigger Group. Level-1 Technical Design Report. Technical Report ATLAS TDR-12, CERN, 1998.

[34] F. James. *MINUIT: Function Minimization and Error Analysis*. CERN Program Library Long Writeup D506, 1994.

[35] N. Kerschen. Private communication.

[36] W. Lampl. *Optimizing the energy measurement of the ATLAS electromagnetic calorimeter*. PhD thesis, Atominstitut der österreichschen Universitäten, 2005.

[37] L.D. Landau. *J.Exp.Phys.*, 8:201, (USSR) 8 1944.

[38] S. Paganis. Private communication.

[39] D. Prieur. *Etalonnage du calorimétre électromagnétique du détecteur ATLAS. Reconstruction des événements avec des photons non pointants dans le cadre d'un modéle supersymétrique GMSB.* PhD thesis, L'Université Claude Bernard - Lyon 1, 2005.

[40] A.C. Melissinos S. Behrens. *Univ. of Rochester Preprint*, 1981.

[41] W. Seligman. Particlegenerator:an athena monte-carlo event generator for simple particles, August 2005.

[42] The LHC study group. The Large Hadron Collider. Conceptual Design Report. Technical Report CERN/AC/95-05, CERN, 1995.

[43] S. Viret. Atlas electromagnetic barrel photon testbeam response compared to GEANT4 simulation. *ATLAS Internal Note*, 2004.

[44] R. Wigmans. *Calorimetry: Energy Measurements in Particle Physics*. Oxford University Press, Clarendon, 2000.

[45] D.H. Wilkinson. Ionization energy loss by charged particles part i.the landau distribution. *Nucl. Inst. Meth.*, A383:513, 1996.

[46] I. Wingerter-Seez. Study of energy reconstruction using optimal filtering with the LAr electromagnetic calorimeter. *ATLAS Internal Note LARG-NO-19*, 1995.

Appendix A: Extraction of Optimal Filtering Coefficients (OFCs)

The height of the pulse after shaping is proportional to the energy deposited by a passing charged particle in the liquid argon. By sampling the pulse at its peak, one can get a measurement of the energy. However, in doing this noise is introduced in the pulse, and the sample assumed to be taken at the peak of the pulse can be shifted due to jitter, etc.

These effects are partially compensated by sampling the pulse and applying the optimal filtering technique. Once the pulse shape and the noise autocorrelation matrix are known, linear coefficients can be optimized in order to maximize the signal to noise ratio.

With two sets of linear weights a_i and b_i the following linear combinations are formed:

$$\begin{aligned} A &= \sum_i a_i S_i \\ A\tau &= \sum_i b_i S_i \end{aligned} \tag{A.1}$$

where S_i are the signal samples. The computation of a_i and b_i is described in detail in [5], then the following conditions are imposed:

$$\begin{aligned} A &=< \sum_i a_i S_i > \\ A\tau &=< \sum_i b_i S_i > \end{aligned} \tag{A.2}$$

If the signal shape can be described with a function g, then the samples S_i can be expressed in the following way:

$$S_i = Ag(t-\tau) = Ag_i - A\tau g_i' n_i \tag{A.3}$$

Here n_i is the noise, while g_i and g_i' are respectively the value of the shaping function g and the value of its first derivative for the sample i.

When replacing S_i by its Taylor expansion in equation A.2, we get:

$$\begin{aligned} A &= \sum_i (Aa_i g_i - A\tau a_i g_i' + < n_i >) \\ A\tau &= \sum_i (Ab_i g_i - A\tau b_i g_i' + < n_i >) \end{aligned} \tag{A.4}$$

By requiring that the average of the noise remain equal to zero, the following constraints are obtained:

$$\begin{aligned} \sum_i a_i g_i = 1 \text{ and } \sum_i a_i g_i' = 0 \\ \sum_i b_i g_i = 0 \text{ and } \sum_i b_i g_i' = -1 \end{aligned} \tag{A.5}$$

With these conditions, the variances Var($\sum_i a_i S_i$) and Var($\sum_i b_i S_i$) are minimized using Lagrangean multipliers. This yields the following equations:

$$\begin{aligned} a_i &= \lambda V_{ij} g_j + \kappa V_{ij} g_j' \\ b_i &= \mu V_{ij} g_j + \rho V_{ij} g_j' \end{aligned} \tag{A.6}$$

Here, V_{ij} is the inverse of the autocorrelation matrix $R_{ij} =< n_i n_j >$, while λ, κ , μ and ρ are the Lagrangean multipliers, which are computed using the constraints given by the equations A.5.

In ATLAS, data will be taken synchronously with 5 samples at 25ns intervals. The third sample will be close to the peak, with a precision of 2ns. Optimal filtering will be applied to compute the pulse amplitude, to compensate for the jitter between the sampling clock and the pulse, and to reduce the noise.

Appendix B: Various Formulae

B.1 Bethe-Bloch Approximation

A particle passing through matter interacts with electrons and with nuclei. The particle, unless travelling at highly relativistic speeds, will lose energy by ionization. The mean energy loss (the stopping power) due to ionization is given by the Bethe-Bloch formula [24].

$$\begin{aligned} -\frac{dE}{dx} &= D\frac{Z}{A}\rho z^2\Phi(\beta)(1+\nu), \\ \text{with } \Phi(\beta) &= \frac{1}{\beta^2}(log(\frac{2m_ec^2\gamma^2\beta^2}{I(1+\gamma m_e/M)} - \beta^2 - \frac{\delta}{2} - \frac{Z}{C}) \end{aligned} \tag{B.1}$$

where

- E = particle energy
- M = particle mass
- β = particle velocity (in units of c)
- γ = 1/$\sqrt{(1-\beta^2)}$
- z = particle range (in units of elementary charge)
- x = path length
- D = 4 $\pi r_e^2 m_e c^2 N_A$ = 0.30707 MeV cm^2/mole
- r$_e$= 2.817 938 10^{23} cm = classical electron radius
- m$_e$ = 0.511 003 MeV/c^2 = electron rest mass
- N$_A$ = 6.022 10^{23}/mole = Avogadro’s number
- Z = atomic number of the medium
- A = atomic weight of the medium [g/mole]
- ρ = mass density of the medium [g/cm^3]
- I = average ionization potential
- δ = density correction
- C = shell correction
- ν = higher order correction.

B.2 Landau's Distribution

The Bethe-Bloch formula describes the average energy loss of charged particles. The fluctuation of the energy loss around the mean is described by an asymmetric distribution, the Landau distribution [45, 37]. The probability $\phi(\epsilon)d\epsilon$ that a singly charged particle losees energy between ϵ and $\epsilon + d\epsilon$ per unit length of an absorber is:

$$\phi(\epsilon) = \frac{2\pi Ne^4}{m_e v^2}\frac{Z}{A}\frac{1}{\epsilon^2} \tag{B.2}$$

If we define

$$\xi = \frac{2\pi Ne^4}{m_e v^2} ZAx\ , \tag{B.3}$$

where *x* is the area density of the absorber:

$$\phi(\epsilon) = \xi(x)\frac{1}{x\epsilon^2} \tag{B.4}$$

Numerically one can write

$$\xi = \frac{0.1536}{\beta^2}\frac{Z}{A}x\ \text{[keV]}\ , \tag{B.5}$$

where x is measured in mg/cm^2.

For an absorber of 1 cm Ar we have for $\beta = 1$, $\xi = 0.123keV$.

We define now

$$f(x, \Delta) = \frac{1}{\xi}\omega(\lambda) \tag{B.6}$$

as the probability that the particle loses an energy Δ on traversing an absorber of thickness *x*. λ is defined to be the normalized deviation from the most probable energy loss $\Delta^{m.p.}$.

$$\lambda = \frac{\Delta - \Delta^{m.p.}}{\xi} \tag{B.7}$$

The most probable energy loss is calculated to be [45, 40]

$$\Delta^{m.p.} = \xi \; ln \frac{2m_e c^2 \beta^2 \gamma^2 \xi}{I^2} - \beta^2 + 1 - \gamma E \,, \tag{B.8}$$

where $\gamma E = 0.577...$ is Euler's constant.

Landau's treatment of $f(x, \Delta)$ yields

$$\omega\lambda = \frac{1}{\pi} \int\limits_0^\infty e^{-u \ln u - \lambda u} \sin \pi u du \,, \tag{B.9}$$

which can be approximated by [40]

$$\Omega(\lambda) = \frac{1}{\sqrt{2\pi}} \exp - \frac{1}{2} \lambda + e^{-\lambda} \tag{B.10}$$

Appendix C: Treatment of Late Converting Photons

Given that the run under consideration did not include the inner detector, the number of conversions was reduced. However, late conversions became difficult to identify since there was no magnetic field to open up the $e^- e^+$ pairs. This situation will have an impact on ATLAS, for the inner detector will be able to trace conversions up to a radius $R < 80$ cm. Studies have shown [13] that approximately 30% of all converted photons (early conversions) happen within the ID cavity (up to 115cm along the radial direction). Figure C.1 shows that around 75% of these conversions occur in the volume (R $<$ 80 cm , $|z| <$ 280 cm), in which they can be easily identified. However, the late conversions will, at first glance, seem like non-interacting photons since the electron-positron pairs do not bend in the azimuthal direction.

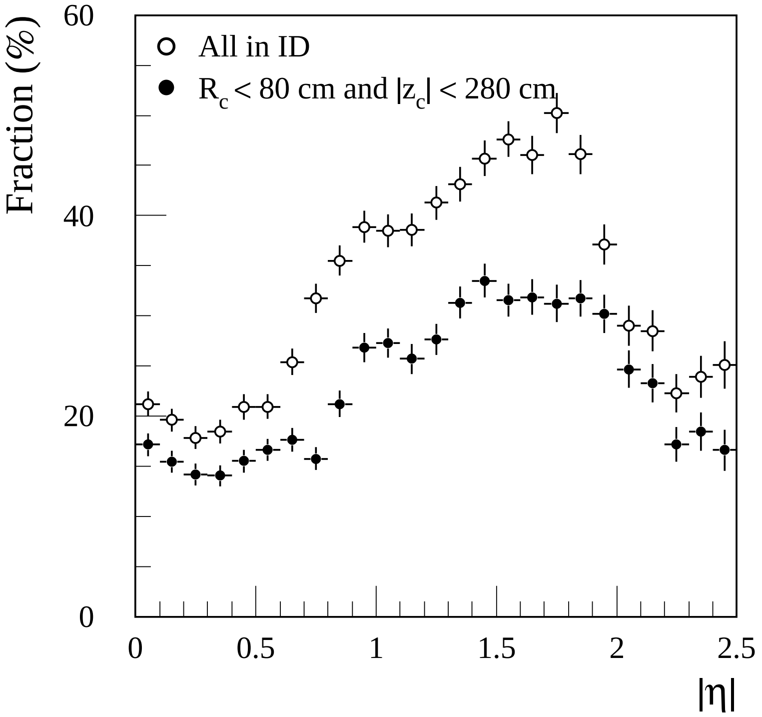

Figure C.1 Fraction of photons converted in the ID cavity (open symbols) and in the region in which conversions can be efficiently identified (closed symbols) as a function of pseudorapidity. Source [13].

After the ID, the cryostat has the largest amount of dead material for particles to traverse. In our particular test beam setup, photons had to travel $0.87X_0$ [1] of cryostat material until a hit was recorded on the presampler. The percentage of photons converting in the cryostat was 46.2$\%$, while the percentage of photons converted in the presampler was 7.7 $\%$. A depiction of the different conversion points along the beam line (from a beam photon) is given in Figure C.2.

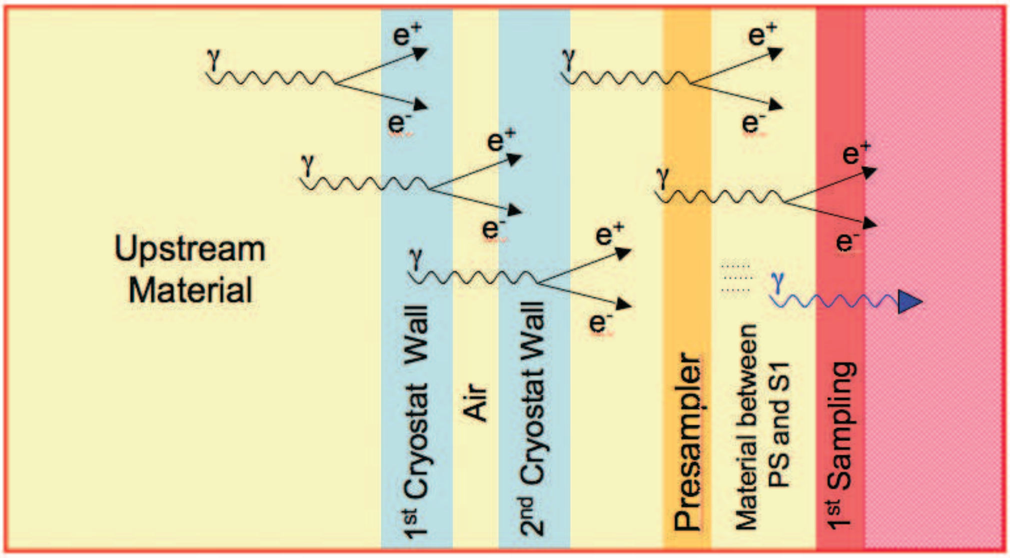

Figure C.2 Different conversion scenarios for late interacting photons (before cryostat and downstream). Drawing not to scale.

The study was performed using a Monte Carlo simulation, reflecting the conditions and setup of this particular run (see Chapter 8).

The idea behind the study of late conversions is to try to find a way to identify them, using the calorimeter as much as possible. We concentrated on the presampler and the first sampling layers. The earlier a photon converts, the sooner the shower develops, allowing for energy depositions on the presampler and the first sampling. Figure C.3 shows the visible energy depositions in the presampler for late conversions at different radii, corresponding to different regions upstream of the accordion. Observe that non-interacting photons leave maximum 5 MIPs in the presampler (the energy deposited by a MIP in the presampler is 2.52 MeV).

---

[1] The cryostat thickness is a function of the position in η. The value quoted here is for $\eta \sim 0.4$.

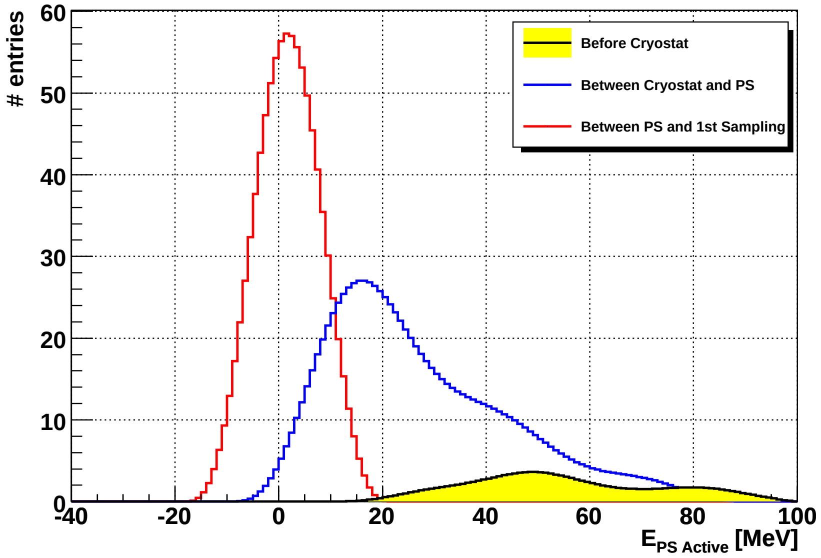

Figure C.3 Visible energy deposited by late-converting photons in the presampler, categorized by conversion radii.

From the preceding argument, we can conclude that a non-interacting photon will deposit almost no energy on the presampler and will have a higher deposition on the second sampling due to late showering. The difference, as seen in Figure C.5(a) , is subtle, nonetheless present. The distribution for 'All Photons' has a mean of 43.87 ± 1.3 GeV, while the distribution where a cut on the presampler was applied shifts its mean to 45.47 ± 2.3 GeV. The energy reading on the presampler for a non-converted photon should be compatible with the noise level on the presampler itself (see Chapter 7). The same behavior is observed in the data as well (Figure C.5(b)). The distribution in red has a mean of 43.85 ± 1.45. The distribution filled in light green has displaced its mean to 47.16 ± 1.82.

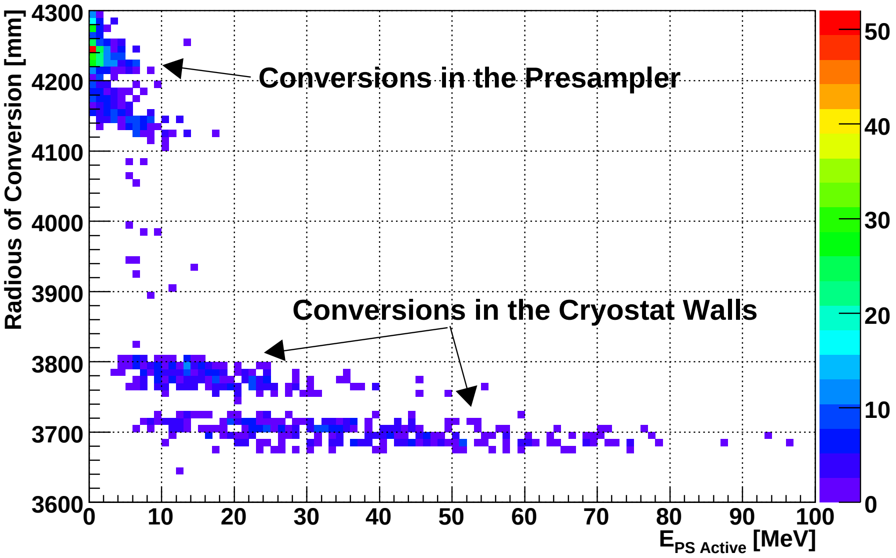

Figure C.4 Conversions radii in the cryostat and presampler as a function of the presampler visible energy

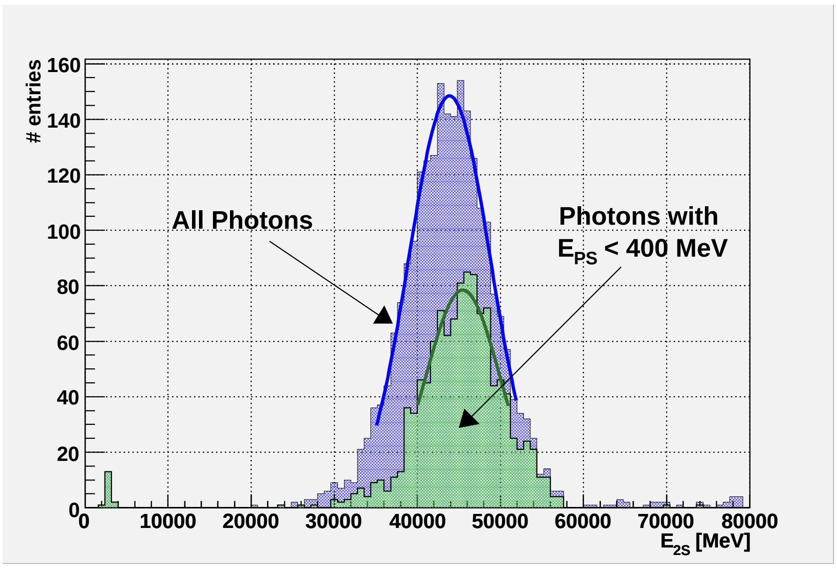

(a) Monte Carlo: Energy deposition in the second sampling for all photons and for photons where we require that E_{PS} be less than 400 MeV.

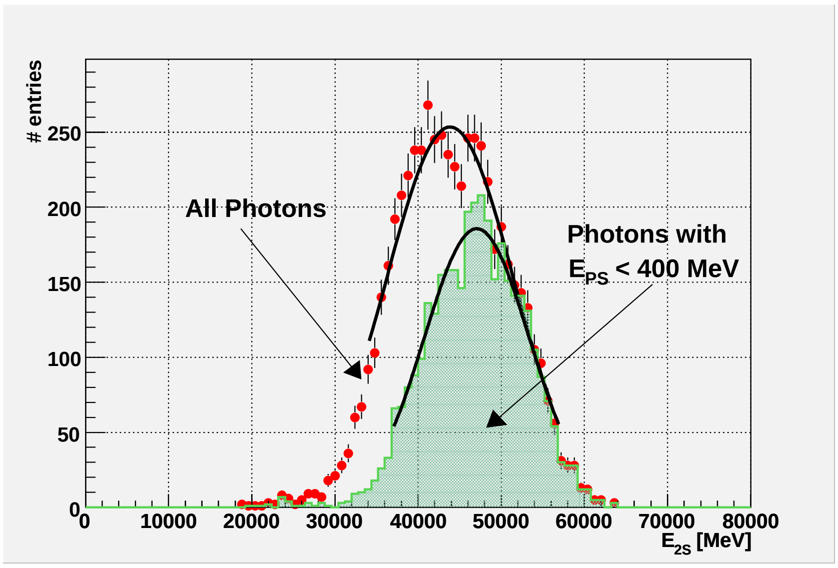

(b) Data: Energy deposition in the second sampling for all photons and for photons where we require that E_{PS} be less than 400 MeV.

Figure C.5 Differences between converted and non-converted photons as seen on the second sampling of the calorimeter.

Furthermore, the shower development also shows this trend. It can be seen by comparing the ratio of the first and second sampling energies as a function of the energy of the presampler. Figures C.6(a) and C.6(a) illustrate this point for Monte Carlo and data, respectively.

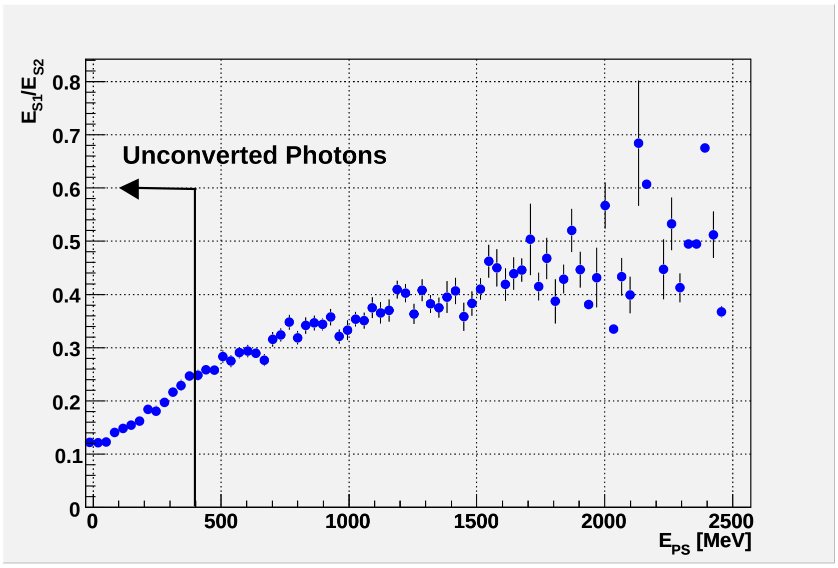

(a) Monte Carlo

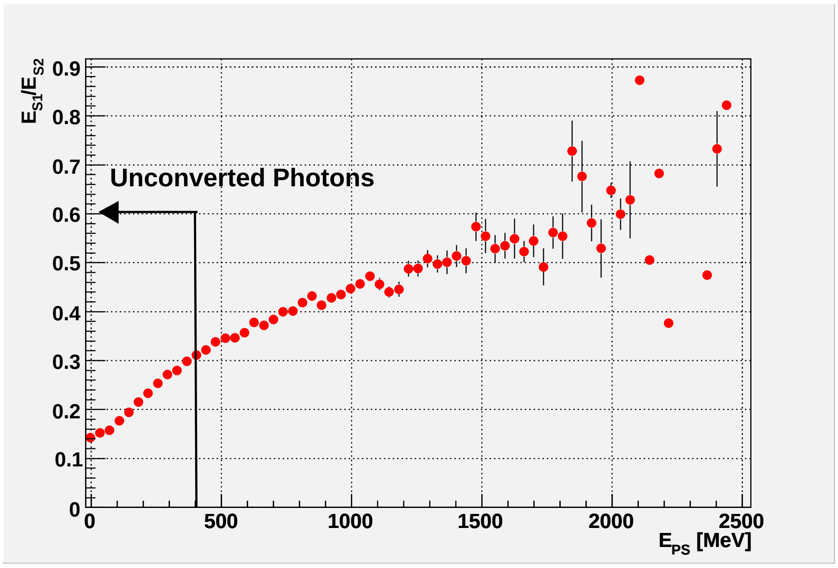

(b) Data

Figure C.6 Shower development as a function of the presampler energy.

Appendix D: Properties of the Relevant Materials

Table D.1 lists the properties of the relevant materials used in the construction of the electromagnetic calorimeter. The values have been obtained from [31]. The effective values for the accordion calorimeter include all materials used (Kapton, steel-coat, copper electrode and prepeg).

Table D.1 Material Properties

Material	Liquid Argon	Lead (Pb)	Aluminum (Al)	Accordion ($\eta < 0.8$) effective
Density [g/cm^3]	1.396	11.35	2.66	4.18
Radiation Length [cm]	14	0.56	8.9	2.02
dE/dx [MeV/cm] (MIP)	2.1	12.73	4.36	5.3
dE/dx [MeV/X$_0$] (MIP)	29.5	7.13	38.8	10.7
Critical Energy (e$^-$) [MeV]	38.13	7.79	42.55	-
Molière Radius [cm]	7.79	1.53	11.97	3.66